PHYSICAL REVIEW D **108,** 123518 (2023)

Featured in Physics

Hyper Suprime-Cam Year 3 results: Cosmology from cosmic shear two-point correlation functions

Xiangchong Li,[1,2,*] Tianqing Zhang,[1] Sunao Sugiyama,[2,3] Roohi Dalal,[4] Ryo Terasawa,[2,3] Markus M. Rau,[5,1]
Rachel Mandelbaum,[1] Masahiro Takada,[2] Surhud More,[6,2] Michael A. Strauss,[4] Hironao Miyatake,[7,8,2]
Masato Shirasaki,[9,10] Takashi Hamana,[9] Masamune Oguri,[11,12,3,2] Wentao Luo,[13,14] Atsushi J. Nishizawa,[15,7,8]
Ryuichi Takahashi,[16] Andrina Nicola,[17,4] Ken Osato,[11,18] Arun Kannawadi,[4] Tomomi Sunayama,[19,7]
Robert Armstrong,[20] James Bosch,[4] Yutaka Komiyama,[21] Robert H. Lupton,[4] Nate B. Lust,[4] Lauren A. MacArthur,[4]
Satoshi Miyazaki,[22] Hitoshi Murayama,[23,24,2] Takahiro Nishimichi,[25,2,26] Yuki Okura,[9] Paul A. Price,[4]
Philip J. Tait,[22] Masayuki Tanaka,[9] and Shiang-Yu Wang[27]

[1]*McWilliams Center for Cosmology, Department of Physics, Carnegie Mellon University,
5000 Forbes Avenue, Pittsburgh, Pennsylvania 15213, USA*
[2]*Kavli Institute for the Physics and Mathematics of the Universe (WPI), The University of Tokyo Institutes
for Advanced Study (UTIAS), The University of Tokyo, Chiba 277-8583, Japan*
[3]*Department of Physics, The University of Tokyo, Bunkyo, Tokyo 113-0031, Japan*
[4]*Department of Astrophysical Sciences, Princeton University, Princeton, New Jersey 08544, USA*
[5]*High Energy Physics Division, Argonne National Laboratory, Lemont, Illinois 60439, USA*
[6]*The Inter-University Centre for Astronomy and Astrophysics,
Post bag 4, Ganeshkhind, Pune 411007, India*
[7]*Kobayashi-Maskawa Institute for the Origin of Particles and the Universe (KMI), Nagoya University,
Nagoya, 464-8602, Japan*
[8]*Institute for Advanced Research, Nagoya University, Nagoya 464-8601, Japan*
[9]*National Astronomical Observatory of Japan, National Institutes of Natural Sciences,
Mitaka, Tokyo 181-8588, Japan*
[10]*The Institute of Statistical Mathematics, Tachikawa, Tokyo 190-8562, Japan*
[11]*Center for Frontier Science, Chiba University, 1-33 Yayoi-cho, Inage-ku, Chiba 263-8522, Japan*
[12]*Research Center for the Early Universe, The University of Tokyo, Bunkyo, Tokyo 113-0031, Japan*
[13]*School of Physical Sciences, University of Science and Technology of China, Hefei, Anhui 230026, China*
[14]*CAS Key Laboratory for Researches in Galaxies and Cosmology/Department of Astronomy,
School of Astronomy and Space Science, University of Science and Technology of China,
Hefei, Anhui 230026, China*
[15]*Gifu Shotoku Gakuen University, Gifu 501-6194, Japan*
[16]*Faculty of Science and Technology, Hirosaki University, 3 Bunkyo-cho, Hirosaki, Aomori 036-8561, Japan*
[17]*Argelander Institut für Astronomie, Universität Bonn, Auf dem Hügel 71, 53121 Bonn, Germany*
[18]*Department of Physics, Graduate School of Science, Chiba University,
1-33 Yayoi-cho, Inage-ku, Chiba 263-8522, Japan*
[19]*Department of Astronomy and Steward Observatory, University of Arizona,
933 North Cherry Avenue, Tucson, Arizona 85719, USA*
[20]*Lawrence Livermore National Laboratory, Livermore, California 94551, USA*
[21]*Department of Advanced Sciences, Faculty of Science and Engineering, Hosei University,
3-7-2 Kajino-cho, Koganei-shi, Tokyo 184-8584, Japan*
[22]*Subaru Telescope, National Astronomical Observatory of Japan,
650 North Aohoku Place Hilo, Hawaii 96720, USA*
[23]*Berkeley Center for Theoretical Physics, University of California, Berkeley, California 94720, USA*
[24]*Theory Group, Lawrence Berkeley National Laboratory, Berkeley, California 94720, USA*
[25]*Center for Gravitational Physics and Quantum Information, Yukawa Institute for Theoretical Physics,
Kyoto University, Kyoto 606-8502, Japan*
[26]*Department of Astrophysics and Atmospheric Sciences, Faculty of Science, Kyoto Sangyo University,
Motoyama, Kamigamo, Kita-ku, Kyoto 603-8555, Japan*
[27]*Institute of Astronomy and Astrophysics, Academia Sinica, Taipei 10617, Taiwan*

(Received 5 April 2023; accepted 22 September 2023; published 11 December 2023)

---

[*] xiangchl@andrew.cmu.edu

We perform a blinded cosmology analysis with cosmic shear two-point correlation functions measured from more than 25 million galaxies in the Hyper Suprime-Cam three-year shear catalog in four tomographic redshift bins ranging from 0.3 to 1.5. After conservative masking and galaxy selection, the survey covers 416 deg^2 of the northern sky with an effective galaxy number density of 15 arcmin^{-2} over the four redshift bins. The 2PCFs adopted for cosmology analysis are measured in the angular range; $7.1 < \theta/\mathrm{arcmin} < 56.6$ for ξ_+ and $31.2 < \theta/\mathrm{arcmin} < 248$ for ξ_-, with a total signal-to-noise ratio of 26.6. We apply a conservative, wide, flat prior on the photometric redshift errors on the last two tomographic bins, and the relative magnitudes of the cosmic shear amplitude across four redshift bins allow us to calibrate the photometric redshift errors. With this flat prior on redshift errors, we find $\Omega_\mathrm{m} = 0.256^{+0.056}_{-0.044}$ and $S_8 \equiv \sigma_8\sqrt{\Omega_\mathrm{m}/0.3} = 0.769^{+0.031}_{-0.034}$ (both 68% C.I.) for a flat Λ cold dark matter cosmology. We find, after unblinding, that our constraint on S_8 is consistent with the Fourier space cosmic shear and the 3×2 pt analyses on the same HSC dataset. We carefully study the potential systematics from astrophysical and systematic model uncertainties in our fiducial analysis using synthetic data, and report no biases (including projection bias in the posterior space) greater than 0.5σ in the estimation of S_8. Our analysis hints that the mean redshifts of the two highest tomographic bins are higher than initially estimated. In addition, a number of consistency tests are conducted to assess the robustness of our analysis. Comparing our result with *Planck*-2018 cosmic microwave background observations, we find a $\sim 2\sigma$ tension for the ΛCDM model.

DOI: 10.1103/PhysRevD.108.123518

I. INTRODUCTION

The flat Λ cold dark matter (ΛCDM) model, which is now considered as concordance cosmology model, explains a diverse set of observations with a nonzero cosmological constant Λ (which drives the accelerating expansion of the late-time Universe) and cold dark matter (which drives large-scale structure formation). The observations include the Hubble diagram of type Ia supernovae (e.g., [1]), big bang nucleosynthesis (e.g., [2]), fluctuations in the cosmic microwave background radiation (CMB; e.g., [3,4]), cosmic shear e.g., [5–7] and galaxy clustering e.g., [8–12]. As the precision of these observations has grown, we are now in the era of precision cosmology, focusing on possible small discrepancies between different observations when interpreted by the flat ΛCDM cosmology model. One such tension is the so-called σ_8 or S_8 tension, which refers to the fact that the ΛCDM models inferred from large-scale structure probes consistently exhibit a lower value of σ_8 or S_8 see [13] for a recent review, which characterizes the clustering amplitude in the present-day Universe, than do cosmological models inferred from the *Planck*-2018 CMB measurements [4]. A statistically significant discrepancy after marginalizing over the known systematic uncertainties could be an indication of physics beyond the flat ΛCDM cosmology. However, the discrepancy could also be a sign of unknown systematics in some of the observations or the analyses.

Weak gravitational lensing is one of the most important observations of large-scale structure at low redshifts. It refers to the small but coherent distortion of images of background galaxies due to the deflection of light when it travels through an inhomogeneous foreground matter density field [14]. Since weak lensing is caused by gravity, it is sensitive to the projected total matter (both dark matter and baryons) distribution along the line of sight [15]. Cosmic shear, namely the two-point statistics of lensing-shear distortion measured from background galaxy images, are related to the two-point statistics (i.e., the power spectrum) of the projected foreground matter density field. Cosmic shear measurements are particularly sensitive to the combination of cosmology parameters $S_8 \equiv \sigma_8\sqrt{\Omega_\mathrm{m}/0.3}$, where Ω_m is the total matter density parameter.

The ongoing Stage-III large-scale multiband photometric surveys which have weak lensing among their primary science targets include the Kilo-Degree Survey (KiDS) [16], the Dark Energy Survey (DES) [17], and the Hyper Suprime-Cam survey (HSC) [18] which is the subject of this paper. The HSC survey is an optical imaging survey covering about 1, 100 deg^2 using a 1.77 deg^2 field-of-view imager mounted on the 8.2-meter Subaru telescope [19–22]. The HSC survey is able to measure cosmic shear signals up to $z \sim 2$ from its i-band coadded images thanks to the combination of its depth (5σ point-source magnitude of $i \sim 26$) and good seeing (mean seeing size of $\sim$0.6 arcsec) for the HSC wide layer. In this paper, we focus on the Year 3 results of HSC (HSC-Y3), based on roughly 430 deg^2 of sky.

Li *et al.* [23] presented the HSC-Y3 shear catalog for weak-lensing science. We conducted a number of null tests on the shear catalog against many possible systematics such as modeling errors in the point-spread function (PSF) and shear estimation biases thus demonstrating that the HSC-Y3 shear catalog meets the requirements for weak-lensing science. Rau *et al.* [24] performed a joint redshift distribution inference on the sample, combining photometric redshift information with clustering redshifts from the CAMIRA luminous red galaxy sample

(CAMIRA-LRG; [25–27]). Zhang *et al.* [28] developed a technique to correct for systematic bias in cosmic shear analysis from fourth-order PSF modeling error and shape leakage to shear estimation.

In this paper, we present results from a tomographic cosmic shear analysis using the HSC-Y3 shear catalog. We measure the two-point correlation functions (2PCFs) from the HSC-Y3 shear catalog. Then we model the 2PCFs with twenty-three cosmological, astrophysical, and nuisance parameters. With a nested Bayesian sampling analysis, we constrain the cosmological parameters, especially focusing on S_8, in the context of the flat ΛCDM cosmology.

In our likelihood model, we carefully marginalize over various nuisance parameters quantifying systematic errors in the cosmic shear analysis [29]. The systematic errors we consider include systematic errors due to imperfect PSF modeling and PSF shape leakage [28], shear calibration uncertainties [23], and the photometric redshift (photo-z) uncertainties [24]. In addition to systematic errors, we study the modeling uncertainties in the matter power spectrum at small scales, e.g., the model uncertainties in the nonlinear power spectrum [30,31] and baryonic physics from star formation, supernovae, and AGN feedback [32–34]. Specifically, we use our fiducial pipeline to analyze various mock 2PCFs simulated using different nonlinear [31] and baryonic models to quantify the systematic uncertainties on the Ω_{m} and S_8 constraints. In addition, we adopt a conservative model to marginalize intrinsic shape correlations due to tidal alignment [35,36] and tidal torquing [37].

In order to obtain robust cosmological constraints, we perform a blinded analysis to avoid confirmation biases affecting our results. In particular, we conduct various blinded internal consistency tests by analyzing data in the context of the flat ΛCDM cosmology in different subfields, with different angular scale cuts, and removing each of the redshift bins to check the robustness of our results. Furthermore, we look for sensitivity of the central value and uncertainty in our S_8 constraint for analyses with flat priors on different cosmological parameters and prior ranges, analyses with different models for the linear and nonlinear matter power spectrum as well as different models for baryonic physics, analyses with different intrinsic alignment models, and analyses with different systematics models. After we confirm that there is no internal inconsistency in our cosmic shear 2PCFs analysis, we unblind our analysis and check the consistency of our constraints with the *Planck*-2018 CMB analysis [4] and other lensing surveys such as DES [7,38] and KiDS [6].

Our paper is organized as follows. In Sec. II we describe the basic characteristics of the HSC-Y3 dataset (including galaxy shear, photo-z, star shape and mock catalogs) that we use for the real space cosmic shear analysis. In Sec. III we measure the two-point correlation functions from the HSC shear catalog and the covariance from HSC mock catalogs. In Sec. IV we provide a brief overview of the theoretical model used in our likelihood. In Sec. V, we conduct internal consistency checks. In Sec. VI, we present our main results and compare them with constraints from external datasets. Throughout this paper, we report the mode of the 1D projected posterior distribution, along with 68% credible interval (CI) for parameter values and uncertainties. In addition, we also quote the maximum *a posteriori* (MAP) estimate from the Monte Carlo (MC) chain.

We note that this paper is one of a series of HSC-Y3 cosmological analysis papers, alongside:

(i) A cosmic shear analysis using pseudo-C_ℓ measurement [39].
(ii) A 3×2 pt analysis combining galaxy clustering, cosmic shear, and galaxy-galaxy lensing [40–42].

Those three cosmology analyses are conducted without any comparison between the cosmology constraints before unblinding. However, when performing model validation tests on synthetic data vectors, we make sure that the two cosmic shear analyses, from 2PCFs and pseudo-C_ℓ, are subject to the same criteria when making decisions on analysis choices.

II. HSC-Y3 DATA

In this section we briefly introduce the HSC-Y3 data for the cosmic shear analysis. The data is based on the S19A internal data release, which was released in September 2019 and was acquired between March 2014 and April 2019. First we introduce the galaxy shear catalog [23] that is used to measure the cosmic shear two-point correlation functions (2PCFs) is introduced in Sec. II A, the shear catalog blinding is discussed in Sec. II B, and the photometric redshift (photo-z) catalog [43] that is used to separate source galaxies into four tomographic bins and infer the galaxy redshift distribution is introduced in Sec. II C. The star catalog that is used to quantify PSF systematics is introduced in Sec. II D. Finally, we introduce the mock catalogs that are used to estimate the statistical uncertainties on our 2PCFs measurement in Sec. II E.

A. Weak-lensing shear catalog

1. Basic characterization

The original HSC-Y3 shape catalog [23] contains more than 35 million source galaxies covering 433 deg^2 of the northern sky. The galaxy sample is conservatively selected for the weak-lensing science with a magnitude cut on extinction-corrected `CModel` magnitude at $i < 24.5$, a `CModel` signal-to-noise ratio (SNR) cut at $\mathrm{SNR} > 10$ and a `reGauss` resolution cut at $R_2 > 0.3$ [23].

After the production of the shear catalog, a few additional cuts are applied to improve the data quality. In particular, we follow [44] to remove objects with extremely large i-band ellipticity which are potentially unresolved binary stars. To be more specific, we remove objects with large ellipticity, $|e| > 0.8$ and i-band determinant radius

$r_{\mathrm{det}} < 10^{-0.1r+1.8}$ arcsec (where r in the exponent is the r-band magnitude), amounting to 0.46% of the galaxy sample [23].

In addition, we remove a region in GAMA09H with 132.5 [deg] < ra < 140 [deg], 1.6 [deg] < dec < 5 [deg], containing an area of ∼20 deg^2. This region has very good seeing size ∼0.4 arcsec, but it has a smaller number of single-frame exposures contributing to the coadded images. In addition, we find significant PSF fourth-moment modeling errors in this region [28]. We find that including galaxy shapes in this region causes significant B-modes in 2PCFs at high redshifts and large scales.

Additionally, a number of galaxies are found to have secondary solutions at very high redshifts in their estimated photo-z posterior distributions, due to redshift template degeneracies. These secondary solutions are outside the redshift coverage of our CAMIRA-LRG sample [26] making it difficult to calibrate with the cross-correlation technique [24]. The details will be discussed in Sec. II C.

After these cuts, the final shear catalog contains 25 million galaxies covering 416 deg^2 of the northern sky. The catalog is split into six subfields: XMM, GAMA09H, WIDE12H, GAMA15H, VVDS and HECTOMAP. The area and effective galaxy number densities, n_{eff} (as defined in Ref. [45]), in different redshift bins of the subfields are summarized in Table I. The number density maps for six subfields are shown in Fig. 1. The effective standard deviation of the error on the per-component shear per galaxy is $\sigma_\gamma = 0.236$.

2. Galaxy shear

The HSC-Y3 shear catalog contains galaxy shapes, estimated with the re-Gaussianization (`reGauss`) PSF correction method [46] from the HSC i-band wide-field coadded images [47]. The `reGauss` estimator measures the two components of galaxy ellipticity,

$$(e_1, e_2) = \frac{1-(r_b/r_a)^2}{1+(r_b/r_a)^2}(\cos 2\phi, \sin 2\phi), \tag{1}$$

where r_b/r_a is the axis ratio, and ϕ is the position angle of the major axis with respect to the equatorial coordinate system. The lensing shear distortion, denoted as γ, coherently changes the galaxy ellipticities.

To control the shear estimation bias below 1% of the shear distortion, the galaxy shapes are calibrated with realistic image simulations downgrading galaxy images from Hubble Space Telescope [48] to the HSC observing conditions [49]. In the shear calibration, we modeled the biases, including multiplicative (m) and additive (c) biases from shear estimation, galaxy selection and galaxy detection as functions of galaxy properties (i.e., galaxy resolution, galaxy SNR, and galaxy redshift). For a galaxy sample distorted by a constant shear, the multiplicative bias and additive bias are given by

$$\hat{m} = \frac{\sum_i w_i m_i}{\sum_i w_i},$$
$$\hat{c}_\alpha = \frac{\sum_i w_i a_i e^{\mathrm{psf}}_{\alpha;i}}{\sum_i w_i}, \tag{2}$$

respectively. Here, i refers to the galaxy index, and w_i, m_i, a_i, e^{psf}_α are the galaxy shape weight, multiplicative bias, fractional additive bias, and PSF ellipticity for the galaxy with index i. $\alpha = 1, 2$ are the two components of spin-2 properties (e.g., ellipticity, shear, and additive bias). The galaxy shape weight for each galaxy is defined as

$$w_i = \frac{1}{\sigma^2_{e;i} + e^2_{\mathrm{rms};i}}, \tag{3}$$

where $e_{\mathrm{rms};i}$ is the root-mean-square (rms) of the intrinsic ellipticity per component for the ith galaxy. e_{rms} and σ_e are modeled and estimated for each galaxy using the image simulations. The estimated shear for the galaxy ensemble after calibration is

$$\check{\gamma}_\alpha = \frac{\sum_i w_i e_{\alpha;i}}{2\mathcal{R}(1+\hat{m})\sum_i w_i} - \frac{\hat{c}_\alpha}{1+\hat{m}}, \tag{4}$$

TABLE I. The area and effective number density $n^{(i)}_{\mathrm{eff}}$ ($i = 1, \ldots, 4$) [45] in each tomographic bin and in six different subfields (i.e., XMM, VVDS, GAMA09H, WIDE12H, GAMA15H, HECTOMAP); and those for the whole HSC-Y3 footprint across the four redshift bins.

Fields	Area (deg^2)	$n^{(1)}_{\mathrm{eff}}$(arcmin^{-2})	$n^{(2)}_{\mathrm{eff}}$(arcmin^{-2})	$n^{(3)}_{\mathrm{eff}}$(arcmin^{-2})	$n^{(4)}_{\mathrm{eff}}$(arcmin^{-2})	All (arcmin^{-2})
XMM	33.17	3.44	4.46	3.66	1.94	13.51
VVDS	96.18	3.82	5.13	4.21	2.13	15.30
G09H	82.36	3.99	4.74	3.81	2.11	14.65
W12H	121.32	3.61	5.20	3.96	2.06	14.82
G15H	40.87	3.92	5.38	4.27	2.24	15.81
HECT	43.06	3.74	5.34	4.05	2.32	15.44
All	416.97	3.77	5.07	4.00	2.12	14.96

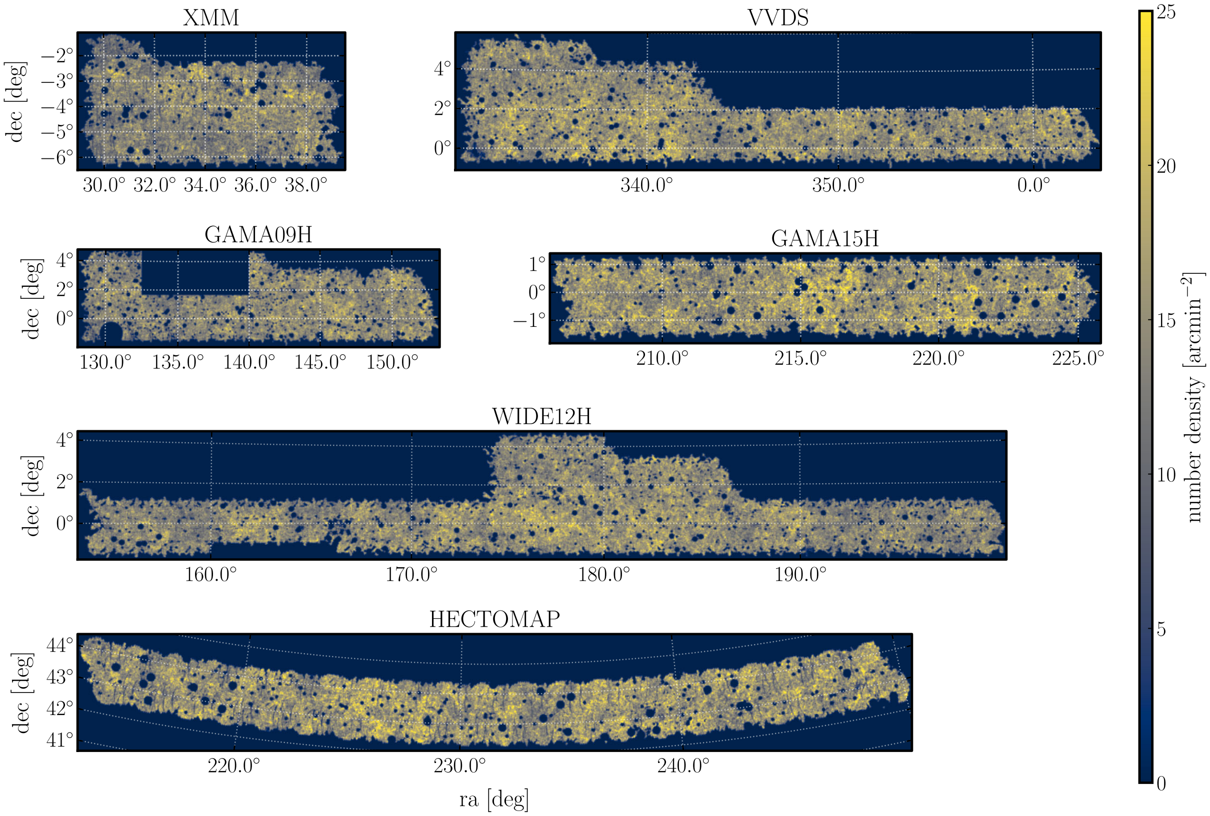

FIG. 1. The map of effective number density $n_{\rm eff}$ of galaxies across four redshift bins. A rectangular region in GAMA09H (132.5 [deg] < ra < 140 [deg], 1.6 [deg] < dec < 5 [deg] with very good seeing, a smaller number of input single exposures, and significant fourth-order PSF shape residual is removed from the original catalog.

where $\alpha = 1$, 2, and $\mathcal{R}$ is the shear responsivity for the galaxy population, defined as

$$\mathcal{R} = 1 - \frac{\sum_i w_i e^2_{\mathrm{rms};i}}{\sum_i w_i}. \tag{5}$$

3. Selection bias

Selection bias refers to a bias induced by selection cuts correlated with the true lensing shear and/or anisotropic systematics (e.g., PSF anisotropy). As a result, the selected galaxies that are sufficiently close to the edge of the cuts coherently align in a direction that correlates with the lensing shear and/or the systematics. The correlation with lensing shear leads to multiplicative shear estimation bias, whereas the correlation with anisotropic systematics leads to additive shear estimation bias.

We quantify selection bias in terms of multiplicative bias ($m^{\rm sel}$) and fractional additive bias ($a^{\rm sel}$) and estimate these biases from image simulations [23]. The estimated shear is corrected as

$$\hat{\gamma}_\alpha = \frac{\check{\gamma}_\alpha - \hat{c}^{\rm sel}_\alpha}{1 + m^{\rm sel}}, \tag{6}$$

where

$$\hat{c}^{\rm sel}_\alpha = \frac{a^{\rm sel} \sum_i w_i e^{\rm psf}_{\alpha;i}}{\sum_i w_i} \tag{7}$$

is the estimated additive selection bias [23].

Finally, the per-object shear ($\gamma_{\alpha;i}$) for a single galaxy is defined as

$$\gamma_{\alpha;i} = \frac{1}{1 + m^{\rm sel}} \left(\frac{e_{\alpha;i}/(2\mathcal{R}) - a_i e^{\rm psf}_{\alpha;i}}{1 + \hat{m}} - a^{\rm sel} e^{\rm psf}_{\alpha;i} \right). \tag{8}$$

The shear estimation from an galaxy ensemble defined in Eq. (6) is the weighted average of the per-galaxy shear.

In addition to the distortion of galaxy images from lensing shear, the lensing convergence, denoted as κ, isotropically distorts galaxy images and changes galaxy sizes and fluxes. Since the intrinsic galaxy sizes are unknown, we can only observe the reduced shear, denoted as $g_\alpha \equiv \gamma_\alpha/(1 - \kappa)$ from distorted galaxy images. In our work, we do not distinguish between the lensing shear and the reduced shear since it is a higher-order systematic bias, as shown in [50]. The bias caused by the reduced shear is less than $0.15\sigma_{\rm 2D}$, where $\sigma_{\rm 2D}$ is the 1σ contour in the 2D ($\Omega_{\rm m}$, S_8) plane for the DES fiducial cosmic shear analysis.

B. Shear-catalog blinding

In order to avoid confirmation bias in our cosmic shear analyses, we conduct our analysis with catalog-level blinding and analysis-level blinding. That is, our results are masked while conducting the analysis before unblinding.

For the catalog-level blinding, we measure 2PCFs and constrain cosmology using three blinded catalogs. Each catalog is blinded by adding a random additional multiplicative bias with a two-level catalog blinding scheme [23]. The first is a user-level blinding to prevent an accidental comparison of blinded catalogs between different cosmological analyses (i.e., the cosmic shear 2PCFs analysis in this paper, the cosmic shear Fourier space analysis [39] and the 3×2 pt analysis [41,42]), whereas the second is a collaboration-level blinding to prevent analysers knowing which catalog of the three is the true catalog.

For the user-level blinding, a random additional multiplicative bias $\mathrm{d}m_1$ is generated for each catalog. The values of $\mathrm{d}m_1$ are different for each analysis team, and they are encrypted with the public keys from the principal investigators of the corresponding analysis teams. This single value of $\mathrm{d}m_1$ is decrypted and subtracted from the multiplicative bias values for each catalog entry to remove the user-level blinding before the cosmic shear analysis.

For the collaboration-level blinding, three blinded catalogs are generated with indexes $j = 0, 1, 2$. The additional multiplicative biases $\mathrm{d}m_2^j$ for these three blinded catalogs are randomly selected from the following three different choices of $(\mathrm{d}m_2^1, \mathrm{d}m_2^2, \mathrm{d}m_2^3)$: $(-0.1, -0.05, 0)$, $(-0.05, 0, 0.05)$, $(0, 0.05, 0.1)$. Note, we set the difference in multiplicative bias between three catalogs to be 0.05, corresponding to a shift in S_8 by ~ 0.05, in order to cover the S_8 tension between weak-lensing and CMB observations. The additional multiplicative biases are listed in an ascending order, in each case, while the true catalog (with $\mathrm{d}m_2 = 0$) has a different index for the three options. The values of $\mathrm{d}m_2^{1,2,3}$ are encrypted by a public key from one designated person who is not involved in any cosmology analysis.

The final blinded multiplicative bias values for the galaxies in each of these three catalogs are

$$m^j_{\mathrm{blind;i}} = m_{\mathrm{true;i}} + \mathrm{d}m_1^j + \mathrm{d}m_2^j, \tag{9}$$

where i is the galaxy index in each blinded catalog indexed by j. We carry out the same analysis for all three catalogs for internal consistency checks (see Sec. V) after decrypting and subtracting the $\mathrm{d}m_1$ from the multiplicative bias for each catalog.

We adopt an analysis-level blinding for the internal consistency tests in Sec. V. Specifically, we shift the posteriors along each cosmological parameter, e.g., S_8 and Ω_m, by the corresponding projected mode estimate from the fiducial chain. As a result, we only show the difference between the internal tests and the fiducial chain. In addition, we do not compare the measured 2PCFs with predictions of any known cosmology. Moreover, the analysis team did not compare the posterior of cosmology parameters with any external results (e.g., *Planck* CMB, DES and KiDS's constraints) before unblinding.

The analysis team agreed that, once the results were unblinded, they would be published regardless of the outcome. In addition, the analysis method could not be changed or modified after unblinding.

C. Photometric redshift catalog

In the following, we briefly summarize the three methods for photometric redshift (photo-z) estimation at the individual galaxy level. We refer the readers to Nishizawa *et al.* [43] for more details.

`dNNz` is a photo-z conditional density estimation algorithm based on a neural network. Its architecture consists of multi-layer perceptrons with five hidden layers. The code uses `CModel` fluxes, convolved fluxes, PSF fluxes, galaxy sizes and galaxy shapes for the training. The photo-z conditional density is constructed with 100 nodes in the output layer, and each node represents a redshift histogram bin spanning from $z = 0$ to redshift $z = 7$ ([51]).

The direct empirical photometric redshift code (`DEmPz`) is an empirical algorithm for photo-z conditional density estimation [52]. It uses quadratic polynomial interpolation of 40 nearest neighboring galaxies in a training set, with a distance estimated in a 10 dimensional feature space (5 magnitudes, 4 colors, and 1 size information). `DEmPz` estimates the error for the constructed photo-z conditional densities with resampling procedures.

`mizuki` [53] is a photo-z algorithm adopting a spectral energy distribution (SED) fitting technique. The method uses an SED template set constructed with Bruzual-Charlot models [54], a stellar population synthesis code using an initial mass function following Chabrier [55], emission-line modeling assuming solar metallicity [56], and a dust attenuation model from Calzetti *et al.* [57]. It applies a set of redshift-dependent Bayesian priors on the photo-z estimation, and, to improve the accuracy, the photo-z posteriors of galaxies are calibrated with the specXphot dataset [58].

We divide the galaxies in the shear catalog introduced in Sec. II A into four tomographic redshift bins by selecting galaxies using the best estimate, minimizing the estimation risk (see Nishizawa *et al.* [43] for more details), of the `dNNz` photo-z algorithm within four redshift intervals—(0.3, 0.6], (0.6, 0.9], (0.9, 1.2] and (1.2, 1.5]. We find $\sim 31\%$ and $\sim 8\%$ galaxies in the first and second redshift bins, respectively, have double peaks in the `mizuki` and `dNNz` photo-z probability density function (PDF), and the secondary peak corresponds to a significant fraction of outliers at $z \gtrsim 3.0$. We remove these galaxies from our sample for 2PCFs measurement since the secondary peaks are outside the redshift coverage of the CAMIRA-LRGs [24]

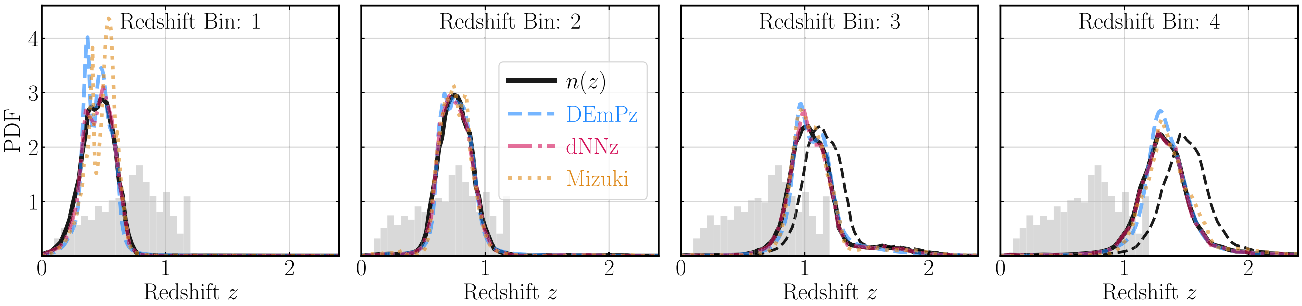

FIG. 2. The comparison between $n(z)$ distributions (solid line) estimated by the joint calibration with CAMIRA-LRG sample [24] and those estimated by stacking the `DEmPz` (dashed lines), `dNNz` (dot-dashed lines) and `mizuki` (dotted lines) photo-z posteriors from individual galaxies. The shaded grey histogram is the number density as a function of redshift of CAMIRA-LRGs used to calibrate the $n(z)$ distributions of the solid lines. The median redshifts for the four redshift bins (solid black lines) are 0.44, 0.75, 1.03 and 1.31, and the median redshift for the overall sample is 0.80. The dashed black lines in the last two redshift bins are the $n(z)$ distributions after after the self-calibration in parameter inference (see text for details).

(see Sec. IV C) that is used to calibrate the galaxy redshift distribution, and therefore can potentially produce large systematic uncertainties.

To be more specific, galaxies with secondary peaks are identified with the following selection criteria based on the distance between the 0.025 and 0.975 quantiles of the `mizuki` and `dNNz` photo-z PDF estimates

$$\left(z^{\mathrm{mizuki}}_{0.975;i} - z^{\mathrm{mizuki}}_{0.025;i}\right) < 2.7 \quad \text{and} \quad \left(z^{\mathrm{dnnz}}_{0.975;i} - z^{\mathrm{dnnz}}_{0.025;i}\right) < 2.7, \tag{10}$$

where $z^{\mathrm{mizuki\,(dnnz)}}_{0.975;i}$ and $z^{\mathrm{mizuki\,(dnnz)}}_{0.025;i}$ denote the 97.5 and 2.5 percentiles for galaxy i derived with the `mizuki` (`dNNz`) photo-z PDF estimates, respectively. We do not find a significant number of double solutions for `DEmPz`, thus we do not include it in the criteria above. In Fig. 2, we show the stacked photo-z posteriors from individual galaxies in each redshift bin for these three photo-z estimators, after rejecting galaxies with double solutions. The $n(z)$ obtained by combining multiple photo-z's and calibrated with CAMIRA LRGs [24] is used for our fiducial analysis. The calibrated $n(z)$ is shown in Fig. 2.

D. Star catalog

The HSC-Y3 star catalog used to quantify the PSF systematics in the estimation of the 2PCFs is selected from the star samples described in Sec. V.1 of Li *et al.* [23], which covers the same footprint as the galaxy shear catalog described in Sec. II A. We briefly summarize the star sample we used in this paper, and refer the readers to [23] for more details.

The PSF models in the HSC-Y3 coadded images are constructed by stacking the PSF models estimated in each CCD exposure contributing to the coadded pixels, and the PSF models in a CCD exposure are constructed by interpolating star images on the same CCD. The selection of stars used for PSF modeling is based on the k-means clustering of high-SNR (i.e., SNR > 50) objects in size, typically resulting in ~80 star candidates per CCD chip (an area of ~60 arcmin^2; see Bosch *et al.* [47] for more details). In the single exposure CCD processing, ~20% of the stars in a given single exposure are randomly selected and reserved for cross-validation, and are not used for PSF modeling. Since the star sample used in PSF modeling is derived on individual exposures, different exposures will not necessarily select the same set of reserved stars. At the coadded image level, stars that were used by $\geq 20\%$ of the input exposures are labelled as having been used in the modeling, namely "`i_calib_psf_used` == True."

The star sample that is used to quantify PSF systematics on 2PCFs is selected by "`i_extendedness_value` == 0," a cut indicating whether an object is an extended galaxy or a pointlike star. After that, we apply an i-band magnitude cut at 22.5 to select a star sample with high SNR. Li *et al.* [23] further divide this magnitude limited star sample into two subsamples; those flagged by "`i_calib_psf_used` == True" are PSF stars and the others are defined as non-PSF stars.

In this paper, we use the PSF star sample to estimate the additive bias on 2PCFs from PSF systematics, since as shown in Zhang *et al.* [28], the additive bias on 2PCFs estimated from PSF stars is consistent with that estimated with non-PSF stars. In addition, the estimation of the PSF systematic error from PSF stars has higher SNR since there are more stars in the PSF star sample. We give the details of how we use PSF stars to estimate the additive PSF systematic error and marginalize over it in our cosmological analysis in Sec. IV E.

E. Mock catalogs

In this subsection, we introduce the HSC-Y3 galaxy mock shear catalogs, which are used to accurately quantify the uncertainties of our measured 2PCFs (both galaxy-galaxy and galaxy-star shape correlations) due to cosmic variance, galaxy shape noise, measurement errors due to photon noise, and photometric redshift uncertainties. The mock catalogs are generated following Shirasaki *et al.* [59] with updates to incorporate the survey footprint, galaxy shape noise, shape measurement error, and photometric redshift error of the HSC-Y3 shear catalog.

The mock shear catalog uses simulations of the full-sky shear map at 38 redshifts generated by the ray-tracing simulation [60] with $108 N$-body simulations of the WMAP9 cosmology ($H_0 = 70$ km/s/Mpc, $\Omega_\mathrm{m} = 0.279$, $\Omega_\mathrm{b} = 0.046$, $\sigma_8 = 0.82$) [3]. The ray-tracing simulation calculates the light-ray deflection on the celestial sphere using the projected matter density field at the spherical shells [61,62]. Each shell has a radial "thickness" of 150 h^{-1} Mpc. The angular resolution of the shear map is 0.43 arcmin.

In order to increase the number of realizations of the mock catalogs, we extract 13 separate regions with the same HSC three-year survey geometry from each full-sky shear map, obtaining $108 \times 13 = 1404$ mock catalogs in total. These 1404 lensing-shear maps at 38 redshift planes are combined with the observed angular positions, photo-z s, and shapes of real galaxies [23] to generate mock shear catalogs. To be more specific, source galaxies are populated on the lensing-shear maps using the original angular positions and the `dNNz` "best-fit" redshift estimates of the galaxies in the HSC shear catalog. Each galaxy is assigned a source redshift estimate in the mock following the `dNNz` photo-z posterior distribution. The shape noise on each galaxy is generated with a random rotation of the galaxy's intrinsic shape following the intrinsic shape dispersion estimated in the HSC shear catalog, and the measurement error is generated as a zero-mean Gaussian random number with the standard deviation measured in the HSC shear catalog. We distort each galaxy's intrinsic shape with the shear value on the shear map and add measurement error to the distorted shape to generate the final galaxy shape see Sec. IV.2 in Ref. [59].

We note that our simulations use source galaxy positions from the real HSC data but unlike the real Universe, the positions are not correlated with the density field in the simulations. The correlation between the source galaxy clustering and the shear signal [63] are neglected in the mock.

III. TWO-POINT STATISTICS

The 2PCFs of galaxy shear [14], denoted as $\xi_\pm(\theta)$, are two-point statistics that are widely used to constrain cosmological parameters. In Sec. III A, we measure the 2PCFs from the galaxy shear catalog introduced in Sec. II A; in Sec. III B, we derive the covariance matrix of the 2PCFs using mock shear catalogs introduced in Sec. II E; in Sec. III C, we measure the B-modes on 2PCFs to test the systematics in our measurement.

A. Two-point correlation functions

The 2PCFs can be measured from the shear catalog using the per-object shear defined in Eq. (8),

$$\hat{\xi}_\pm(\theta) = \frac{\sum_{i,j} w(\boldsymbol{r}_i)\gamma_+(\boldsymbol{r}_i) w(\boldsymbol{r}_j)\gamma_+(\boldsymbol{r}_j)}{\sum_{i,j} w(\boldsymbol{r}_i) w(\boldsymbol{r}_j)} \pm \frac{\sum_{i,j} w(\boldsymbol{r}_i)\gamma_\times(\boldsymbol{r}_i) w(\boldsymbol{r}_j)\gamma_\times(\boldsymbol{r}_j)}{\sum_{i,j} w(\boldsymbol{r}_i) w(\boldsymbol{r}_j)}, \tag{11}$$

where the summation is over every galaxy pair (i, j) with angular separation θ. For each galaxy pair, we decompose the per-object shear estimates $\gamma_\alpha(\boldsymbol{r}_i)$ into tangential components, $\gamma_+(\boldsymbol{r}_i)$, and cross components, $\gamma_\times(\boldsymbol{r}_i)$, with respect to the direction connecting the two galaxies in a pair.

We use the public software TreeCorr[1] to measure both the auto and cross-correlations from the four tomographic redshift bins in equal log-intervals of $\Delta \log(\theta) = 0.29$ in the range $7.1 < \theta/\mathrm{arcmin} < 56.6$ for ξ_+, and $31.2 < \theta/\mathrm{arcmin} < 248$ for ξ_-. The small-scale cut is determined by the requirement to control the modeling error on the matter power spectrum at small scales due to baryonic physics (Sec. IV A); and the large-scale cut is determined by the B-mode systematics (Sec. III C). For different redshift bins, we use consistent scale cuts in θ for each of the measured auto and cross-correlations ξ_+ and ξ_-. It is worth mentioning that the DES cosmic shear analysis [7,64] adopts a redshift-dependent scale cut. Given that we have not observed compelling evidence suggesting a specific scale at any particular redshift introduces significant bias, we choose to fix the scale cut across different bins, which simplifies our decision-making process regarding scale cuts. Figure 3 shows the 2PCFs (i.e., $\hat{\xi}_+^{ij}$ and $\hat{\xi}_-^{ij}$) measured from the galaxy shear catalog in four tomographic bins. The i and j specify the galaxy samples in two tomographic bins (note, in the case of $i = j$, the same tomographic bin) from which the correlation function is calculated. The unshaded region denotes the scales used for our fiducial analysis. We have 7 angular bins for both ξ_+ and ξ_-. In total, we have $(7 + 7) \times 10 = 140$ data points for the 10 auto and cross-redshift bins, and the SNR of the 2PCFs is 26.6 including the Hartlap correction when estimating the inverse of the covariance matrix [65].

We note that although we focus on 2PCFs in this paper, several alternative cosmic shear two-point statistics have been used in the literature. These two-point statistics include the angular power spectrum in Fourier space e.g., [66–68] and the complete orthogonal sets of E/B-integrals e.g., [69,70]. In particular, Dalal *et al.* [39] carry out analysis in parallel to this paper using the angular power spectrum in Fourier space with the same catalog.

---

[1] https://github.com/rmjarvis/TreeCorr.

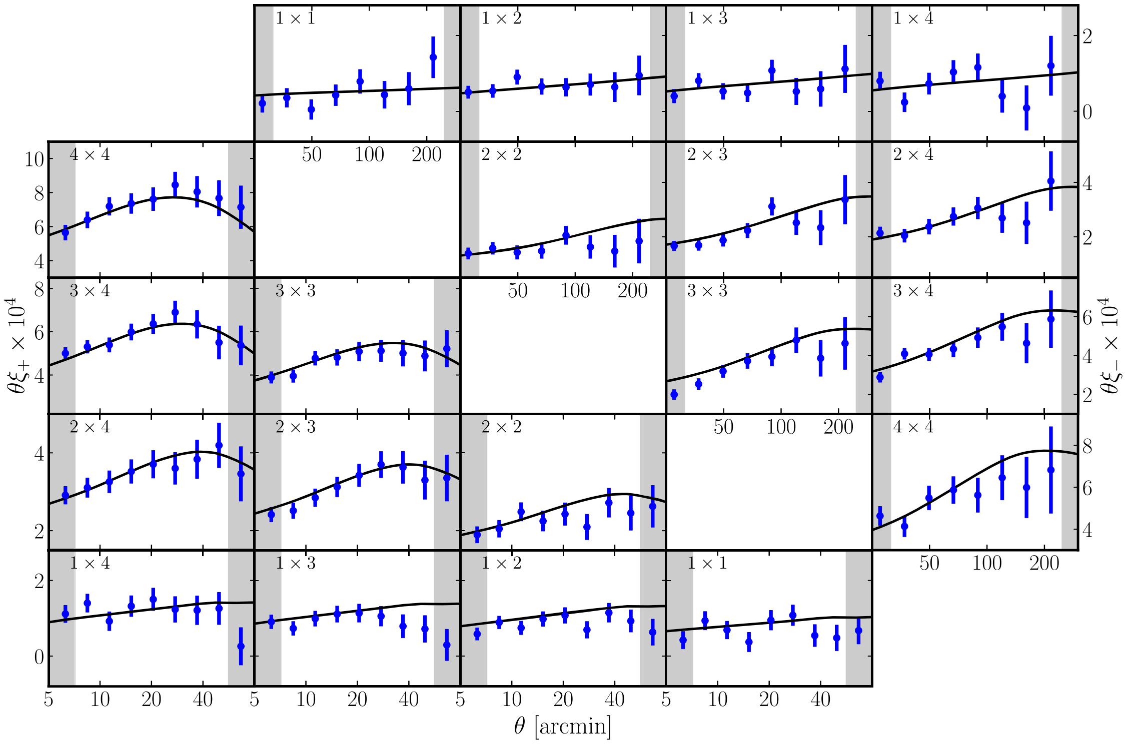

FIG. 3. The ten 2PCFs including four autocorrelations and six cross-correlations between the four tomographic redshift bins (labeled with 1–4). This plot shows the 2PCFs on scales 5.3 [arcmin] $< \theta <$ 76 [arcmin] for ξ_+, and 23.2[arcmin] $< \theta <$ 248 [arcmin] for ξ_-. The unshaded region refers to the fiducial scale cut: 7.1 [arcmin] $< \theta <$ 56.6 [arcmin] for ξ_+, and 31.2 [arcmin] $< \theta <$ 248 [arcmin] for ξ_-. The errorbars are estimated with mock catalogs. The total SNR of the measured 2PCFs is 26.6. The solid lines are the best-fit model of our fiducial analysis, as discussed in Sec. V A.

B. Covariance

We derive a covariance matrix of the estimated 2PCFs using the 1404 HSC mock shear catalogs summarized in Sec. II E with different realizations of galaxy intrinsic shape, measurement error from image noise, and cosmic shear signal [59]. We measure the 2PCFs from all 1404 realizations of mock catalogs in the same manner as the measurement from the real HSC shear catalog and calculate the covariance matrix from these 1404 measurements. The covariance matrix is denoted as $\boldsymbol{C}$, and the correlation coefficients, defined as $\rho_{ij} \equiv C_{ij}/\sqrt{C_{ii}C_{jj}}$, are shown in Fig. 4. We inspect the diagonal covariance elements with bootstrap resampling and confirm that each element of the covariance matrix has SNR greater than 21 ($\lesssim$5% statistical uncertainty), which indicates that the covariance is minimally affected by the finite number of realizations.

Since the cosmic shear signal in the mock catalogs are obtained from a large number of full-sky ray-tracing simulations of the WMAP9 cosmology which takes into account nonlinear structure formation [60], the derived cosmic variance includes both Gaussian and non-Gaussian information. Also, the galaxy positions and survey geometry in the mock catalogs mimic those of the real data; therefore the derived covariance includes super-survey covariance [59,71]. Moreover, we generate random shape noise and measurement error using the galaxy intrinsic shapes and measurement error from the real shear catalog [23]. We find that the shape noise covariance is prominent at the smallest angular bins, while the cosmic variance dominates the covariance at the largest angular bins.

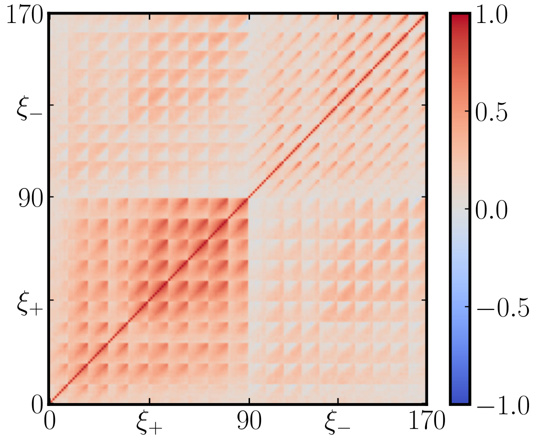

FIG. 4. The normalized covariance matrix (correlation coefficients) estimated with mock catalogs. Note that this plot shows the coefficients on scales 5.3 [arcmin] $< \theta <$ 76 [arcmin] for ξ_+, and 23.2 [arcmin] $< \theta <$ 248 [arcmin] for ξ_-. The fiducial scale cut—7.1 $< \theta <$ 56.6 [arcmin] for ξ_+, and 31.2 [arcmin] $< \theta <$ 248 [arcmin] for ξ_-—is a subset of this scale range.

The accuracy of the covariance matrix from the mocks was studied in detail by Shirasaki *et al.* [59]. They found that multiplicative bias of 10% can lead to a ~20% difference in the covariance from shape noise and measurement error. We already adopted the real value of multiplicative bias in the shear catalog, and thus have corrected for its effect. In addition, we correct for the bias from the effects of shell thickness, finite angular resolution and finite redshfit resolution in the ray-tracing simulations (for more details see Ref. [59]). Since we find the average 2PCFs measured from our simulations are lower than the theory prediction, and the ratio is approximately constant (0.81 on average) within our scale cuts for each redshift bin, we divide the 2PCF from each realization of mocks by the ratio in each bin.

One caveat in our covariance estimation is that we do not include dependence of the covariance on the cosmological parameters, since our mock catalogs are generated from a set of ray-tracing simulations adopting only one WMAP9 cosmology [60]. Kodwani *et al.* [72] used a Fisher analysis to study the dependence of the covariance matrix on the cosmological parameters and the resulting bias in the cosmology constraints when assuming a cosmology-independent covariance. They reported that the cosmology dependence of the covariance matrix does not significantly impact the cosmology constraints (to be more specific, parameters are only biased by $\leq 1\%$ of statistical uncertainties) for any current and future weak-lensing surveys. Following Kodwani *et al.* [72], we neglect the parameter dependence of the covariance matrix in our analysis.

C. *B*-modes

The measured 2PCFs $\xi_\pm$ include contributions from both curl-free gradient component (E-mode) and curl component (B-mode). However, the physical B-mode from a gravitational lensing potential, which can be caused by second-order lensing deflection [73], intrinsic alignments [37] and redshift clustering of source galaxies [63], is expected to be orders of magnitude smaller than the E-modes. Therefore, an estimate of the B-mode component can be used as a test for systematic errors. Following Schneider *et al.* [63], we separate the E-mode and B-mode components as

$$\xi^E_+(\theta) = \frac{1}{2}\left[\xi_+(\theta) + \xi_-(\theta) + \int_\theta^\infty \frac{\mathrm{d}\phi}{\phi}\xi_-(\phi)\left(4 - 12\frac{\theta^2}{\phi^2}\right)\right],$$

$$\xi^E_-(\theta) = \frac{1}{2}\left[\xi_+(\theta) + \xi_-(\theta) + \int_0^\theta \frac{\mathrm{d}\phi\phi}{\theta^2}\xi_+(\phi)\left(4 - 12\frac{\phi^2}{\theta^2}\right)\right],$$

$$\xi^B_+(\theta) = \frac{1}{2}\left[\xi_+(\theta) - \xi_-(\theta) - \int_\theta^\infty \frac{\mathrm{d}\phi}{\phi}\xi_-(\phi)\left(4 - 12\frac{\theta^2}{\phi^2}\right)\right],$$

$$\xi^B_-(\theta) = \frac{1}{2}\left[\xi_+(\theta) - \xi_-(\theta) + \int_0^\theta \frac{\mathrm{d}\phi\phi}{\theta^2}\xi_+(\phi)\left(4 - 12\frac{\phi^2}{\theta^2}\right)\right], \quad (12)$$

where $\xi_+(\theta) = \xi^E_+(\theta) + \xi^B_+(\theta)$ and $\xi_-(\theta) = \xi^E_-(\theta) - \xi^B_-(\theta)$. In order to compute the integrals in Eq. (12), we use a Riemann sum and measure $\xi_\pm$ with much finer log-intervals of $\Delta\log(\theta) = 0.02$ ranging from 0.2 arcmin to 415 arcmin. To compute the integral in ξ^B_+ (ξ^B_-) beyond (below) $\theta = 415$ arcmin ($\theta = 0.2$ arcmin), we extrapolate the measured ξ_- (ξ_+) beyond the interval with a WMAP9 cosmology. We confirm the result is not sensitive to the cosmology model (WMAP or *Planck* cosmology) for the extrapolation. We use the 1404 HSC-Y3 mock catalogs (introduced in Sec. II E) to calculate the errors on the estimated B-modes. Specifically, we conduct the same measurement on each mock realization, and derive the covariance matrix from the 1404B-modes measurement.

As seen in Fig. 5, the B-modes on the ξ_+ measurement are significant at large angular scales, especially in the high redshift bins. To reduce the influence of the B-modes on our cosmology constraints, we apply a scale cut on ξ_+ at scales with $\theta \geq 56.6$ arcmin. Although we do not find significant B-modes on ξ_-, we also apply a scale cut on ξ_- to remove scales with $\theta \geq 248$ arcmin since the data at such large scales is dominated by cosmic variance and contributes little to the SNR of the 2PCFs. Note that the cuts at small scales are imposed to reduce the modeling uncertainties of baryonic physics as will be shown in Sec. IV G. After the cuts at large scales, we find that the probability that the B-modes in the fiducial scale range is consistent with zero is $p = 0.143$ for ξ_+ and 0.237 for ξ_-, respectively.

IV. MODEL

In this section, we introduce the model, containing twenty-three free parameters as shown in Table II, to predict the tomographic cosmic shear 2PCFs $\xi^{ij}_\pm(\theta)$. Note that we coordinate with the Fourier-space cosmic shear analysis [39] when making the decision on model choices, and our fiducial model is the same as the Fourier space analysis. The parameters can be divided into two categories; eleven physical parameters and twelve systematic parameters. The physical parameters include five cosmological parameters, one baryonic feedback parameter and five intrinsic alignment parameters; the systematic parameters include four photo-z error parameters, four shear calibration bias parameters and four PSF systematic parameters. Our model is implemented in the public software: CosmoSIS [74]. We note that the model choices were set entirely before unblinding.

We coordinate our model choices with the parallel cosmic shear analysis using the pseudo-C_ℓ [39]. The analysis tests and choices described below have also been also adopted and described by [39].

With the flat-sky approximation, the 2PCFs can be expressed as the E and B modes of angular power spectra $C^{E/B}(\ell)$ via the Hankel transform,

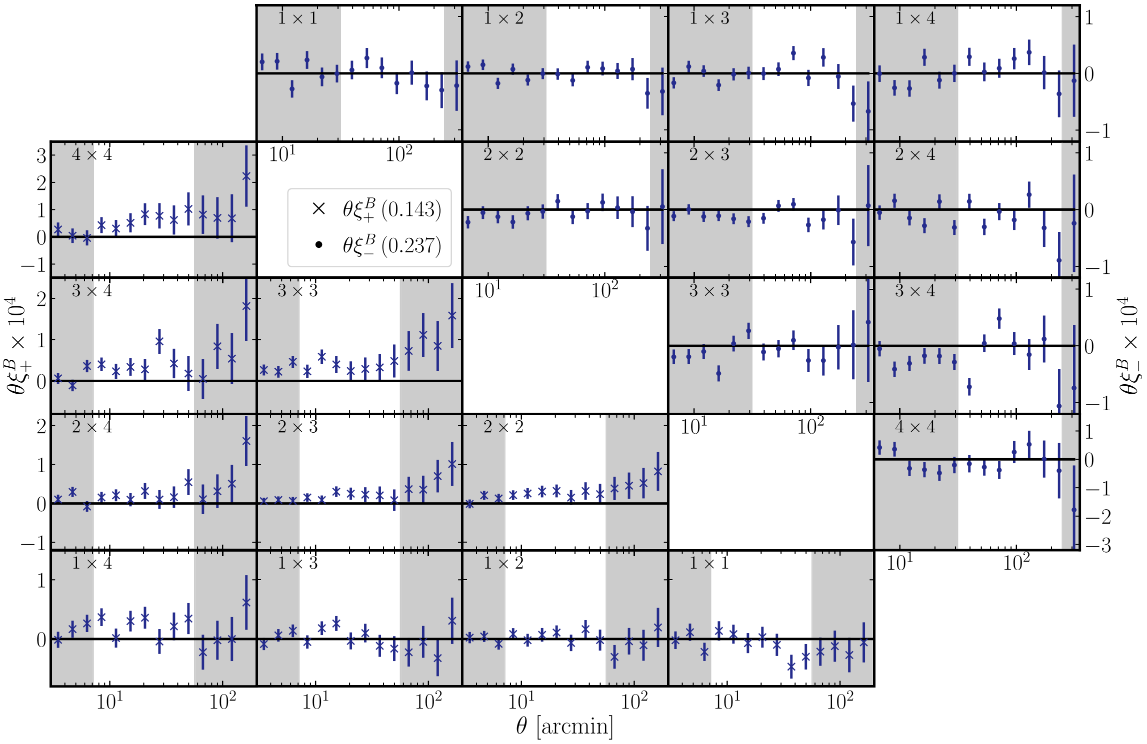

FIG. 5. B-modes on 2PCFs measured from the HSC-Y3 catalog in four tomographic bins. The p-value of the measured B-modes relative to a model of exactly zero is 0.1143 for ξ_+ and 0.1237 for ξ_-, as shown in the legend. The errorbars are estimated with mock catalogs. The unshaded region refers to the fiducial scale cut.

$$\xi^{ij}_{+/-}(\theta) = \frac{1}{2\pi}\int d\ell\,\ell J_{0/4}(\theta\ell)(C^{E;ij}(\ell) \pm C^{B;ij}(\ell)), \quad (13)$$

where $J_{0/4}$ are the zeroth/fourth-order Bessel functions of the first kind. In our analysis, the Hankel transform is computed with `FFTLog` [75] implemented in CosmoSIS. In Fig. 6, we demonstrate the integrands in Eq. (13) for different scales of $\xi_\pm$. As shown, $\xi_\pm$ in one angular bin corresponds to an integral over a wide range of ℓ s; therefore, our cosmic shear analysis based on 2PCFs is sensitive to information on different scales from the Fourier space analysis [39]. In a companion paper [39], we measure pseudo-C_ℓs and reconstruct angular power spectra $C_\ell^{E/B;ij}$ from the HSC-Y3 shear catalog.

The observed galaxy shapes are determined by both foreground lensing shear and the intrinsic shapes induced by the torques from the local environment. The spatial correlation between intrinsic shapes is known as intrinsic alignment (IA) [76]. Therefore, the E-mode angular power spectra in Eq. (13) can be decomposed into lensing-lensing autospectra ($C_{\rm GG}^{E;ij}$), intrinsic-intrinsic autospectra ($C_{\rm II}^{E;ij}$) and lensing-intrinsic cross-power spectra between lensing and IA ($C_{\rm GI}^{E;ij}$) [76]. Although the B-mode induced by lensing shear is negligible, a significant B-mode angular power spectrum can be produced by high-order IA models.

$$C^{E;ij} = C_{\rm GG}^{E;ij} + C_{\rm II}^{E;ij} + C_{\rm GI}^{E;ij} + C_{\rm GI}^{E;ji},$$
$$C^{B;ij} = C_{\rm II}^{B;ij}. \quad (14)$$

As shown in Sec. III C, the measured B-mode signal within our fiducial scale cuts is not significant, so we set this component to zero in our analysis. The E-mode lensing angular power spectra ($C^E_{GG;ij}$) is related to the matter power spectrum. Our implemented model for the matter power spectra is introduced in Sec. IV A. Our implemented IA model is introduced in Sec. IV B. Systematics are described by twelve parameters in our model, which include uncertainties in photo-z estimation (see Sec. IV C), uncertainties in shear calibration (see Sec. IV D) and PSF related systematic uncertainties (see Sec. IV E). Finally, the Monte Carlo Bayesian analysis used to constrain the free parameters is introduced in Sec. IV F.

A. Matter power spectra

We first connect the lensing angular power spectrum $C_{\rm GG}^{ij}(\ell)$ in Eq. (14) to the power spectrum $P_{\rm m}(k,z)$ of the matter distribution in the Universe at different redshifts. In a spatially flat universe, the lensing angular power spectrum encodes information of the matter power spectrum, $P_{\rm m}(k,\chi)$ according to the Limber approximation [77,78],

TABLE II. Model parameters and priors used in our fiducial cosmological parameter inference. The label $\mathcal{U}(a,b)$ denotes a noninformative flat prior between a and b, and $\mathcal{N}(\mu,\sigma)$ denotes a normal distribution with mean μ and width σ.

Parameter	Prior
Cosmological parameters (Sec. IV A)	
Ω_m	$\mathcal{U}(0.1, 0.7)$
$A_\mathrm{s}(\times 10^{-9})$	$\mathcal{U}(0.5, 10)$
n_s	$\mathcal{U}(0.87, 1.07)$
h_0	$\mathcal{U}(0.62, 0.80)$
ω_b	$\mathcal{U}(0.02, 0.025)$
Baryonic feedback parameters (Sec. IV A)	
A_b	$\mathcal{U}(2, 3.13)$
Intrinsic alignment parameters (Sec. IV B)	
A_1	$\mathcal{U}(-6, 6)$
η_1	$\mathcal{U}(-6, 6)$
A_2	$\mathcal{U}(-6, 6)$
η_2	$\mathcal{U}(-6, 6)$
b_ta	$\mathcal{U}(0, 2)$
Photo-z systematics (Sec. IV C)	
Δz_1	$\mathcal{N}(0, 0.024)$
Δz_2	$\mathcal{N}(0, 0.022)$
Δz_3	$\mathcal{U}(-1, 1)$
Δz_4	$\mathcal{U}(-1, 1)$
Shear calibration biases (Sec. IV D)	
Δm_1	$\mathcal{N}(0.0, 0.01)$
Δm_2	$\mathcal{N}(0.0, 0.01)$
Δm_3	$\mathcal{N}(0.0, 0.01)$
Δm_4	$\mathcal{N}(0.0, 0.01)$
PSF systematics (Sec. IV E)	
$\alpha'^{(2)}$	$\mathcal{N}(0, 1)$
$\beta'^{(2)}$	$\mathcal{N}(0, 1)$
$\alpha'^{(4)}$	$\mathcal{N}(0, 1)$
$\beta'^{(4)}$	$\mathcal{N}(0, 1)$

$$C^{ij}_{\mathrm{GG}}(\ell) = \int_0^{\chi_H} d\chi \frac{q_i(\chi) q_j(\chi)}{\chi^2} P_\mathrm{m}\left(k = \frac{\ell + 1/2}{\chi}; \chi\right), \quad (15)$$

where χ is the radial comoving distance, χ_H is the distance to the horizon (the maximum distance one could possibly observe[2]), and $q_i(\chi)$ is the lensing efficiency in the ith redshift bin defined as

$$q_i(\chi) = \frac{3}{2}\Omega_\mathrm{m}\left(\frac{H_0}{c}\right)^2 \frac{\chi}{a(\chi)} \int_\chi^{\chi_H} d\chi' n_i(\chi') \frac{\chi' - \chi}{\chi'}, \quad (16)$$

where Ω_m and H_0 are the matter density and Hubble parameter ($H_0 = 100\ h_0$ [km/s/Mpc]) at redshift zero, a is the cosmology scale factor, and $n_i(\chi)$ is the normalized redshift distribution of the galaxy in the ith redshift bin [see Sec. IV C for the modeling of $n_i(z)$]. Note that χ is given as a function of redshift as $\chi = \chi(z)$, so we compute the nonlinear matter power spectrum $P_\mathrm{m}(k; z)$ for an input set of k and z given $\chi = \chi(z)$.

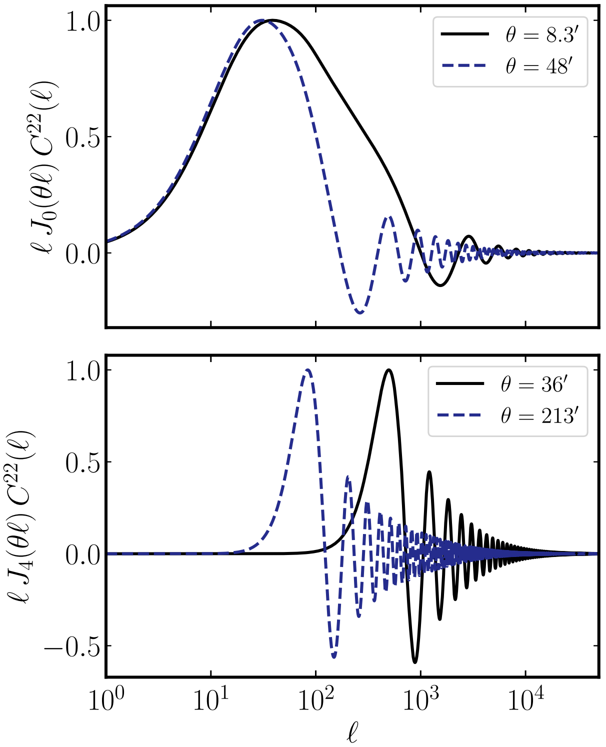

FIG. 6. The integrands in Eq. (13) which transform angular power spectra to correlation functions. We show the integrands for the smallest and largest angular bins for ξ_+ and ξ_-, respectively, for the correlation functions of the second redshift bin with itself.

1. Linear and nonlinear power spectra

At large scales in the early Universe, the structure grows according to linear perturbation theory. For a flat ΛCDM cosmology, the linear matter power spectrum is determined by the five cosmological parameters in Table II, including the matter density parameter (Ω_m), the amplitude (A_s) and the tilt (n_s) parameters of the power spectrum of the primordial curvature perturbations, the dimensionless Hubble parameter (h) and $\omega_\mathrm{b} \equiv \Omega_\mathrm{b} h^2$, where Ω_b is the baryon density parameter. In our analyses, we set the sum of neutrino mass $\sum m_\nu = 0.06$ eV. The linear power spectrum can be accurately computed by solving the Einstein-Boltzmann equations which describe the coevolution of the different components in the Universe (e.g., dark energy, dark matter, baryonic matter, radiation). The linear power spectrum of matter density field can be computed with public codes such as CAMB [79], and CLASS [80,81]. These public codes solve the coupled set of differential equations at first order according to linear perturbation theory, and compute the linear matter power spectrum.

---

[2] We note that, in this paper, we only model the structure up to $z = 4$.

TABLE III. The supported range for five cosmological parameters in BACCO emulator, where $\Omega_b = \omega_b/h^2$.

Parameter	Supported range
Ω_m	$\mathcal{U}(0.06, 0.7)$
$A_s(\times 10^{-9})$	$\cdots$
h_0	$\mathcal{U}(0.5, 0.9)$
Ω_b	$\mathcal{U}(0.03, 0.07)$
n_s	$\cdots$

At small scales, structure growth is nonlinear and cannot be described by a linear perturbation theory. Therefore, one has to resort to cosmological N-body simulations to model the matter power spectrum at nonlinear scales. Many empirical models calibrated against high-resolution N-body simulations have been proposed to calculate the nonlinear matter power spectrum, including HaloFit [82] and HMCode [30,83,84]. In modern cosmology analysis pipelines, emulators are broadly adopted to improve the computational speed of the matter power spectrum. They are constructed by running a large number of cosmological simulations with different input cosmological and astrophysical parameters, and interpolating the power spectrum between these parameters. These emulators can efficiently compute both linear [85–87] and nonlinear [31,87–89] power spectra with percent-level accuracy.

In our fiducial analysis, we adopt the public BACCO emulator [85] (version 1.0.0)[3] to compute the linear matter power spectrum. BACCO is a neural network emulator trained with more than 200,000 linear-matter power spectra computed with CLASS in the wave-number range between 10^{-4} and $50[h\ \mathrm{Mpc}^{-1}]$. The supported range of the cosmological parameters of the BACCO emulator is shown in Table III. The BACCO emulator is not limited by boundaries in A_s and n_s since it emulates the transfer function of the linear power spectrum [85]. In order to model the nonlinear matter power spectrum, we use HMCode [84] 2016, which is a variant of the halo model with physically motivated parameters calibrated with N-body and hydrodynamical simulations [30,83,84].

In our analysis pipeline, we adopt wide flat priors on the five cosmological parameters: Ω_m, A_s, n_s, h, and ω_b. However, we note that a flat prior on A_s leads to an informative prior on Ω_m and S_8 due to the degeneracies between these parameters. In order to obtain a chain with uniform prior on the (Ω_m, S_8) plane, we follow Sugiyama *et al.* [8] to apply a weight $w = \sigma_8/A_s$, which is the determinant of the Jacobian for the coordinate transform from $(\Omega_m, A_s, \ldots)$ to $(\Omega_m, S_8, \ldots)$, to the MC chain sampled with the flat prior on A_s to obtain a chain with uniform prior on Ω_m and S_8. We refer the readers to Sugiyama *et al.* [8] for more details. Our priors are coordinated to be the same with Dalal *et al.* [39], and the reasons for adopting flat prior on A_s are discussed in details in Dalal *et al.* [39].

2. *Baryonic feedback*

The matter power spectrum at small scales is significantly supressed by baryonic effects such as feedbacks from supernova and active galactic nuclei (AGN) (at $k \sim 10\ h/\mathrm{Mpc}$) as well as cooling and star formation.

We follow Asgari *et al.* [6] to adopt HMCode 2016 [84] to empirically model baryonic effects on the matter power spectrum. HMCode 2016 parameterizes the effect of baryonic feedback with a halo bloating parameter η_b and the amplitude of the halo mass-concentration relation A_b [83,84]. This baryonic model is calibrated with hydrodynamical simulations. We follow Joachimi *et al.* [90] to set the bloating parameter as a function of the amplitude parameter:

$$\eta_b = 0.98 - 0.12 A_b. \tag{17}$$

To be more specific, we use HMCode 2016 to model the supression from baryonic feedbacks on small scales of power spectrum with a flat prior: $A_b \in [2, 3.13]$ as shown in Table II. We marginalize over the amplitude parameter A_b when constraining our cosmological parameters. In HMCode 2016, $A_b = 3.13$ corresponds to the matter power spectrum without baryonic feedback (i.e. the spectrum obtained from dark matter only simulations). The latest version of HMCode is HMCode 2020 [30], which improves the modeling of the nonlinear matter power spectrum with very large neutrino mass, i.e., $m_\nu > 0.5$ eV. However, our analysis focuses on the ΛCDM cosmology with $\sum m_\nu = 0.06$ eV, and the computational speed of HMCode 2016 is about 1.5 times faster than HMCode 2020. Therefore, we adopt HMCode 2016 as our fiducial model.

It is worth noting that that there are other approaches to model the baryonic effects on the matter power spectrum, including baryonic correction models [91] and approaches based on principal component analysis (PCA) [92].

B. Intrinsic alignment

In a spatially flat universe, the IA angular power spectrum between two redshift bins i and j is related to the integrated 3D IA power spectrum via the Limber approximation:

$$C^{ij}_{\mathrm{II}}(\ell) = \int_0^{\chi_H} \mathrm{d}\chi \frac{n_i(\chi) n_j(\chi)}{\chi^2} P_{\mathrm{II}}\left(k = \frac{\ell + 1/2}{\chi}; \chi\right),$$

$$C^{ij}_{\mathrm{GI}}(\ell) = \int_0^{\chi_H} \mathrm{d}\chi \frac{q_i(\chi) n_j(\chi)}{\chi^2} P_{\mathrm{GI}}\left(k = \frac{\ell + 1/2}{\chi}; \chi\right), \tag{18}$$

where q_i is the lensing efficiency defined in Eq. (16). The II (GI) refers to the correlation between intrinsic shape and intrinsic shape (lensing shear and intrinsic shape). There are

---

[3] https://bitbucket.org/rangulo/baccoemu/src/master/.

many ways to model the II and GI power spectra, and, in this paper, we consider two model choices:

(i) the tidal alignment and tidal torque model (TATT; [37]); and

(ii) the nonlinear alignment model (NLA; [35,36]).

TATT is built on nonlinear perturbation theory assuming the intrinsic galaxy shapes are determined by the tidal field and the density field of matter. Following Secco *et al.* [7], we only keep the quadratic perturbation terms, and the IA power spectra are given by

$$\begin{aligned} P^E_{\mathrm{GI}}(k) &= c_1 P_\delta(k) + b_{\mathrm{ta}} c_1 P_{0|0E}(k) + c_2 P_{0|E2}(k), \\ P^E_{\mathrm{II}}(k) &= c_1^2 P_\delta(k) + 2 b_{\mathrm{ta}} c_1^2 P_{0|0E}(k) \\ &\quad + b^2_{\mathrm{ta}} c_1^2 P_{0E|0E}(k) + c_2^2 P_{E2|E2}(k) \\ &\quad + 2 c_1 c_2 P_{0|E2}(k) + 2 b_{\mathrm{ta}} c_1 c_2 P_{0E|E2}(k), \\ P^B_{\mathrm{II}}(k) &= b^2_{\mathrm{ta}}(k) c_1^2 P_{0B|0B}(k) + c_2^2 P_{B2|B2}(k) \\ &\quad + 2 b_{\mathrm{ta}} c_1 c_2 P_{0B|B2}(k). \end{aligned} \tag{19}$$

The subscripts of the tidal field power spectra on the right-hand side indicate correlations between different order terms in the expansion of the matter field, and these power spectra are calculated to one-loop order using the public software; FAST-PT v2.1 [93,94].[4] We refer the readers to Blazek *et al.* [37] for more details. The redshift-dependent amplitudes c_1 and c_2 are defined as

$$\begin{aligned} c_1(z) &= -A_1 \frac{\bar{C}\rho_{\mathrm{c}}\Omega_{\mathrm{m}}}{D(z)} \left(\frac{1+z}{1+z_0}\right)^{\eta_1}, \\ c_2(z) &= 5 A_2 \frac{\bar{C}\rho_{\mathrm{c}}\Omega_{\mathrm{m}}}{D^2(z)} \left(\frac{1+z}{1+z_0}\right)^{\eta_2}, \end{aligned} \tag{20}$$

where $D(z)$ is the growth function, ρ_{crit} is the critical density, $z_0 = 0.62$ is the pivot redshift, and $\bar{C} = 5 \times 10^{-14} M_\odot h^{-2}\ \mathrm{Mpc}^2$ is obtained from `SuperCOSMOS` [95]. The TATT IA model has five free parameters; $A_1, A_2, \eta_1, \eta_2, b_{\mathrm{ta}}$. The power-law terms in Eq. (20) with two free parameters (η_1, η_2) are used to model the possible redshift evolution beyond what is already encoded in the model; A_1 and A_2 capture the IA power spectra that scale linearly and quadratically with the tidal field. The bias parameter b_{ta} models the fact that galaxies are oversampled in the highly clustered regions. In this paper, we adopt wide flat priors on the TATT model parameters; $A_1, A_2, \eta_1, \eta_2 \in [-6, 6]$, $b_{\mathrm{ta}} \in [0, 2]$. This is because the IA signal is very sensitive to the properties (e.g., color, magnitude) of the galaxy sample [96,97], thus it is very difficult to derive reliable Gaussian priors on the TATT model parameters for the galaxy sample in the shear catalog.

NLA is a more commonly used IA model, which is a subspace of TATT with $A_2 = 0$ and $b_{\mathrm{ta}} = 0$. The NLA model is built upon the assumption that intrinsic galaxy shapes are aligned linearly with the tidal field. Under this assumption, the GI and II power spectra are

$$P^E_{\mathrm{GI}} = c_1(z) P_\delta, \qquad P^E_{\mathrm{II}} = c_1^2(z) P_\delta, \tag{21}$$

where the redshift-dependent amplitude $c_1(z)$ is defined in Eq. (20). Our implementation of the NLA model has two free parameters, A_1 and η_1, and we adopt wide flat priors on them: $A_1, \eta_1 \in [-6, 6]$. The NLA model here is different from the original linear alignment model [35,36] as P_δ in Eq. (21) is not the linear matter power spectrum but the full matter power spectrum including nonlinear structure growth and baryonic feedback (in our fiducial analysis, the matter power spectrum is predicted by HMCode). Another difference to the original model is that our implementation of NLA also includes a redshift evolution described by a power law in $c_1(z)$ to capture additional redshift evolution as shown in Eq. (20).

Campos *et al.* [98] proposed to select the proper IA model with an empirical approach based on the difference in χ^2 between models applied to the real data. We analyze all the blinded data vectors with both TATT and NLA. For each setup, we look at the difference in the S_8 estimates and the resulting χ^2 of the analyses. We do not see a significant difference in the projected posterior of S_8 ($\Delta S_8 \sim 0.4\sigma$) nor significant difference in χ^2 between these two setups. Furthermore, TATT and NLA also give comparable errors on the projected posterior of S_8. We decide to use TATT as our fiducial model, since it is a more complete model of IA, and it does not degrade our constraints.

C. Photometric redshift

As shown in Eq. (16), the redshift distributions in four redshift bins, $n_i(z)$ $(i = 1, 2, 3, 4)$, of the source galaxies are essential ingredients for modeling the shear-shear angular power spectra C^{ij}_ℓ, where i and j are the indices of the tomographic redshift bins. The HSC-Y3 redshift distributions and their uncertainties are inferred jointly by the photometric redshift estimation, described in Sec. II C, and by spatial cross-correlations between the HSC-Y3 shape catalog and the CAMIRA-LRG catalog [25,26,99]. Here we provide a brief overview of the inference process, and we refer the readers to Rau *et al.* [24] for the details.

The redshift distribution of each tomographic bin is modeled as a discrete probability density function on redshift grids ranging from $z = 0$ to $z = 4$, with a 0.025 step size. In Fig. 2 (black lines), we show the $n_i(z)$ distributions of the joint redshift estimation. The redshift distributions shown are modeled as a logistic Gaussian process, of which the parameters are inferred by

(i) the `dNNz` photo-z estimation and a model for the cosmic variance for all redshifts; and

---

[4] https://github.com/JoeMcEwen/FAST-PT.

(ii) cross-correlation between the photometric samples and the CAMIRA-LRG samples between $z = 0.0$ and 1.2.

We note that the CAMIRA-LRG sample (the grey histogram in Fig. 2), which is used for cross-correlation calibration, covers only part of the redshift range of bin 3, and does not cover any of bin 4.

In order to quantify and marginalize over the redshift distribution uncertainty, we allow the mean redshift distribution of each bin to shift by Δz_i, namely,

$$n_i(z) \to n_i(z + \Delta z_i). \tag{22}$$

Zhang *et al.* [100] demonstrated that this shift model is sufficient for capturing the uncertainty in redshift distribution for the HSC-Y3 cosmic shear analysis, and is computationally inexpensive, thus we use it here. As a result, four extra redshift parameters corresponding to four tomographic bins are included in the fiducial analysis of this work.

Rau *et al.* [24] derived the priors on Δz_i using the model difference, i.e., differences of the inferred $n_i(z)$ between three photometric redshift models (see Fig. 2) and the reference CAMIRA-LRG sample. We refer the readers to Sec. V.7 of Rau *et al.* [24] for more details on how the priors are determined.

Taking into account the fact that the redshift distributions of galaxies in bin 3 and bin 4 are only partially calibrated by spatial cross-correlation with CAMIRA-LRGs, we compare the cosmological constraints with two types of priors on the redshift shifting errors Δz_i in Sec. V D. These two types of priors are summarized as follows:

(i) Informative Gaussian priors estimated by Rau *et al.* [24] for four redshift bins. The priors for the first two redshift bins are shown in Table II, and the last two redshift bins are $\mathcal{N}(0, 0.031)$ and $\mathcal{N}(0, 0.034)$, respectively.

(ii) Informative Gaussian priors [24] for bin 1 and bin 2; and uninformative flat priors between −1 and 1 for bin 3 and bin 4.

As will be shown in Sec. V D, we find that when adopting the uninformative flat prior on bin 3 and bin 4, the posteriors on Δz_3 and Δz_4 are not consistent with zero, indicating that the true redshift distributions of the last two redshift bins are higher by $\Delta z \sim 0.1$ than that estimated by [24]. This result is seen in each of the three blinded catalogs. In Sec. V D, we simulate noisy mock data vectors for the three blinded catalogs and find that such large positive values for Δz_3 and Δz_4 are not likely be due to statistical uncertainties, and thus are likely to be real. Furthermore, the estimate of S_8 is $\sim 1\sigma$ higher for the analysis using the informative Gaussian priors on bin 3 and bin 4. Therefore, we suspect that the photo-z inferred redshift distributions of the last two redshift bins are systematically biased. We leave the calibration of high redshift bins and their impact on cosmic shear to future studies. The fiducial priors on the Δz_i are listed in Table II.

D. Shear calibration bias

As presented in [23], our shear catalog is calibrated with image simulations downgrading the HST images in F814W band to the HSC observational conditions. Specifically, we model and calibrate the shear estimation bias including galaxy model bias [101], noise bias [102], selection bias [103], and detection bias [104] using realistic image simulations. In addition, we confirm that the shear estimation bias due to the blending of galaxies located at different redshifts is small for the HSC-Y3 weak-lensing science.

We also model and marginalize over the uncertainties from the multiplicative bias residual after the aforementioned calibration due to the assumptions and the limited galaxy number in the simulations. To be more specific, we follow [38] to introduce a nuisance parameter $\Delta m^{(i)}$ to the ith redshift bin (where $i = 1, \ldots 4$) to represent the redshift-dependent multiplicative bias residual. The theoretical prediction for the cosmic shear 2PCFs is modified as

$$\xi^{ij}(\theta) \to (1 + \Delta m_i)(1 + \Delta m_j)\xi^{ij}(\theta). \tag{23}$$

The prior range of Δm_i is taken to be Gaussian with zero mean and a standard deviation of 0.01, which is motivated by the calibration of the HSC-Y3 shear catalog based on image simulations [23] since it is confirmed that the multiplicative bias residual is controlled below the 1% level.

E. PSF systematics model

In this section, we describe the model for PSF-related additive systematics in this work. The additive bias changes the shear signal as $\gamma \to \gamma + \gamma_{\rm sys}$. As Zhang *et al.* [28] found, in addition to the second-order radial moments of the PSF, the spin-2 component of the fourth-order PSF moments can also cause significant leakage and modeling errors in shear for the `reGauss` shear estimator. Therefore, we include both second-order and fourth-order PSF shapes in the model for the PSF additive bias as

$$\gamma_{\rm sys} = \alpha^{(2)} e^{(2)}_{\rm psf} + \beta^{(2)} \Delta e^{(2)}_{\rm psf} + \alpha^{(4)} M^{(4)}_{\rm psf} + \beta^{(4)} \Delta M^{(4)}_{\rm psf}, \tag{24}$$

where the first and third terms are the PSF leakage bias by the PSF second- and fourth-order moments, and the second and fourth terms are the PSF modeling error in the second- and fourth-order moments.

We find the prior on the PSF systematics parameters by cross-correlating the shapes and the shape modeling errors of PSF stars with the galaxy shapes. The cross-correlations are modeled by

$$\langle \hat{\gamma}_{\mathrm{gal}} e^{(2)}_{\mathrm{psf}} \rangle = \alpha^{(2)} \langle e^{(2)}_{\mathrm{psf}} e^{(2)}_{\mathrm{psf}} \rangle + \beta^{(2)} \langle \Delta e^{(2)}_{\mathrm{psf}} e^{(2)}_{\mathrm{psf}} \rangle + \alpha^{(4)} \langle M^{(4)}_{\mathrm{psf}} e^{(2)}_{\mathrm{psf}} \rangle + \beta^{(4)} \langle \Delta M^{(4)}_{\mathrm{psf}} e^{(2)}_{\mathrm{psf}} \rangle \tag{25}$$

$$\langle \hat{\gamma}_{\mathrm{gal}} \Delta e^{(2)}_{\mathrm{psf}} \rangle = \alpha^{(2)} \langle e^{(2)}_{\mathrm{psf}} \Delta e^{(2)}_{\mathrm{psf}} \rangle + \beta^{(2)} \langle \Delta e^{(2)}_{\mathrm{psf}} \Delta e^{(2)}_{\mathrm{psf}} \rangle + \alpha^{(4)} \langle M^{(4)}_{\mathrm{psf}} \Delta e^{(2)}_{\mathrm{psf}} \rangle + \beta^{(4)} \langle \Delta M^{(4)}_{\mathrm{psf}} \Delta e^{(2)}_{\mathrm{psf}} \rangle \tag{26}$$

$$\langle \hat{\gamma}_{\mathrm{gal}} M^{(4)}_{\mathrm{psf}} \rangle = \alpha^{(2)} \langle e^{(2)}_{\mathrm{psf}} M^{(4)}_{\mathrm{psf}} \rangle + \beta^{(2)} \langle \Delta e^{(2)}_{\mathrm{psf}} M^{(4)}_{\mathrm{psf}} \rangle + \alpha^{(4)} \langle M^{(4)}_{\mathrm{psf}} M^{(4)}_{\mathrm{psf}} \rangle + \beta^{(4)} \langle \Delta M^{(4)}_{\mathrm{psf}} M^{(4)}_{\mathrm{psf}} \rangle \tag{27}$$

$$\langle \hat{\gamma}_{\mathrm{gal}} \Delta M^{(4)}_{\mathrm{psf}} \rangle = \alpha^{(2)} \langle e^{(2)}_{\mathrm{psf}} \Delta M^{(4)}_{\mathrm{psf}} \rangle + \beta^{(2)} \langle \Delta e^{(2)}_{\mathrm{psf}} \Delta M^{(4)}_{\mathrm{psf}} \rangle + \alpha^{(4)} \langle M^{(4)}_{\mathrm{psf}} \Delta M^{(4)}_{\mathrm{psf}} \rangle + \beta^{(4)} \langle \Delta M^{(4)}_{\mathrm{psf}} \Delta M^{(4)}_{\mathrm{psf}} \rangle . \tag{28}$$

The left-hand side of Eqs. (25)–(28) are correlation functions between the galaxy shape and PSF moments, which we call the "g-p correlation." The correlation functions on the right hand side are PSF-PSF correlation functions, which we call the "p-p correlation." We show the measurements and the best-fit models of all four g-p correlations in Fig. 7 using the catalog with blinding ID 0, which incidentally happened to be the true shear catalog after unblinding. To find the prior for the PSF systematics parameters, we calculate covariance matrices for the g-p correlations of all three blinded catalogs using the mock catalogs described in Sec. II E. The prior of the true catalog (blinded catalog 0) are listed in Table II. Since Zhang *et al.* [28] found that $\alpha^{(2)}$ and $\alpha^{(4)}$ are correlated, we include the correlation between all PSF parameters in the prior. The correlation between the PSF parameters does not impact the results significantly, which is consistent with the finding in Zhang *et al.* [28].

Zhang *et al.* [28] find significant bias on ξ_+ due to PSF systematics, whereas the bias on ξ_- to be negligible. We model the impact of PSF additive bias on ξ_+ by

$$\xi_+(\theta) \to \xi_+(\theta) + \sum_{k=1}^{4} \sum_{q=1}^{4} p_k p_q \langle S_k S_q \rangle , \tag{29}$$

where $\boldsymbol{p} = (\alpha^{(2)}, \beta^{(2)}, \alpha^{(4)}, \beta^{(4)})$ is the parameter vector, and $\boldsymbol{S} = (e^{(2)}_{\mathrm{psf}}, \Delta e^{(2)}_{\mathrm{psf}}, M^{(4)}_{\mathrm{psf}}, \Delta M^{(4)}_{\mathrm{psf}})$ is the PSF moments vector. We note that the PSF additive systematics are added to the 2PCFs after the rescaling from multiplicative bias.

In order to account for the correlation in the prior of PSF systematic parameters, we sample four uncorrelated parameters, $\boldsymbol{p}' = (\alpha'^{(2)}, \beta'^{(2)}, \alpha'^{(4)}, \beta'^{(4)})$, with uncorrelated Gaussian priors. We then transform these parameters into our original parameters by the following invertible transform:

$$\boldsymbol{p} = \mathbf{T} \cdot \boldsymbol{p}' + \bar{\boldsymbol{p}}, \tag{30}$$

where $\bar{\boldsymbol{p}}$ is the average of the original PSF systematic parameters, $\mathbf{T} = \mathbf{V}^{\frac{1}{2}}\mathbf{U}$, $\mathbf{V}$ is a diagonal matrix with eigenvalues of $\boldsymbol{p} - \bar{\boldsymbol{p}}$'s covariance matrix as the diagonal elements, and each column of $\mathbf{U}$ is a eigenvector of the covariance matrix. In Sec. V D, we show that the bias from

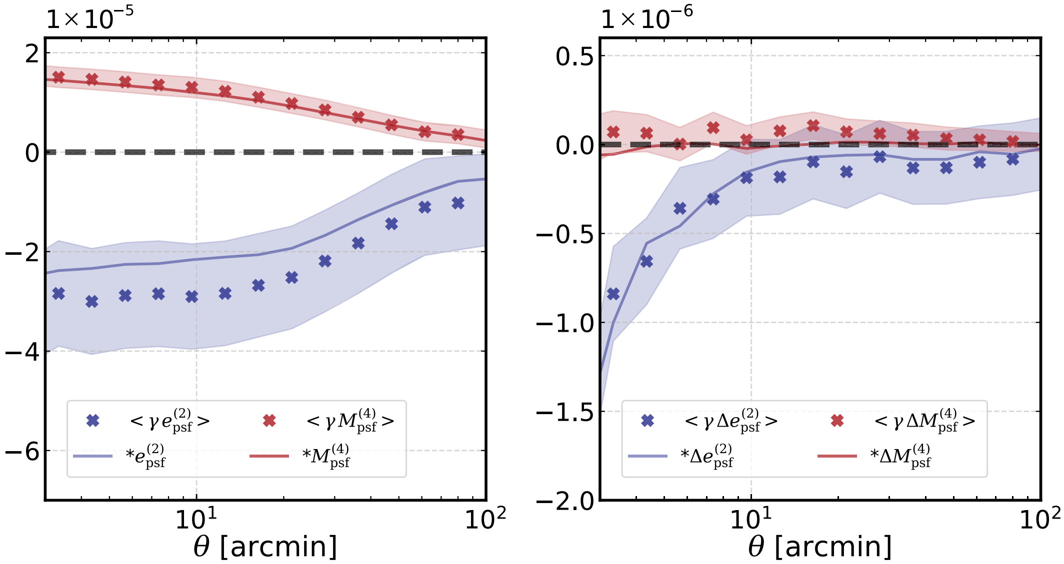

FIG. 7. Galaxy-star correlations, including cross-correlations between galaxy shape and star shape (left panel), and also between galaxy shape and star shape errors (right panel). We show the correlations to both second- ($e^{(2)}_{\mathrm{psf}}$) and fourth-order ($M^{(4)}_{\mathrm{psf}}$) star shapes and star shape errors. The points are the measurements from HSC data, and the solid lines are the best-fit model using star-star correlations [see Eqs. (25)–(28)].

not including the correlation between $\alpha^{(2)}$ and $\alpha^{(4)}$ is negligible for HSC-Y3 cosmic shear analysis.

Zhang *et al.* [28] conducted other extensive mock tests, where they investigated PSF systematics models taking into account redshift dependency, second-order terms, and PSF versus non-PSF stars. They found that the above modeling of PSF additive systematics is sufficient for the HSC-Y3 cosmic shear analysis. We refer the readers to Zhang *et al.* [28] for further details about PSF additive systematics in the HSC-Y3 shear catalog.

F. Bayesian inference

We use a Monte Carlo Bayesian analysis to sample the posterior in the 23-dimensional space of the cosmological, astrophysical and systematic parameters. We denote the vector of parameters as $\Theta = (\Omega_\mathrm{m}, A_s, h_0, \ldots)$, and the model prediction of 2PCFs, with 140 dimensions (14 angular bins for each of the 10 correlation functions across 4 redshift bins), as $\xi_\pm(\Theta)$. We adopt a Gaussian likelihood $\mathcal{L}$:

$$\ln \mathcal{L}(\hat{\xi}_\pm|\Theta) = -\frac{1}{2}(\hat{\xi}_\pm - \xi_\pm(\Theta))^T \mathbf{C}^{-1}(\hat{\xi}_\pm - \xi_\pm(\Theta)), \quad (31)$$

where $\hat{\xi}_\pm$ is the measured 2PCFs as shown in Fig. 3 and $\mathbf{C}$ is the covariance matrix estimated from 1404 mock catalogs with the WMAP9 cosmology, which is shown in Fig. 4. Note, as discussed in Sec. III B, we neglect the dependency of the covariance matrix on cosmological parameters. $\mathbf{C}^{-1}$ is the precision matrix, namely the inverse of the covariance matrix. When estimating the inverse matrix, we correct for noise bias by multiplying the numerical inverse of the noisy estimate of covariance by the Hartlap factor [65]: $(1404-140-2)/(1404-1) \sim 0.9$. With Bayesian inference, we construct a posterior probability distribution, denoted as $\mathcal{P}(\Theta|\hat{\xi}_\pm)$ for the parameters Θ, given the data vector $\hat{\xi}_\pm$,

$$\mathcal{P}(\Theta|\hat{\xi}_\pm) \propto \mathcal{L}(\hat{\xi}_\pm|\Theta)\Pi(\Theta), \quad (32)$$

where $\Pi(\Theta)$ is the prior distribution of Θ.

Markov Chain Monte Carlo (MCMC) and nested sampling are widely used in the cosmology community to sample posteriors in high-dimensional parameter space. MCMC methods directly generate samples from the posterior in high-dimensional parameter space, whereas nested samplers map the high-dimensional posterior onto a one-dimensional space and divide the posterior into many nested "slices." After generating samples from the "slices," they recombine the samples with appropriate weights to reconstruct the posterior. In this paper, we compare the constraints from three different samplers, EMCEE [105], `MultiNest` [106], and `PolyChord` [107] implemented in CosmoSIS:

(i) EMCEE is an affine-invariant ensemble sampler for MCMC.

(ii) `MultiNest` is a nested sampler using a k-means clustering algorithm with ellipsoid bounds.

(iii) `PolyChord` is a nested sampler using slice sampling to sample within the nested isolikelihoods contours.

TABLE IV. The setups of the three MC samplers. `PolyChord` has three hyperparameters; the number of live points, number of repetitions n_repeat, and tolerance `tol`. `Efr` is the sampling efficiency for `MultiNest`. EMCEE uses 10,000 samples with 80 walkers and `nstep`= 5.

`PolyChord`	`MultiNest`	EMCEE
$n_\mathrm{live} = 500$	$n_\mathrm{live} = 500$	$n_\mathrm{sample} = 10^4$
$n_\mathrm{repeat} = 20$	$n_\mathrm{efr} = 0.3$	$n_\mathrm{walker} = 80$
`tol` $= 0.01$	`tol` $= 0.05$	$n_\mathrm{step} = 5$

We use `PolyChord` for our fiducial analysis since, as pointed out by Lemos *et al.* [108], the marginalized posterior widths for Ω_m and σ_8 estimated by `MultiNest` are 10% smaller and are probably underestimated. Moreover, `MultiNest` gives a biased estimation of evidence. However, `MultiNest` is about five times faster than `PolyChord`, so we utilize `MultiNest` for our internal consistency tests. Since the estimated posterior widths from `MultiNest` are systematically smaller, it is conservative to use the posteriors from `MultiNest` for internal consistency tests. In addition, we compare the posteriors estimated from `PolyChord` and `MultiNest` to the estimation from EMCEE.

To assess the convergence of our chains, we check that, at the end of the chains, the normalized nested weight (the weight, at each estimation, divided by the maximum weight in the chains) has stopped increasing and is close to zero. In addition, we also use `nestcheck` [109], a public software,[5] to confirm that the posterior mass has peaked out, which indicates that most of the posterior mass contribution is well-sampled. Also, we confirm that the uncertainty of the S_8 posterior distribution is reasonably small. The setups for the three MC samplers are shown in Table IV.

We report the 1D marginalized mode and its asymmetric ±34% confidence intervals, together with the MAP estimated as the maximum of the posterior in the chain returned by the nested sampler,

$$\text{1D mode}^{+34\%\mathrm{CI}}_{-34\%\mathrm{CI}}\ (\text{MAP from nested chain}). \quad (33)$$

We note that the DES cosmic shear analysis [7,64] reported a projected mean estimated from the nested chain sampled with `PolyChord`; whereas KiDS reported the MAP estimated with MaxLike implemented in CosmoSIS as their reported point estimation, and they report a hybrid

---

[5] https://github.com/ejhigson/nestcheck.

confidence interval that is estimated on the joint, multidimensional highest posterior density region, but projected onto the marginal posterior of the parameter under consideration [110]. We choose to report the projected mode since it is less sensitive than the projected mean to the tails of the projected 1D posterior. In addition, the projected mode is more stable than the MAP, and its confidence interval is mathematically well-defined and simple to estimate.

G. Model validation

In our fiducial analysis, we use the BACCO emulator to model the linear matter power spectrum (Sec. IV A); HMCode 2016 for nonlinear matter power spectrum and baryonic feedback (Sec. IV A); and TATT for intrinsic alignment (Sec. IV B). The redshift distributions are calibrated by cross-correlating with CAMIRA-LRGs, and the redshift estimation error is modeled with shifting errors Δz, adopting a flat prior in the last two redshift bins (Sec. IV C). Additionally, we use redshift-dependent multiplicative bias residuals (Sec. IV D) and a PSF systematic model with fourth-order shape leakage and shape error (Sec. IV E). We perform Bayesian analysis using the nested sampler `PolyChord` (Sec. IV F).

We validate our model with noiseless synthetic 2PCFs simulated with different models for the matter power spectrum. We first make a baseline (systematics-free) simulation using the fiducial model and the $\Omega_{\rm m}$ and A_s from the WMAP9 cosmology, and other parameters are from the MAP of the cosmology constraint using the blinded catalog 0 with our fiducial setup. Then we change the models in the simulation pipeline to simulate "contaminated" data vectors, and check the biases of analyses on $\Omega_{\rm m}$ and S_8 for these "contaminated" data. Specifically, we test the following "contaminated" models:

(i) Simulation with CAMB linear power spectrum instead of the BACCO emulator.
(ii) Simulation with baryonic rescaling from OWLS-AGN [111,112] instead of HMCode 2016.
(iii) Simulation with nonlinear power spectrum from `MiraTitan II` emulator [31] and baryonic rescaling from OWLS-AGN instead of HMCode 2016.

We add the baryonic feedback into our synthetic data vectors using a rescaling scheme proposed by Amon *et al.* [64]. Specifically, the power spectrum with baryonic physics is simulated by multiplying a scale-dependent suppression factor to the dark-matter-only power spectrum—namely the HMCode 2016 nonlinear power spectrum without baryonic feedback ($A_{\rm b} = 3.13$) for our case,

$$P_{\rm m,b}(k,z) = \frac{P_{\rm hydro}(k,z)}{P_{\rm DM}(k,z)} P_m(k,z|A_{\rm b} = 3.13), \quad (34)$$

where $P_{\rm hydro}(k,z)$ is the power spectrum measured from hydrodynamic simulations (e.g., OWLS-AGN [111], COWLS [113], Illustris [114], MassiveBlack-II [115], Eagle [116], Horizon-AGN [117], and IllustrisTNG [118]), and $P_{\rm DM}(k,z)$ is the power spectrum measured from dark matter only simulations of the same suite.

In order to assure that the modeling errors from both baryonic physics and nonlinear structures for our fiducial scale cut defined in Sec. III A are not significant in our analysis, we follow the DES-Y3 cosmic shear analysis to check whether the amplitude of the 2D MAP estimation bias (denoted as $\boldsymbol{b}_{\rm 2D}$) on the plane of ($\Omega_{\rm m}$, S_8) is less than 0.3σ, when applying our fiducial model to the OWLS-AGN, CAMB, and `MiraTitan II` simulations:

$$\sqrt{\boldsymbol{b}_{\rm 2D}^T \boldsymbol{\Sigma}^{-1} \boldsymbol{b}_{\rm 2D}} < 0.3, \quad (35)$$

where $\boldsymbol{\Sigma}$ is the covariance matrix of the 2D posterior on the plane of ($\Omega_{\rm m}$, S_8) estimated from the first blinded catalog. In addition, to make sure that our model is not significantly influenced by the modeling, we test our fiducial model and scale cut with the synthetic simulation using both OWLS-AGN baryonic suppression and the `MiraTitan II` nonlinear power spectrum. In this paper, we adopt the CosmoSIS implementation of MaxLike[6] which is a wrapper of the SciPy minimizer, to estimate MAPs. To be more specific, we use the Nelder-Mead minimizer [119] with tolerance set to 10^{-6}. In order to reduce the numerical error in the MAP estimation, we follow Joachimi *et al.* [110] to run the minimizer with 50 different starting points and take the final MAP to be the result with the largest posterior. The starting points are varied in the parameters of interest in relation to the model choice, including three cosmology parameters $\Omega_{\rm m}$, A_s, $A_{\rm b}$ and four intrinsic alignment parameters, A_1, A_2, η_1 and η_2. Note, all 23 parameters vary during each MAP estimation, although the starting points are randomly sampled in only these seven dimensions. We find that the MAP estimate does not change when adding additional points for ~30 starting points. Our results are shown as "+" points in Fig. 8, and the maximum 2D bias we found is $\sim 0.2\sigma$ for the OWLS-AGN + `MiraTitan II` simulation, which is less than the requirement threshold of 0.3σ.

Furthermore, we check the influence of modeling errors on the 1D projected mode since it is the point estimation we will report as discussed in Sec. IV F. The results are shown as "×" points in Fig. 8. We find that the 1D biases on S_8 are about -0.14σ for all the simulations with our fiducial scale cut; however, the 1D biases on $\Omega_{\rm m}$ range from -0.4σ to -0.8σ for different simulations. The differences between the biases on MAPs and the biases on projected modes are mainly caused by projection effects in the projected point estimation. As shown in Joachimi *et al.* [110], the projection effects can cause about a 1σ bias on the 1D projected point

---

[6] https://github.com/joezuntz/cosmosis/tree/main/cosmosis/samplers/maxlike.

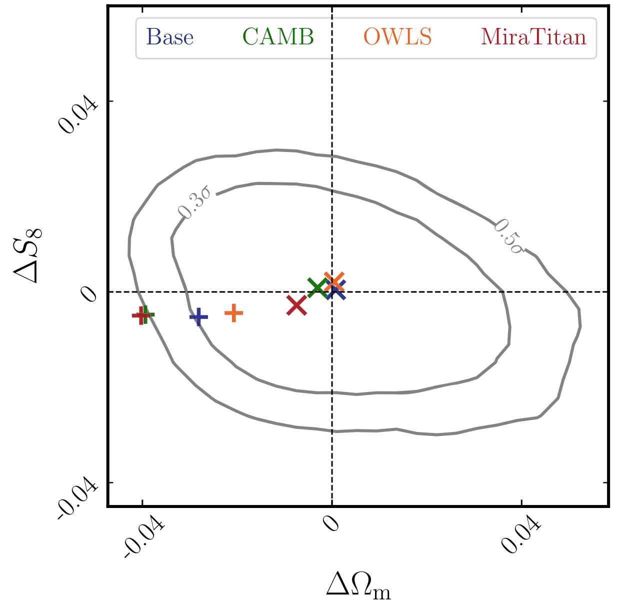

FIG. 8. The modeling errors (estimated parameters—true parameters) in the MAP ("×") and projected 1D mode ("+") when applying our model to different synthetic mocks of 2PCFs including (from left to right in the legend) the baseline simulation, simulation with the CAMB linear power spectrum, OWLS-AGN suppression, and the `MiraTitan II` nonlinear power spectrum. The gray lines are 0.3σ and 0.5σ contours of the 2D projected posterior in the parameter space of (Ω_m, S_8).

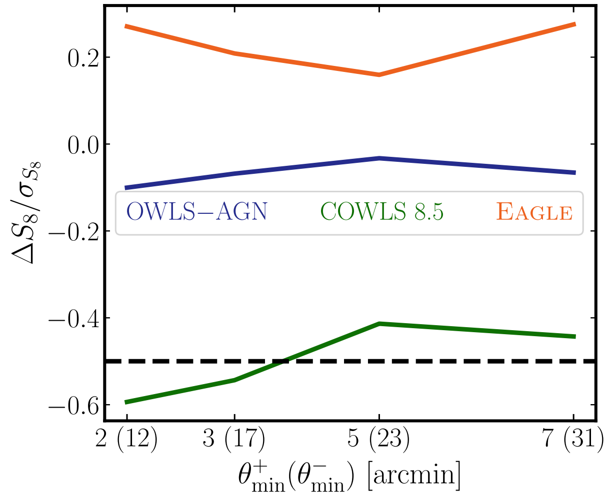

FIG. 9. Tests applying our fiducial model to synthetic mocks of 2PCFs from different hydrodynamic simulations. The y-axis is the modeling errors in the projected 1D mode (estimation—truth) relative to the 1σ uncertainty in the projected mode estimated by analyzing real data. The x-axis is the small-scale cut that we applied. We simultaneously vary the cut on ξ_+ (denoted as $\theta^+_{\rm min}$) and the cut on ξ_- (denoted as $\theta^-_{\rm min}$).

estimation. Based on the tests shown here we conclude that the bias (due to both modeling error and projection effects) on the 1D projected mode of S_8 is less than 0.15σ, which is not significant; however, the systematic uncertainty (from modeling error and projection effects) on the 1D projected mode of Ω_m is significant. We note that the projected 1D mode of Ω_m can be biased low by up to -0.8σ. Therefore, when reporting cosmology constraint, we do not focus on Ω_m.

In addition to OWLS-AGN, we also show the bias in projected 1D mode of S_8 with a few other extreme simulations (e.g., COWLS 8.5 and Eagle) as a function of small-scale cuts on $\xi_\pm$ in Fig. 9. As shown, the COWLS 8.5 simulation has a heating temperature for AGN feedback of $\log(\Theta_{\rm AGN}) = 8.5$, and the bias in S_8 is about 0.5σ but larger than OWLS-AGN for our fiducial scale cut. The bias may be caused by the extreme baryonic physics model of the COWLS 8.5 simulation.

V. FIDUCIAL CONSTRAINT AND INTERNAL CONSISTENCY

In this section, we present our cosmology constraints with the 2PCFs measured in Sec. III and the models introduced in Sec. IV. First we report our cosmology constraint with our fiducial setup in Sec. V A. In order to make sure that our fiducial analysis is robust, we conduct various internal consistency tests by analyzing different subsets of our catalog and with different analysis setups (e.g., different astrophysical and systematic models) in the context of the flat ΛCDM cosmology. First we look into the differences in our cosmology constraints, especially focusing on S_8, for analyses with different samplers (Sec. V E); flat priors on different cosmological parameters (Sec. V B); different astrophysical models (Sec. V C); and different systematic models (Sec. V D). Then we analyze data in different subfields, with different angular scale cuts, and removing each of the redshift bins to check the robustness of our results in Sec. V F. The results of our consistency tests are summarized in Figs. 12 and 17. In addition, we test the influence of B-mode errors in our cosmology constraint.

Note that, we specifically focus on the 1D projected modes of S_8 but not Ω_m in these tests since, as we saw in Sec. IV G, the constraint on Ω_m is sensitive to projection effects and modeling errors in Sec. V G.

Even though we report our constraints obtained from the `PolyChord` sampler in Sec. V A, we adopt `MultiNest` for most of the consistency tests in the rest of this section since `MultiNest` is much faster than `PolyChord`.

A. Fiducial constraint

Our fiducial cosmology constraint is conducted with the setup outlined at the start of Sec. IV G. First we report the constraints for the cosmological parameters, from our fiducial analysis, following the format defined in Eq. (33):

$$\begin{aligned}\Omega_{\rm m}:&\quad 0.256^{+0.056}_{-0.044}\quad(0.304),\\ \sigma_8:&\quad 0.818^{+0.089}_{-0.091}\quad(0.776),\\ S_8:&\quad 0.769^{+0.031}_{-0.034}\quad(0.782).\end{aligned}\tag{36}$$

The marginalized 2D posterior and the point estimates (including the projected mode and the MAP) of these cosmological parameters are shown in Fig. 10. We find the projected mode of $\Omega_{\rm m}$ (S_8) is less than the MAP by $\sim 0.9\sigma$ ($\sim 0.4\sigma$). It is consistent with what we found in Fig. 8 using noiseless mock 2PCFs that the projected modes are lower than the MAP. In addition to the cosmological parameters, the redshift shifting errors for the last two redshift bins estimated with a wide flat prior are

$$\begin{aligned}\Delta z_3:&\quad -0.115^{+0.052}_{-0.058}\quad(-0.120),\\ \Delta z_4:&\quad -0.192^{+0.088}_{-0.088}\quad(-0.190).\end{aligned}\tag{37}$$

In both Fourier [39] and real space cosmic shear analyses, we employ the ChainConsumer package [120] to analyze the MC chains and visualize the marginalized posteriors. After unblinding, we found that the outcomes from ChainConsumer differ mildly with those from GetDist [121]. This discrepancy arises because ChainConsumer lacks corrections for boundary effects and biases stemming from chain smoothing. Specifically, for ChainConsumer, boundary effects lead to inaccuracies in the 1D marginalized posterior near parameter boundaries predominantly influenced by top-hat priors. The high-level summary of the significance for our main reported results on S_8 is that the mode value does not change but the estimated uncertainty on S_8 is approximately 10% larger in ChainConsumer due to the kernel density estimation smoothing. Nonetheless, we retain in this paper the original parameters and plots, as unblinded, for transparency. We direct readers to Appendix A for an in-depth discussion of these effects.

We evaluate the goodness-of-fit with the value of χ^2 at MAP obtained from the fiducial MC chain returned by `PolyChord`, denoted as $\chi(\Theta_{\rm MAP})$. Since many of the parameters are prior-dominated (see figures in Appendix B), the calculation of the number of degrees of freedom is not straightforward. Therefore, we use noisy mocks of 2PCFs simulated according to the covariance matrix for the goodness-of-fit estimation. As the cosmological parameters were blinded when we did this test, we use the matter amplitude and matter density parameters from the WMAP9 cosmology but other parameters are from the MAP estimation of the first blinded catalog. We find, after unblinding, that our best-fit cosmology is very close to the WMAP9 cosmology. Noises with different realizations are added to the data vector according to the covariance (corrected by the Hartlap factor) of the blinded catalog estimated from mocks. We analyze these 50 mocks using our fiducial model and, to save computational time, we sample them with `MultiNest`. We obtain the reference χ^2 distribution from the histogram of the MAPs estimated from the 100 `MultiNest` chains as shown in Fig. 11. By comparing the χ^2 value of 150 obtained from the real data, to the reference χ^2 distribution, we find the p-value $p = 0.18$. In conclusion, our measured 2PCFs can be well described by the best-fit model. In addition, we fit a χ^2 distribution to the histogram and find that the best-fit effective degrees of freedom amount to 134. Given that the number of data

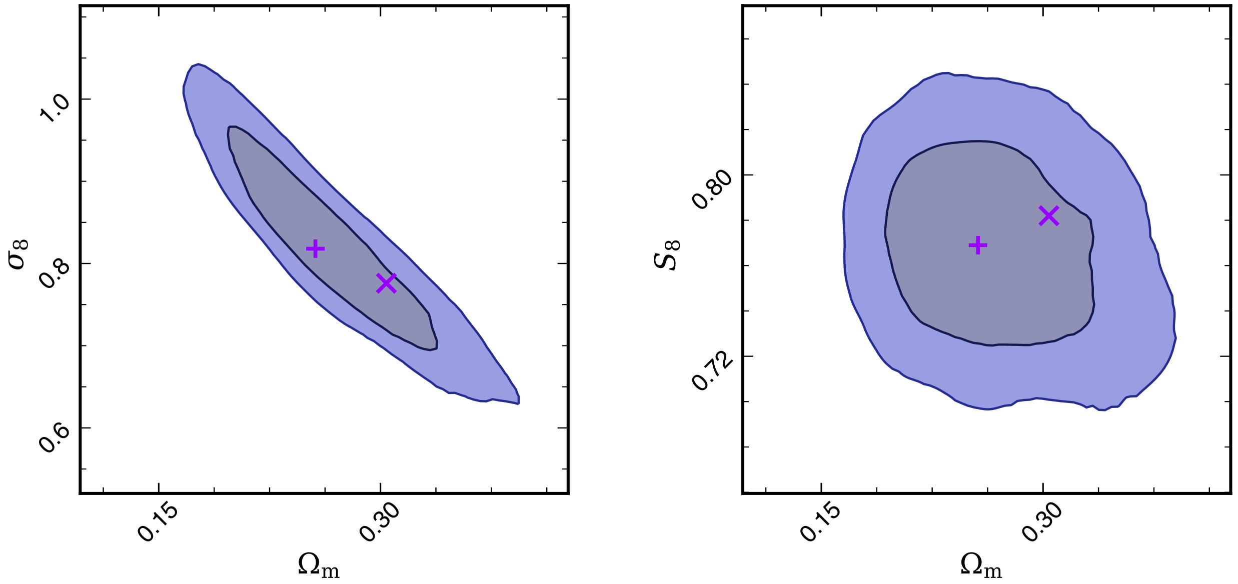

FIG. 10. Posterior contours (68% and 95% C.I. [For all the 2D posteriors shown in this paper, we plot the 68% and 95% C.I.]) of the 2D projected posterior in the ($\Omega_{\rm m}$, σ_8) plane (left panel) and ($\Omega_{\rm m}$, S_8) plane (right panel) for our fiducial analysis, where $S_8 = \sigma_8\sqrt{\Omega_{\rm m}/0.3}$. In addition, we show the projected 1D mode ("+") and the MAP estimated from `PolyChord` chains ("×").

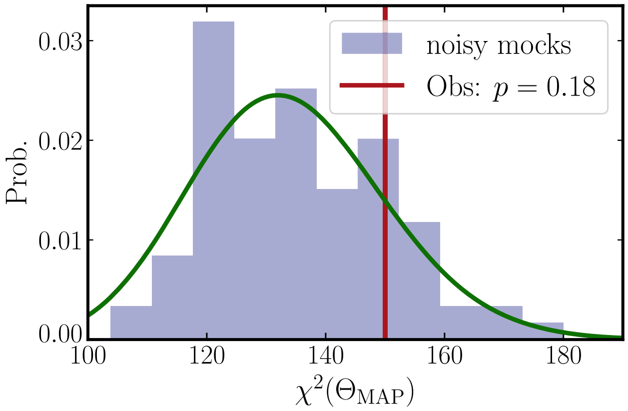

FIG. 11. The evaluation of goodness-of-fit with the χ^2 value at the maximum *a posteriori* (MAP) obtained from the chain of the fiducial analysis (red vertical line). The reference distribution (blue histogram) is obtained by analyzing the 100 noisy mock-data vectors. The p-value is 0.18. The green cure is the best-fit χ^2 distribution with effective degrees of freedom of 134.

points is 140, the effective number of free parameters is calculated to be $140 - 134 = 6$.

Due to an oversight in the code design, the MAPs of A_s and $\Omega_{\rm m}$ were accidentally not blinded when using them as inputs to generate the noisy mocks. However, we note that the estimated S_8, on which our analysis has the strongest constraining power, was blinded in the analysis process.

B. Priors

In our fiducial analysis, we apply a wide top-hat prior on the normalization parameter of the linear power spectrum; $A_s \in [0.5, 10] \times 10^{-9}$. Different cosmic shear analyses apply top-hat priors on different normalization parameters, including A_s (see [7]), $\ln(A_s)$, $\log(A_s)$ (see [5,44,122]) and S_8 (see [6]). Here, we compare the fiducial analysis with the following two priors:

(i) $\ln(A_s \times 10^{10}) \in [1.7, 5.0]$; and
(ii) $S_8 \in [0.1, 2.0]$.

After obtaining an MC chain from the nested sampling for the analyses with flat priors on A_s and $\ln(A_s)$, we reweight the chain in order to obtain a flat prior on the 2D plane of $(\Omega_{\rm m}, S_8)$ as discussed in Sec. IV A. Following Sugiyama *et al.* [8], the corrections for flat prior on A_s and $\ln(A_s)$ involve multiplying the weight of each sample by σ_8/A_s and σ_8, respectively. We refer the readers to Sugiyama *et al.* [8] for the derivation of the correction factors. We find, for a flat prior on A_s, the reweighting shifts the posterior to larger $\Omega_{\rm m}$.

In Appendix B 1, we show the marginalized 2D posteriors for different priors using both `MultiNest` and `PolyChord`. When using the `MultiNest` sampler, the uncertainties in $\Omega_{\rm m}$ for the analyses with the A_s $[\ln(A_s)]$ prior are smaller by 15% (10%) compared to the analysis with the S_8 prior; while the constraints on S_8 show little difference. This is consistent with the finding of Longley *et al.* [123]. In addition, for the analyses with `PolyChord`, the marginalized 2D posteriors for these three different priors are more consistent with each other than with to the analyses with `MultiNest`. It is likely that `MultiNest` neglects the tails of the 2D posteriors for A_s and $\log(A_s)$ priors, leading to underestimated uncertainties for these two analyses. We show the 1D summary statistics of the `PolyChord` posteriors between analyses with different priors in the second group of Fig. 12. As shown, our constraints on S_8 and $\Omega_{\rm m}$ are insensitive to the prior and the choices of sampling cosmological parameters.

C. Physical models

We now compare the cosmology constraints as we vary the model, especially focusing on S_8 between different physical models; the linear and nonlinear matter power spectrum, baryonic feedback (see Sec. IV A) and IA (see Sec. IV B). The 1D summary statistics for the comparisons are shown in Fig. 12, and the 2D contour plots are shown in Sec. B 2.

1. Power spectrum and baryonic feedback

In our fiducial analysis, we use the BACCO emulator [85] to model the linear matter power spectrum, and HMCode 2016 [84], implemented in `pyhmcode` [124], to model the nonlinear power spectrum and baryonic feedback. Here, we test the modeling uncertainties by comparing the constraints on cosmology parameters with other models for the matter power spectrum, including (i) changing the linear power spectrum modeling to CAMB [79] and (ii) changing the nonlinear modeling to HMCode 2020 [30] with a flat prior on the baryonic feedback parameter; $\Theta_{\rm AGN} \in [7.3, 8.3]$. In addition, we test the impact of not modeling baryonic feedback by (iii) continuing to use the BACCO emulator and HMCode 2016, but fixing the $A_{\rm b}$ parameter to 3.13.

The 1D summary statistics of the constraints are shown in the third group of Fig. 12, where the tests (i)–(iii) are labeled as “CAMB,” “Mead 2020” and “DM only,” respectively. In addition, the marginalized 2D posteriors are shown in Appendix B 2. We find that the shifts in cosmology parameters, i.e., $\Omega_{\rm m}$, σ_8 and S_8, are less than 0.5σ, and we conclude that the errors due to uncertainties in matter power spectrum modeling are not significant. This is consistent with our finding in Sec. IV G that our analysis is not sensitive to modeling errors in the matter power spectrum.

2. Intrinsic alignments

In our fiducial analysis, we use the TATT [37] to model the intrinsic alignment effect (see Sec. IV B). In order to test the robustness of our cosmological constraints to the IA modeling errors, we compare our fiducial analysis with the cosmology constraints obtained with two simpler models:

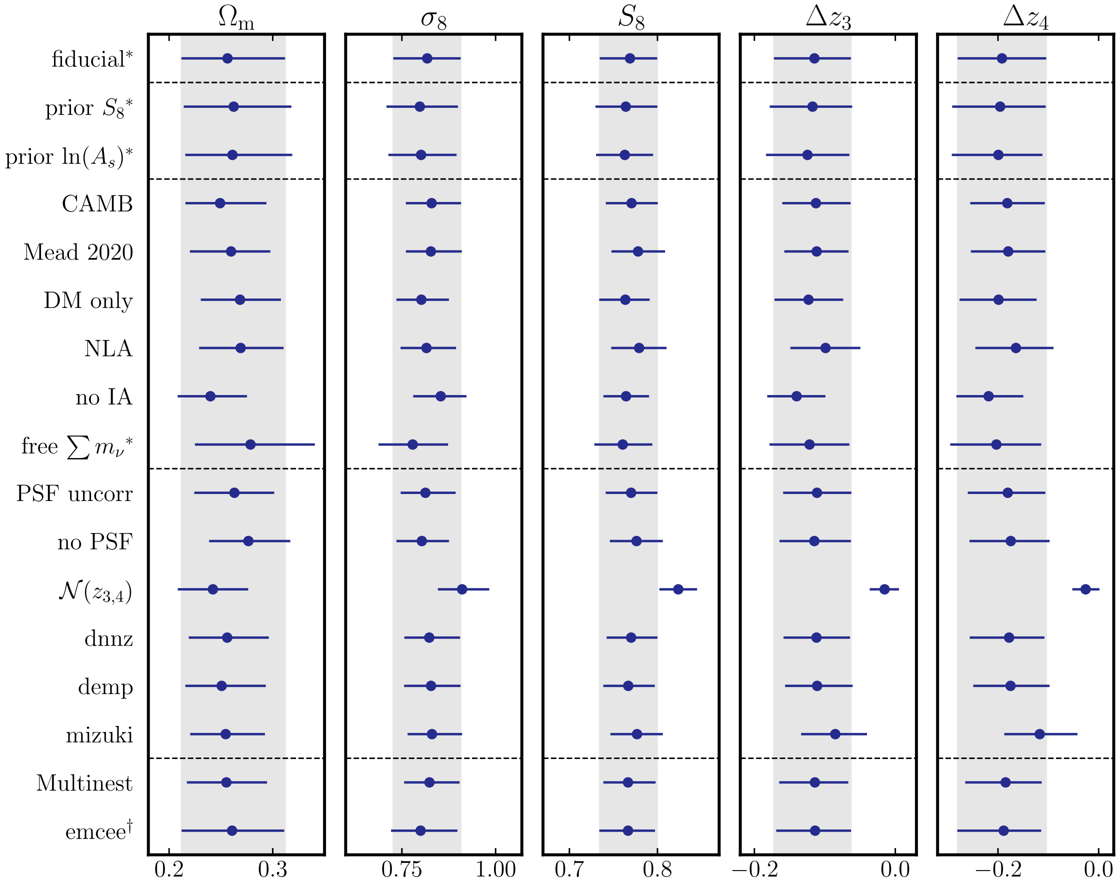

FIG. 12. The 68% C.I. of the 1D projected posterior on each of the parameters Ω_m, σ_8, S_8, Δz_3, and Δz_4 for different analysis setups. In total we have four groups divided by horizontal dashed lines: The first group is the fiducial setup; the second group is for different physical models; the third group is for different systematic models; the fourth group is for different samplers. The results with "*" ("†") are sampled with `PolyChord` (EMCEE) and the others are sampled with `MultiNest`.

(i) the NLA model [36], which is a subset of TATT (see Sec. IV B for a detailed description); and (ii) No intrinsic alignment model is used ("no IA") i.e., intrinsic alignments are assumed to be negligible. The other parts of our analysis pipeline are the same as the fiducial analysis. For the NLA model, we use the same priors for the IA parameters ($A_1 \in [-6, 6]$ and $\eta_1 \in [-6, 6]$) as summarized in Table II. The "no IA" configuration is a nonphysical case, which is used to test the difference in cosmology constraint under the extreme condition that IA effect is fully neglected.

The marginalized 2D posteriors are shown in Fig. 13, and the 1D summary statistics are shown in the third group of Fig. 12, where the tests (i)–(ii) are labeled as "NLA" and "no IA," respectively. We find no significant difference in our S_8 constraint when changing the IA model, although the constraints are stronger when using these simpler models. We find a smaller Ω_m and larger σ_8 for the constraint without modeling the IA effect. However, the shifts in these two parameters are less than 0.5σ; therefore, we conclude that Ω_m and σ_8 are not significantly influenced by the IA modeling error. In Fig. 13, we only show the leading order amplitudes (A_1) of the IA model for TATT. As shown, the A_1 parameter is detected with only 1.1σ and 2.1σ significance for TATT and NLA, respectively. We show the 95% confidence intervals of the IA signal in the 2PCFs using our fiducial model in Fig. 14. The contribution from IA to the 2PCFs is not significant. Therefore, we conclude that we do not find a significant detection of the IA signal. We note that the conclusion can be different for a higher-order IA model (e.g., Bakx *et al.* [125]). In addition to model-dependent analysis, numerous model-independent methods exist for detecting the IA signal in cosmic shear analysis [126–129]. We defer the validation of our conclusions using these methods on HSC data to future studies.

3. Massive neutrinos

Unlike the internal tests above, the test shown here on cosmology model with free neutrino mass is performed after unblinding. Massive neutrinos suppress the structure growth by smoothing the matter density field and changing the matter power spectrum at small scales; therefore, neutrino mass influences the constraint on cosmology parameters e.g., S_8. In our fiducial analysis, we fix the total neutrino

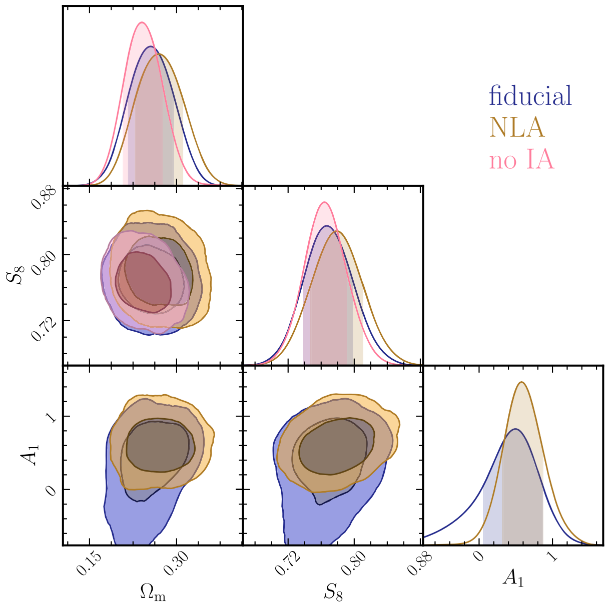

FIG. 13. The marginalized 2D posteriors of analyses with the TATT model (fiducial), the NLA model (NLA) and without modeling of IA (no IA).

mass—$\sum m_\nu = 0.06$ eV, which is the lower limit obtained by neutrino oscillation experiments [130,131]. We note that in the DES-Y3 analysis [7], they constrain neutrino mass with a flat prior. To make sure that our analysis is not sensitive to the difference in the prior on the sum of neutrino mass, we run an analysis with flat prior on the sum of neutrino mass, namely $\sum m_\nu \in [0.06\ \mathrm{eV}, 0.6\ \mathrm{eV}]$. The results are shown in Fig. 15.

The marginalized 2D posteriors are shown in Fig. 15, and the 1D summary statistics are shown as "free $\sum m_\nu$" in the third group of Fig. 17. We find very little change in our S_8 constraint when changing the prior on the neutrino mass. Our constraint on neutrino mass is weak and degenerate with $\Omega_{\rm m}$. This is because weak-lensing 2PCFs are only sensitive to the projected mass along the line of sight, and, due to the limited number of redshift bins, we lose the information on the redshift evolution of the large-scale structure. We note that the constraint on neutrino mass can be significantly improved by combining weak lensing, CMB and baryon acoustic oscillation (BAO) observations [132], but that is beyond the scope of this work.

D. Models of systematic effects

We compare the cosmology constraints, especially focusing on S_8, between different models for PSF systematics and systematics in modeling of redshift distributions.

1. PSF systematics

In our fiducial analysis, we adopt a PSF systematic model including PSF modeling error and PSF leakage from fourth-order PSF shapes. Additionally, we fully take into

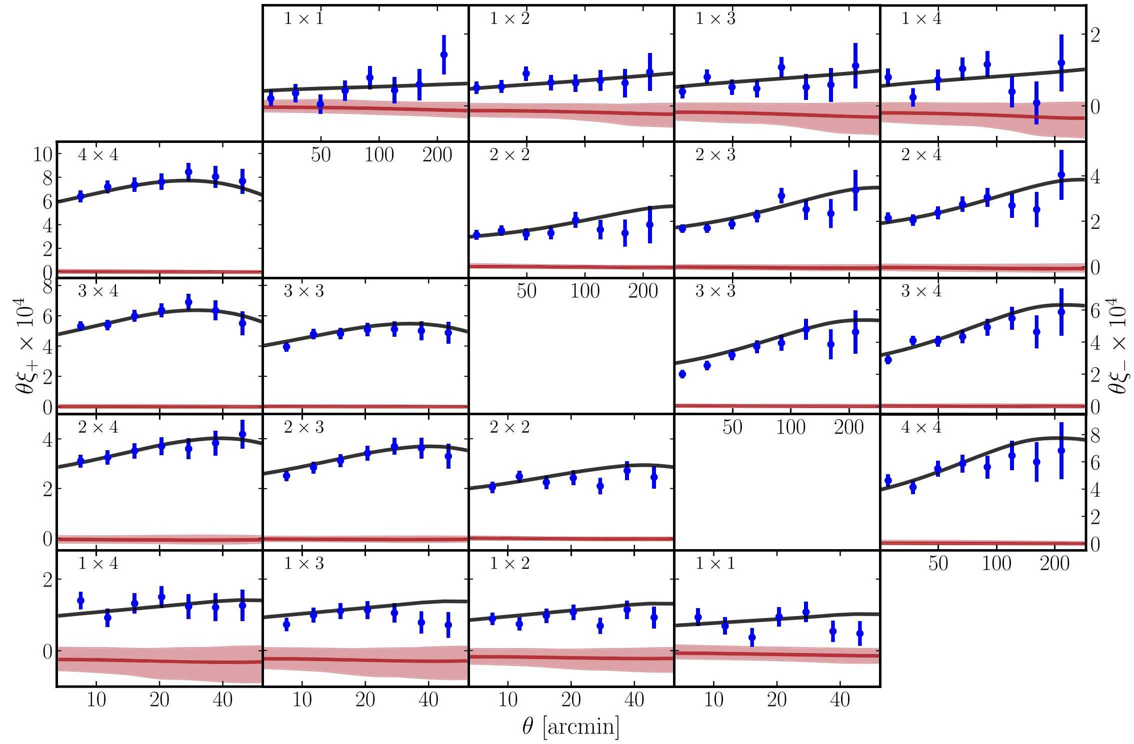

FIG. 14. The contribution from IA (including both the GG and GI terms), based on resampling from our fiducial posterior, to our 2PCFs. The IA signal is shown in red, where the solid lines are the mean, and the shaded reg regions are the 95% confidence intervals. The blue points are the measured 2PCFs and the black lines are the model prediction with the MAP, which are the same as in Fig. 3.

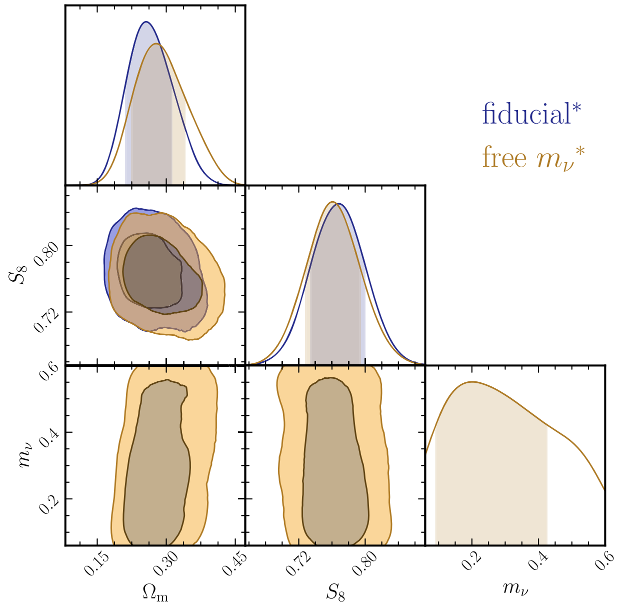

FIG. 15. The marginalized 2D posteriors of the flat ΛCDM cosmology with fixed neutrino mass (fiducial; $m_\nu = 0.06$) and free neutrino mass; $m_\nu \in [0.06, 0.6]$.

account the correlation between PSF systematic parameters. Here, we check the dependence of our cosmology constraint on the model choice of PSF systematics with the following two tests: (i) We determine the constraint without taking into account the correlation between the original PSF systematic parameters by sampling the correlated parameters with the uncorrelated prior; and (ii) we determine the constraint without modeling PSF systematics at all.

The marginalized 2D posteriors are shown in Appendix B 3, and the 1D summary statistics are shown in the fourth group of Fig. 12, where the tests (i)–(ii) are labeled as "psf uncorr" and "no PSF," respectively. We find that the "no PSF" analysis shows $\sim 0.15\sigma$ and $\sim 0.3\sigma$ increases from the baseline analysis in S_8 and $\Omega_{\rm m}$, respectively. We emphasize that the "no PSF" test is not realistic; we know that the PSF systematics are important for the analysis. The increase in $\Omega_{\rm m}$ is consistent with our finding in Zhang *et al.* [28] using noiseless mock 2PCFs, and the increase in S_8 is too small to be statistically significant. In addition, we do not find significant difference in cosmology constraints from the "psf uncorr" test. Therefore, we conclude that, within the choice of models we have considered, our cosmology constraint is not sensitive to the choice of PSF systematics model.

2. Photo-*z* systematics

Our fiducial analysis uses the redshift distribution of galaxies in four redshift bins obtained from a joint estimation using photo-z and cross-correlations between weak-lensing galaxies and CAMIRA-LRGs. The uncertainties on the redshift number densities were estimated based on comparison of different photo-z methods, and do not encompass the full range of systematic uncertainty. As described in Sec. IV C, there are potential biases on the redshift estimations in our third and fourth tomographic redshift bins, since the third bin is only partially calibrated, and the fourth bin is not calibrated by the CAMIRA-LRGs since the LRG sample extends only to $z = 1.2$. To be conservative, in our fiducial analysis, we adopt an uninformative, wide flat prior ranging from -1 to 1 for the mean redshift shifts in these two tomographic redshift bins.

Here, we compare the fiducial cosmology constraint with the one using the Gaussian prior recommended by Rau *et al.* [24] for Δz_3 and Δz_4. The result is labeled as "$\mathcal{N}(\Delta z_{3,4})$" in Fig. 12. As shown, we find a $\sim 2\sigma$ difference in S_8 between these two setups. Furthermore, the constraints on $\Delta z_{3,4}$ show shifts in the mean redshift estimation of the last two redshift bins. To assess the possibility that the shifts in $\Delta z_{3,4}$ are caused by statistical errors, we use 50 noisy mock 2PCFs generated using the WMAP9 cosmology and the best-fit fiducial model for nuisance parameters with Δz_3 and Δz_4 set to 0. We run the fiducial analysis on these mocks (Fig. 16) and find that it is not likely to obtain redshift shifts as large as our fiducial analysis—$\Delta z_3 = -0.115$ and $\Delta z_4 = -0.192$. Note that according to the definition in Eq. (22) *negative* values of $\Delta z_{3,4}$ indicate that the true mean redshift is *higher* than the mean redshift estimated by the joint calibration. Our results indicate that these shifts in the third and fourth redshift bin are statistically significant. We leave the study and calibration of these biases to our future work. Comparing "$\mathcal{N}(z_{3,4})$" with the fiducial constraints in Fig. 12, the conservative flat priors on $\Delta z_{3,4}$ are a large part of the reason why our constraints on S_8 are not improved

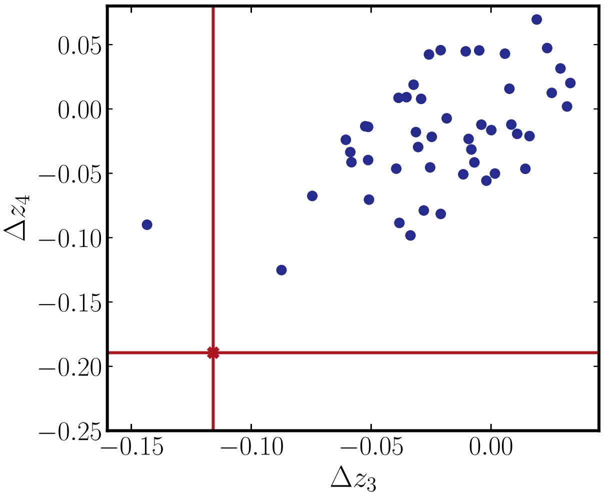

FIG. 16. The evaluation of statistical significance of the shifts in $\Delta z_{3,4}$. Blue points show the $\Delta z_{3,4}$ estimations by conducting our fiducial analysis on noisy mock 2PCFs. The red point is the estimation from our fiducial analysis on HSC-Y3 real data.

over the HSC-Y1 analyses [5], although the HSC-Y3 2PCF measurement has significantly higher SNR.

Additionally, we test the analysis by comparing the fiducial cosmology constraint with analyses using straight-up stackings of photometric posteriors (without deconvolution of photo-z error and calibration from LRGs as our redshift number density. In this test, we still use flat priors on $\Delta z_{3,4}$. As shown by "`dNNz`," "`DEmPz`," and "`mizuki`" in the fourth group of Fig. 12, we find that the difference in S_8 constraint is smaller than 0.5σ. Although directly using the stacked photo-z posterior is not mathematically correct [133], this test attempts to assess the possible bias from the error in the shape of $n(z)$s. However, we note that none of these $n(z)$s are well-calibrated at high redshift; therefore, this test is not able to capture potential bias for galaxies at $z > 1.2$.

E. Samplers

We adopt `PolyChord` as our fiducial sampler, and several internal consistent tests are conducted with `MultiNest` to save computational resources. Here, we check the consistency of the analysis between different samplers. Specifically, we compare the cosmology constraints between the three samplers summarized in Sec. IV F, namely `PolyChord`, `MultiNest`, and EMCEE. The 1D marginalized posteriors are shown in the fifth group of Fig. 12, and the 2D marginalized posteriors are shown in Appendix B 7. As shown, the confidence intervals on $\Omega_{\rm m}$ and σ_8 from `MultiNest` are ~15% smaller than `PolyChord` and EMCEE, while the confidence intervals from `PolyChord` and EMCEE are consistent; Lemos *et al.* [108] found similar results. In addition, we find the 1D projected modes from these three samplers are consistent. Therefore, we conclude that it is conservative to use `MultiNest` for our internal consistency tests as any inconsistency is more significant for results from `MultiNest` due to the smaller confidence intervals.

F. Subfields, tomographic bins, scales

1. Subfields

The HSC-Y3 survey footprint has six different subfields as summarized in Table I. Here, we assess the consistency in the cosmology constraints, especially focusing on S_8, by performing analyses on each subfield separately with our fiducial model.

The 1D summary statistics for the six subfields are shown in Fig. 17, which are labelled as "XMM," "GAMA09H," "GAMA09H," "WIDE12H," "VVDS," and "HECTOMAP," respectively. In addition, the marginalized 2D posteriors are shown in Appendix B 4.

We note that these fields have very different areas (see Table I for details); therefore, the 1σ errors are different among individual fields, and they are different from the fiducial analysis using all of the fields. Additionally, the constraints from these individual fields are approximately independent of each other since they are from different regions of sky; therefore, the errors are not significantly correlated. As shown in Fig. 17, XMM, GAMA15H, VVDS and HECTOMAP show $\sim 1\sigma$ differences in S_8 from the average. However, we note that each shift in S_8 is offset by less than 1σ given the uncertainty in the corresponding individual field. Taking into account that the errors are not significantly correlated, it is not likely for the scatters to be a flag of systematic errors.

2. Tomographic bins

Here, we exclude one tomographic redshift bin at a time and check whether the constraints are consistent with the fiducial constraint with all the four redshift bins. Our fiducial analysis adopts wide, flat priors on Δz_3 and Δz_4.

We find that when removing one of the first two redshift bin, the constraining power of the test is significantly degraded since we apply conservative flat priors on $\Delta z_{3,4}$ and use the measurements in the first two redshift bins to calibrate the redshift density estimations in the last two bins. Therefore, we adopt Gaussian priors on Δz_3 and Δz_4, taken from the posteriors of these parameters from the fiducial analysis, $\Delta z_3 = -0.115 \pm 0.055$ and $\Delta z_4 = -0.192 \pm 0.088$. This test is used to assess the robustness to our cosmology constraint across different redshift bins with the recalibrated redshift densities. When we remove each redshift bin in turn, we have no constraints on the corresponding Δz. In Fig. 17, we do not plot any Δz posterior when that bin is removed.

The 1D summary statistics are shown in Fig. 17, which are labeled as "no z_1," "no z_2," "no z_3," "no z_4," respectively. The marginalized 2D posteriors are shown in Appendix B 6. We find that the maximum shifts in S_8 constraints from removing each redshift bin are $\sim 0.5\sigma$ of the fiducial S_8 constraint. We note that these constraints with tomographic-bin removal are not independent. However, the differences in the S_8 constraints are less than 1.7%, which is small compared to the statistical error on our fiducial S_8 constraint.

While the "no z_3" case shows a significant shift in $\Omega_{\rm m}$, our analysis primarily emphasizes 1D constraints on S_8, rather than on $\Omega_{\rm m}$, similar to Dalal *et al.* [39]. This preference is due to the strong degeneracy between $\Omega_{\rm m}$ and σ_8. As depicted in Fig. 18, for both the "no z_3" and fiducial scenarios, there is a pronounced uncertainty ellipse in the $(\Omega_{\rm m}, \sigma_8)$ plane. Moreover, the 1D posteriors of $\Omega_{\rm m}$ do not follow a Gaussian distribution. In addition, we sample the "no z_3" case with both `MultiNest` and `PolyChord`. As shown in Fig. 18, the confidence interval on $\Omega_{\rm m}$ from `MultiNest` is significantly underestimated compared to `PolyChord` due to the assumptions in `MultiNest` [108]. The "no z_3" results shown in Fig. 17 are based on `MultiNest`.

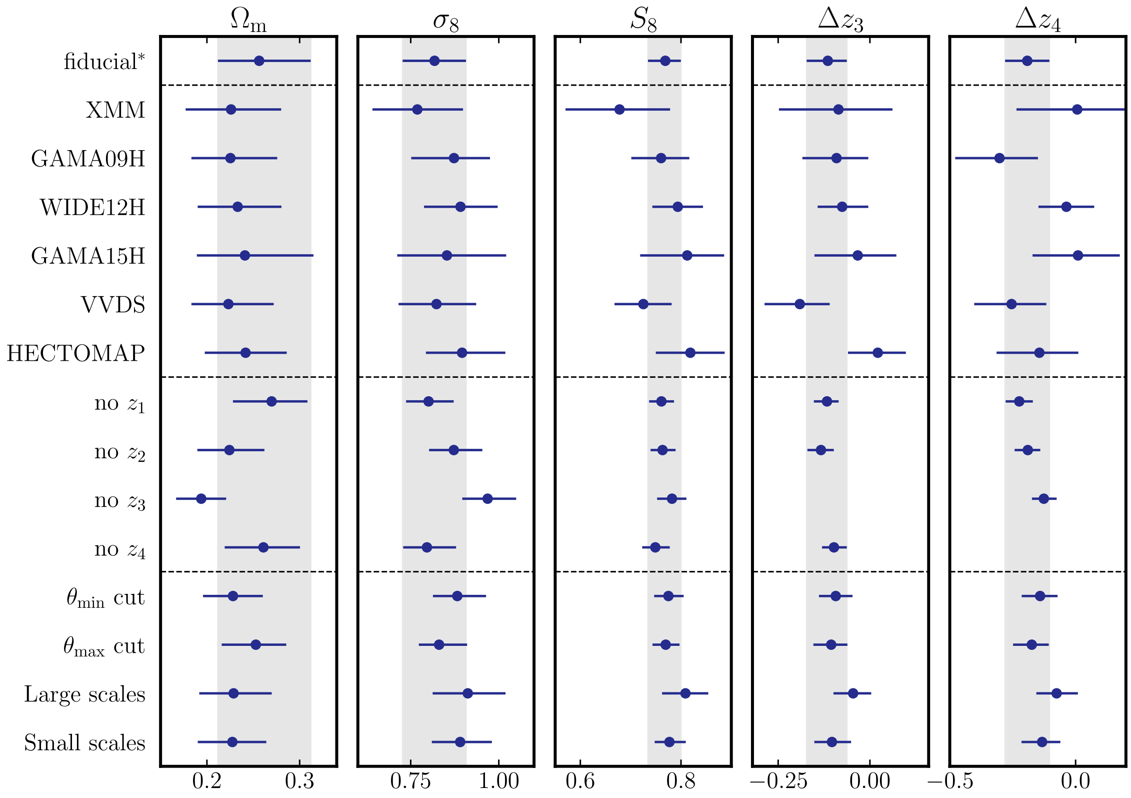

FIG. 17. The 68% C.I.s of 1D projected modes on the parameters Ω_m, σ_8, S_8, Δz_3 and Δz_4 for different splits of the HSC-Y3 data. We have four groups divided by horizontal dashed lines. The first group is the fiducial setup; the second group examines different subfields, the third group is for removal of different redshift bins, and the fourth group is for different scale cuts. The fiducial results (marked with "$*$") are sampled with `PolyChord` and the others are sampled with `MultiNest`. The Δz_3 and Δz_4 for "no z_3" and "no z_4" are missing, respectively, since the redshift bins are removed from the analysis.

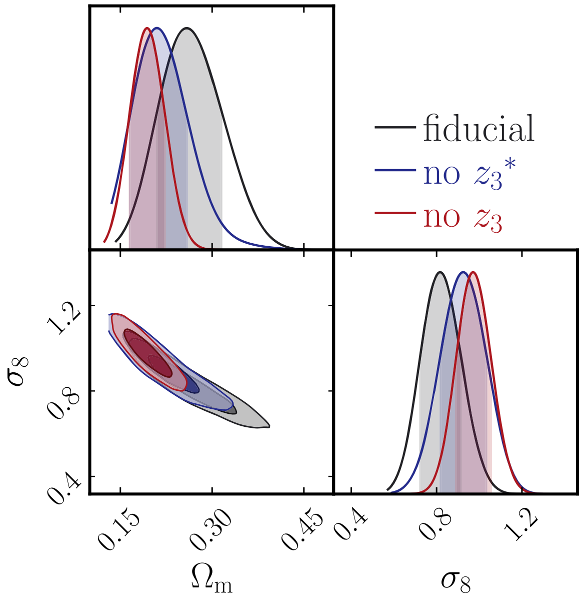

FIG. 18. The 2D posterior in the $(\Omega_\mathrm{m}, \sigma_8)$ plane for the fiducial analysis sampled with `PolyChord`, "no z_3" analysis sampled with both `PolyChord` (with *) and `MultiNest` (without *). The `MultiNest` sampler significantly underestimates the error on the parameters, particularly Ω_m.

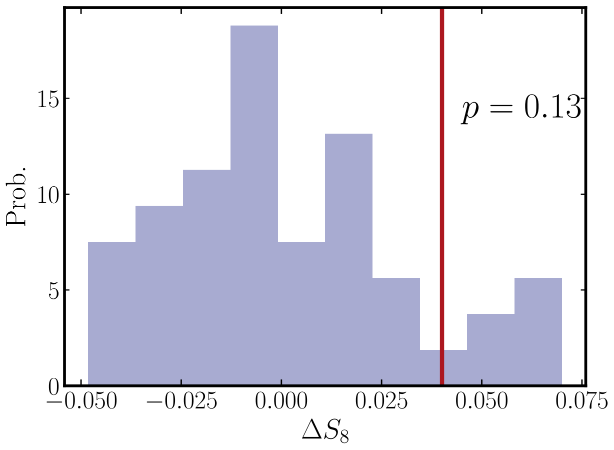

FIG. 19. The evaluation of the statistical significance of the shift in S_8 for the test with large scale cut using 50 mock 2PCFs. The reference distribution (blue histogram) is obtained by analyzing the noisy mocks with the fiducial scale cut, and keeping large scales only. The red vertical line is the estimation of ΔS_8 from real data. The probability of finding ΔS_8 larger than the real analysis is 13%.

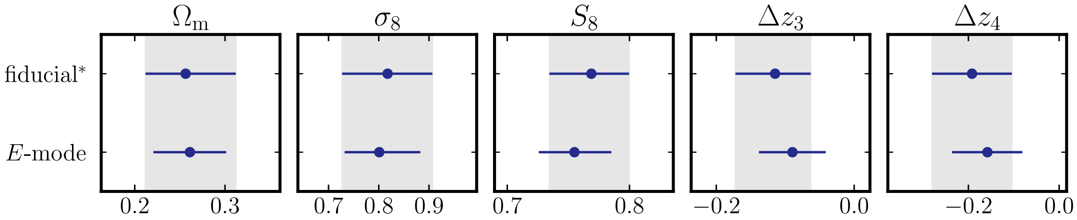

FIG. 20. Similar to Figs. 12 and 17. The 68% C.I. of the 1D projected posterior on each of the parameters Ω_m, σ_8, S_8, Δz_3 and Δz_4 for the fiducial constraint (first row) and the constraint with E-mode-only 2PCFs (second row) after removing the B-mode signal in Fig. 5.

When we compare the data vector for the "no z_3" case against model predictions based on our fiducial MAP constraint, the chi-squared value is 72.1. In contrast, the chi-squared value is 69.8 for the "no z_3" MAP. Given that the effective degrees of freedom are around 79, both sets of parameters fit the data well. Therefore, even though the "no z_3" scenario indicates a noticeable deviation in Ω_m compared to the fiducial constraint, the data *does not strongly* favor either scenario over the other.

3. Scale cuts

Our fiducial scale cuts are $7.1 < \theta/\mathrm{arcmin} < 56.6$ for ξ_+ and $31.2 < \theta/\mathrm{arcmin} < 248$ for ξ_-. Here, we change the angular scale cuts and check the consistency of the cosmology constraints, especially focusing on constraint on S_8. The scale cuts we test include:

(i) **$\boldsymbol{\theta}_\mathrm{max}$ cut:** $\theta_+ \in [7.1, 75.9]$ and $\theta_- \in [31.3, 247.8]$,
(ii) **$\boldsymbol{\theta}_\mathrm{min}$ cut:** $\theta_+ \in [5.3, 56.5]$ and $\theta_- \in [23.3, 247.8]$,
(iii) **Large scales only:** $\theta_+ \in [17.3, 56.5]$ and $\theta_- \in [75.9, 247.8]$, and
(iv) **Small scales only:** $\theta_+ \in [7.1, 23.3]$ and $\theta_- \in [31.3, 102.1]$,

where all numbers are in units of arcminutes. The 1D summary statistics of the tests are shown in Fig. 17, which are labeled as "θ_max cut," "θ_min cut," "Large scales," "Small scales," respectively. The marginalized 2D posteriors are shown in Appendix B 5. We find a $\sim 1\sigma$ difference in S_8 for the analysis using large scale data only. In order to quantify the statistical significance of this difference, we perform our fiducial analysis on 50 noisy mock 2PCFs using the fiducial scale cut and the large scales only. To be more specific, the noisy mocks are generated with the WMAP9 cosmology but the best-fit nuisance parameters from the fiducial analysis. We record the difference in S_8 estimation for each noisy mock realization, and the probability distribution of the difference in S_8, denoted as ΔS_8 is shown in Fig. 19. As shown, there is a 13% probability of ΔS_8 being larger than the real analysis; therefore, this difference is not statistically sufficient to be a bias. We find that the differences in S_8 constraints are negligible for the other tests on scale cuts. The shifting error is less significant at large scales, and this is also the case for the pseudo-C_ℓ analysis in Dalal *et al.* [39].

G. *B*-mode errors

To assess the robustness of our cosmology constraint, we test the influence of B-mode residuals shown in Fig. 5 to our constraint. Specifically, we subtract the estimated B-mode residuals in Fig. 5 from our 2PCFs and analysis the data vector with our fiducial setup. This test is performed after the unblinding. To save the computational time, we do not reestimate the covariance of the derived E-mode 2PCFs, and we use the fiducial covariance matrix. The fiducial constraint and the constraint with E-mode 2PCFs is shown in Fig. 20. As shown, the difference between the two constraints on S_8 is less than 0.5σ, which indicates that the B-mode residuals shown in Fig. 5 are not likely to cause significant error on our cosmology constraint.

VI. COSMOLOGICAL CONSTRAINTS AND EXTERNAL ANALYSIS

After having verified that the HSC-only constraints are robust, we check the consistency of our constraints with other observations and quantify any tension. The external observations include weak-lensing surveys such as DES [7,38] and KiDS [6] (see Sec. VI A), the Planck-2018 CMB analysis [4] (see Sec. VI B), and the eBOSS BAO analysis (see Sec. VI C). We summarize the external observations as follows:

(i) **DES-Y3:** The DES-Y3 weak-lensing data contains about 100 million galaxies (with $n_\mathrm{eff} \sim 5.6\ \mathrm{arcmin}^{-2}$) over more than 4,000 square degress [134]. We focus on the posterior from the cosmic shear 2PCFs presented in [7,64].
(ii) **KiDS-1000:** The KiDS-1000 weak-lensing data contains 21 million galaxies (with $n_\mathrm{eff} \sim 6.2\ \mathrm{arcmin}^{-2}$) over 1000 square degrees [135]. Their cosmic shear paper [6] present cosmic shear analyses using three different statistics (i.e., COSEBIs, 2PCFs, and pseudo-C_ℓ). We use the analysis with COSEBIs, which is the fiducial result from KiDS, in this paper.
(iii) **Planck-2018:** This is the final data release from the *Planck* cosmic microwave background experiment [4]. We incorporate the primary TT data on scales $30 < \ell < 2508$, and also the joint temperature and polarization measurements (TT, TE, EE and BB) at scales $2 < \ell < 30$.

(iv) **eBOSS DR16:** We include spectroscopic baryon acoustic oscillation measurements from the eBOSS galaxy sample. We recompute the posterior in our choice of cosmological parameter space (summarized in Table II), and we combine it with our cosmic shear 2PCFs constraints assuming that these two measurements are independent.

A. Other weak-lensing analyses

We first compare our fiducial constraints on Ω_m and S_8 with other ongoing weak-lensing surveys (i.e., KiDS and DES). As shown in Fig. 21, our result is consistent in general with the DES-Y3 and KiDS-1000 results. Specifically, the difference in the 2D plane of Ω_m and S_8 is within the confidence region, even though the contour size of HSC-Y3 is larger than DES-Y3 and KiDS-1000. We note that the larger contour size is partly due to the use of a flat prior on the photo-z shifting error parameters on the last two redshfit bins (i.e., Δz_3 and Δz_4). If we employ the Gaussian informative prior with $\sigma(\Delta z_{3,4}) \sim \mathcal{O}(10^{-2})$ as derived in [24] on these redshift error parameters, our constraint becomes 15% tighter; however, as shown in Sec. V D, the posterior shows a non-negligible shift toward the direction of larger S_8.

B. *Planck* CMB analysis

We next compare our fiducial constraint with *Planck*-2018. As shown in Fig. 21, our constraint on S_8 appears to be in tension with *Planck*-2018. To quantify the tension, we perform importance sampling to generate chains of equal length from our fiducial and the *Planck*-2018 chains. We then assume that the cosmological constraints are independent and create a new probability distribution with the

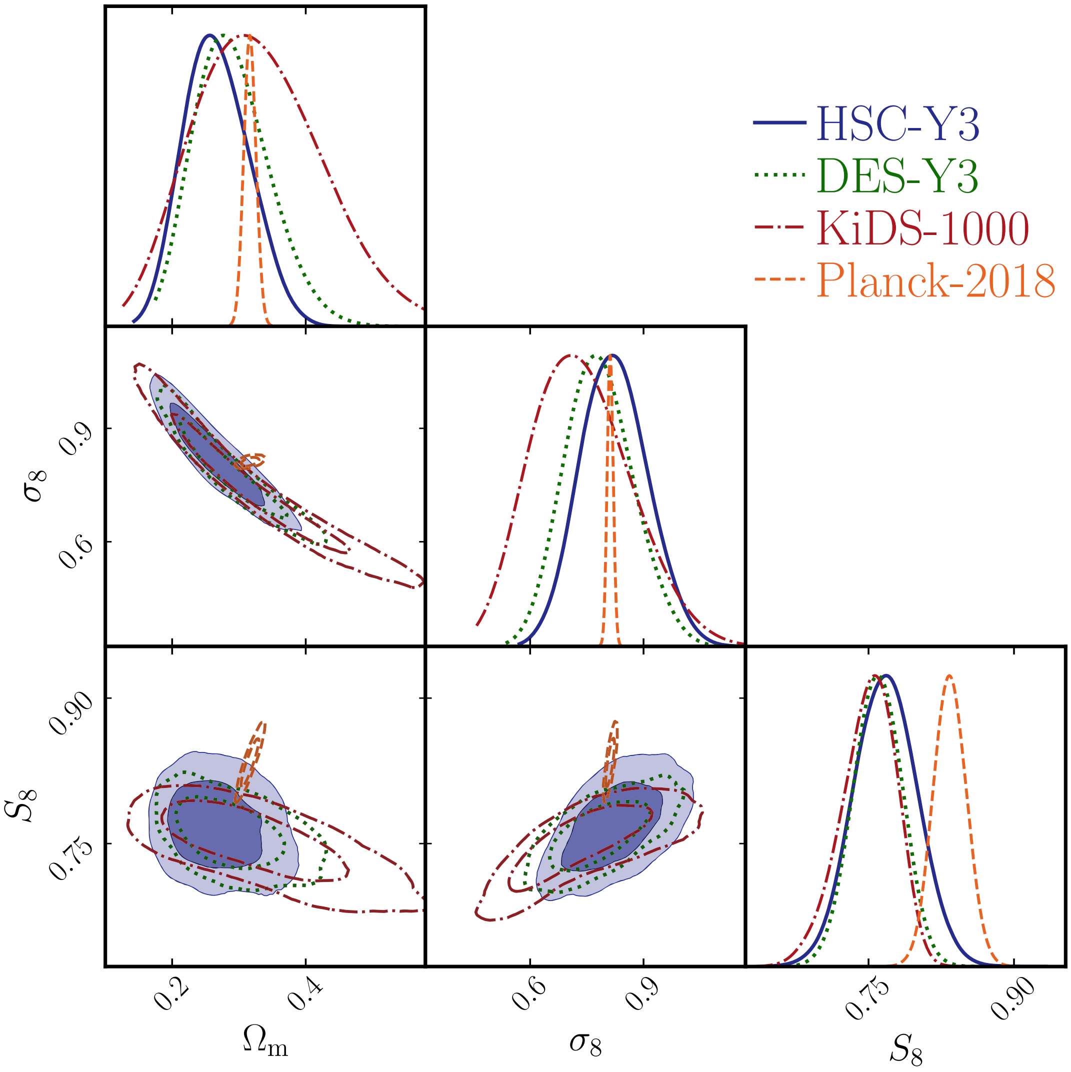

FIG. 21. Comparison between our fiducial cosmology constraint and contemporary weak-lensing observations (i.e., KiDS-1000 and DES-Y3) and *Planck*-2018 CMB observation. The posterior data are plotted as published by each collaboration. These analyses have slightly different priors and astrophysical and systematic models.

difference in S_8 between these two chains—$\Delta S_8 = S_8(\mathrm{HSC}) - S_8(Planck)$ following Charnock *et al.* [136]. The probability of our fiducial analysis being in tension with *Planck*-2018 is defined as the posterior probability enclosed within the contour intersecting the point $\Delta S_8 = 0$. We find a 95.3% chance of being in tension with *Planck*-2018, corresponding to a 1.98σ tension.

In addition, we quantify the possible tension between our constraint and the *Planck*-2018 using the `eigentension` method developed in Park and Rozo [137] with the assumption that these two constraints are independent. We first diagonalize the posterior covariance matrix in the space spanned by the cosmological parameters to find the eigenvectors and the corresponding eigenvalues. Since n_s, ω_b and h_0 in our analysis are prior dominated, we focus on the two parameters that are well-constrained and not prior-dominated: Ω_m, and σ_8. After diagonalizing the covariance matrix of these parameters, we find the two eigenvectors, defined as $e_1 = \sigma_8(\Omega_m)^{0.56}$ and $e_2 = \Omega_m(\sigma_8)^{-0.56}$. We compute the posterior distribution of the difference in the eigenvector, which is defined as

$$(\Delta e_1, \Delta e_2) \equiv (e_1, e_2)_\mathrm{HSC} - (e_1, e_2)_\mathrm{planck}. \tag{38}$$

By estimating the posterior probability above the contour intersecting the point $(\Delta e_1, \Delta e_2) = (0, 0)$, we find our constraint has a 94.5% chance of being in tension with *Planck*-2018, which corresponds to a 1.92σ tension.

C. eBOSS BAO analysis

Finally, we compare our fiducial constraint with the extended Baryon Oscillation Spectroscopic Survey (eBOSS) DR16 analysis [138]. The eBOSS analysis uses galaxies as direct tracers of the density field to measure baryon acoustic oscillation up to $z \sim 3$. We reanalyze the BAO measurements with the prior summarized in Table II using different types of galaxies, including SDSS main galaxy sample (MCGs; [139]), BOSS DR12 galaxies [140], eBOSS galaxies [including luminous red galaxies (LRGs) [141], emission line galaxies (ELGs) [142], quasars [143] and Lyman-α forest samples [144]]. The analysis adopts the likelihood implemented in CosmoSIS. The projected 2D posteriors for the BAO analysis is shown in Fig. 22.

Then we quantify the tension between our fiducial constraint and the BAO constraint on both S_8 and (e_1, e_2). We do not find significant tension between these two analyses—0.23σ and 0.19σ tensions for S_8 and (e_1, e_2), respectively. Since these two constraints are independent and do not show strong tension, we perform a joint analysis between the cosmic shear 2PCFs and the BAO measurements assuming that the two observations are independent. The joint HSC-eBOSS analysis is shown in Fig. 22. We find our constraint on S_8 does not change since BAO does not constrain S_8; however, the constraint on Ω_m significantly improves.

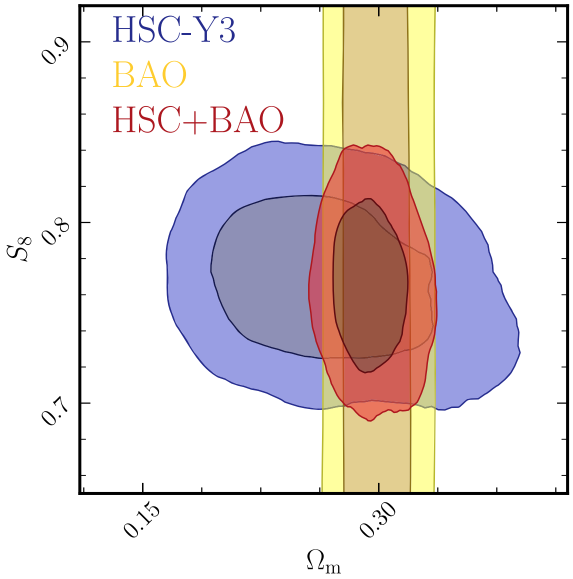

FIG. 22. Comparison between our fiducial constraint (blue contours) and the constraint on cosmology from the eBOSS BAO measurement (yellow contours), which is analyzed with the same priors in Table II. The red contours are the joint estimation between the two observations.

VII. SUMMARY AND OUTLOOK

This paper presents the cosmological constraints from cosmic shear 2PCFs with over ∼1 million galaxies from the three-year Hyper Suprime-Cam (HSC-Y3) data, which covers 416 deg^2 up to redshift $z \sim 2$.

By using our fiducial model to analyze different synthetic 2PCFs, we find the modeling uncertainties on S_8 are less than 0.5σ even for the simulations with the most extreme baryonic feedback models. We model the cosmic shear 2PCFs in the flat ΛCDM cosmology with the sum of neutrino mass fixed to 0.06 eV, and constrain the lensing amplitude with 3.5% precision, finding $S_8 = \sigma_8\sqrt{\Omega_\mathrm{m}/0.3} = 0.769^{+0.031}_{-0.034}$ (68% C.I.). Additionally, the matter density is constrained with 5% precision; $\Omega_\mathrm{m} = 0.256^{+0.056}_{-0.044}$ (68% C.I.). Systematic tests on synthetic data vectors show that the modeling errors on S_8 do not exceed 0.5σ, whereas the maximum modeling error on Ω_m is about 1σ arising from projection of high-dimensional posterior onto 1D space and the modeling uncertainties in baryonic feedback. To assess the robustness of our constraint, we conduct a number of blinded internal consistency tests by analyzing different subsets of the data with different systematic and astrophysical models under the context of the flat ΛCDM cosmology. After unblinding, we compare our constraints on S_8 with other HSC-Y3 weak-lensing analyses e.g., [39,41,42] and find extremely good agreement between these analyses.

Furthermore, we compare our analysis with external dataset and find that our results qualitatively agree well with weak-lensing analyses from the ongoing surveys;

KiDS-1000 [6], DES-Y3 [64]. However, these weak-lensing constraints on S_8 is $\sim 2\sigma$ lower than the constraint from *Planck*-2018 [4].

For the final-year HSC dataset covering $\sim 1, 100\ \mathrm{deg}^2$ on the Northern sky, we expect the precision on S_8 measurement will be improved to ≤ 0.025 thanks to the increase in survey area. We will then be able to see whether the S_8 tension remains. For the final-year analysis, controlling the systematic errors will be more challenging. Below, we discuss a few places that require improvements for the final year weak-lensing analyses.

A. Modelng of baryonic feedback

Our fiducial analysis models the baryonic feedback at small scales using HMCode 2016, and find a significant positive detection of baryonic feedback; $A_\mathrm{b} = 2.34^{+0.40}_{-0.25}$, which is consistent with the HSC-Y3 Fourier space cosmic shear analysis ($2.43^{+0.46}_{-0.25}$) [39]. We note that DES-Y3 adopts HaloFit, a dark matter only empirical model, to calculate the power spectrum since DES-Y3 goes to larger angular scales than HSC-Y3, and they adopt a conservative small-scale cut; therefore, they are less sensitive to baryonic feedback on small scales. In addition, we conduct an analysis with HMCode 2020, which models baryonic feedback with Θ_AGN, and we find the difference in the S_8 constraint is less than 0.5σ. Furthermore, we conduct a number of tests using synthetic 2PCFs to confirm that, for our fiducial scale cut, our constraint on S_8 is robust to modeling error in baryonic feedback. Given this positive detection of baryonic feedback, future cosmology analyses, especially ones aiming to use smaller scale data, will have to be careful in understanding the modeling errors in baryonic feedback.

B. *B*-modes at large scales

We find significant B-modes in ξ_+ at scales $\theta > 60$ arcmin, especially in the last two tomographic bins. To mitigate the B-mode leakage into our cosmology analysis, we apply conservative scale cuts to remove angular scales with $\theta > 56$ arcmin in ξ_+. Similarly, Dalal *et al.* [39] find significant B-modes at scales $\ell < 300$. Note that the DES-Y3 2PCF analysis has a large-scale ct greater than 200 arcmin. Since the DES-Y3 2PCF measurement is dominated by data at very large scales, the modeling uncertainty from baryonic feedback, which is significant at small scales, has a smaller influence on their analysis than in our own. Therefore, controlling the B-modes in large angular scales and including large-scale data in our analysis would not only improve the accuracy but also reduce the modeling uncertainty from baryonic feedback. In future analyses, we will further study the B-modes at large scales and understand the cause of them.

C. Redshift estimation errors

Our fiducial analysis uses a conservative, wide, flat prior on the shifts in the third and fourth redshift bins, and our results indicates significant redshift error on these bins—$\Delta z_3 = -0.115^{0.052}_{-0.058}$ and $\Delta z_4 = -0.192^{0.088}_{-0.088}$—which do not agree with the Gaussian priors on $\Delta z_{3,4}$ derived in Rau *et al.* [24]. In addition, when applying the Gaussian priors of Rau *et al.* [24] on the last two tomographic bins, we find that S_8 shifts to higher values by $\sim 1.7\sigma$ compared to the fiducial analysis adopting flat priors. All of the HSC-Y3 cosmology analyses [39,41,42] find evidence for biased redshifts in these bins. Furthermore, it should be noted that the study conducted by Leauthaud *et al.* [145] found a correlation between the measured excess surface density and the mean source redshift of the lensing survey, potentially resulting from redshift estimation systematics. This was observed through a comparative analysis of the excess surface density measurements of SDSS BOSS lens galaxies [140] using background galaxies from several surveys including CFHTLenS [146], CFHT Survey of Stripe 82 [147], DES [148], KiDS [149], and HSC [150]. Notably, our findings on the redshift measurement errors are consistent with the trend reported in Leauthaud *et al.* [145].

We have taken the most conservative possible approach to these photo-z errors. Due to the flat prior, the constraining power on S_8 of our HSC-Y3 analysis is similar to that of the HSC-Y1 analyses, although the sky coverage is three times larger than the HSC-Y1 dataset. We will work on improving the calibration of the source redshift distribution in the highest two tomographic bins and try to improve the constraining power on S_8.

D. Future improvements

Our final-year HSC data release will cover $\sim 1, 100\ \mathrm{deg}^2$ of the Northern sky with the same depth and image resolution. The data reduction will also be performed by an updated version of LSST Science Pipelines [47], with notable improvements being a multiband deblender [151], consistent selection of PSF stars and with a state-of-the-art PSF modeling [152]. Due to the increase in the data volume alone, the uncertainty on S_8 is expected to be reduced to about 2.5%, and we will be able to see whether the significance of the tension between HSC 2PCFs cosmic shear analysis and Planck increases. We will attempt to improve the control of systematic errors for the final-year analyses with the following approach:

(i) Include multiband images in our galaxy image simulations with realistic galaxy color information [153] (for example, see [153]) to enable us to test photometric redshift estimation and calibrate the $n(z)$ estimation bias from redshift-dependent shear [154,155].

(ii) Update the shear estimation code to a state-of-art algorithm [156–158] which uses correct for multiplicative bias from detection and selection below

0.5% without relying on empirical calibration from external image simulation.

(iii) Cross-check the high redshift $n(z)$ estimates with other galaxy samples with spectroscopic redshift estimations (e.g., DESI [159]) or with other measurments (e.g., shear ratio test [160] and CMB lensing [161]).

The HSC survey is a pioneer survey for future Stage-IV imaging surveys which have much larger sky coverage, higher resolution and/or deeper imaging. These Stage-IV surveys include a ground-based survey: the Vera C. Rubin Observatory Legacy Survey of Space and Time (LSST; [162]), and space-based surveys: Euclid [163] and the Nancy Grace Roman Space Telescope (Roman [164]). These datasets will allow us to better constrain S_8 and understand the apparent tension between the *Planck*-2018 CMB observation.

ACKNOWLEDGMENTS

X. L., T. Z., and R. M. are supported in part by the Department of Energy Grant No. DE-SC0010118 and in part by a grant from the Simons Foundation (Simons Investigator in Astrophysics, Award ID No. 620789). R. D. acknowledges support from the NSF Graduate Research Fellowship Program under Grant No. DGE-2039656. Any opinions, findings, and conclusions or recommendations expressed in this material are those of the authors and do not necessarily reflect the views of the National Science Foundation. We thank the anonymous reviewers for their careful reading of our manuscript and their many insightful comments and suggestions. This work was supported in part by World Premier International Research Center Initiative (WPI Initiative), MEXT, Japan, and JSPS KAKENHI Grants No. JP18H04350, No. JP18H04358, No. JP19H00677, No. JP19K14767, No. JP20H00181, No. JP20H01932, No. JP20H04723, No. JP20H05850, No. JP20H05855, No. JP20H05856, No. JP20H05861, No. JP21J00011, No. JP21H05456, No. JP21J10314, No. JP21H01081, No. JP21H05456, No. JP22H00130, No. JP22K03634, No. JP22K03655 and No. JP22K21349 by Japan Science and Technology Agency (JST) CREST JPMHCR1414, by JST AIP Acceleration Research Grant No. JP20317829, Japan, and by Basic Research Grant (Super AI) of Institute for AI and Beyond of the University of Tokyo. S. S. was supported in part by International Graduate Program for Excellence in Earth-Space Science (IGPEES), WINGS Program, the University of Tokyo. This work was supported by JSPS Core-to-Core Program (Grant No. JPJSCCA20210003). The Hyper Suprime-Cam (HSC) Collaboration includes the astronomical communities of Japan and Taiwan, and Princeton University. The HSC instrumentation and software were developed by the National Astronomical Observatory of Japan (NAOJ), the Kavli Institute for the Physics and Mathematics of the Universe (Kavli IPMU), the University of Tokyo, the High Energy Accelerator Research Organization (KEK), the Academia Sinica Institute for Astronomy and Astrophysics in Taiwan (ASIAA), and Princeton University. Funding was contributed by the FIRST program from the Japanese Cabinet Office, the Ministry of Education, Culture, Sports, Science and Technology (MEXT), the Japan Society for the Promotion of Science (JSPS), Japan Science and Technology Agency (JST), the Toray Science Foundation, NAOJ, Kavli IPMU, KEK, ASIAA, and Princeton University. This paper is based on data collected at the Subaru Telescope and retrieved from the HSC data archive system, which is operated by the Subaru Telescope and Astronomy Data Center (ADC) at NAOJ. Data analysis was in part carried out with the cooperation of Center for Computational Astrophysics (CfCA), NAOJ. We are honored and grateful for the opportunity of observing the Universe from Maunakea, which has the cultural, historical and natural significance in Hawaii. The Pan-STARRS1 Surveys (PS1) and the PS1 public science archive have been made possible through contributions by the Institute for Astronomy, the University of Hawaii, the Pan-STARRS Project Office, the Max Planck Society and its participating institutes, the Max Planck Institute for Astronomy, Heidelberg, and the Max Planck Institute for Extraterrestrial Physics, Garching, The Johns Hopkins University, Durham University, the University of Edinburgh, the Queen's University Belfast, the Harvard-Smithsonian Center for Astrophysics, the Las Cumbres Observatory Global Telescope Network Incorporated, the National Central University of Taiwan, the Space Telescope Science Institute, the National Aeronautics and Space Administration under Grant No. NNX08AR22G issued through the Planetary Science Division of the NASA Science Mission Directorate, the National Science Foundation Grant No. AST-1238877, the University of Maryland, Eotvos Lorand University (ELTE), the Los Alamos National Laboratory, and the Gordon and Betty Moore Foundation.

APPENDIX A: BIASES IN ChainConsumer

In this appendix, we show the biases caused by the boundary effect and the smoothing of MC samples when analyzing the 1D marginalized posteriors using ChainConsumer. Boundary bias arises near the boundaries of the projected 1D sample. A traditional KDE assumes that the sample extends infinitely, which is not true for real-world data. As a result, density estimates close to the edges may be biased downwards since the kernel function extends beyond the data range, effectively under-representing the true density. Reference [121] uses first-order boundary correction and a multiplicative bias correction for higher-order bias caused by the KDE smoothing.

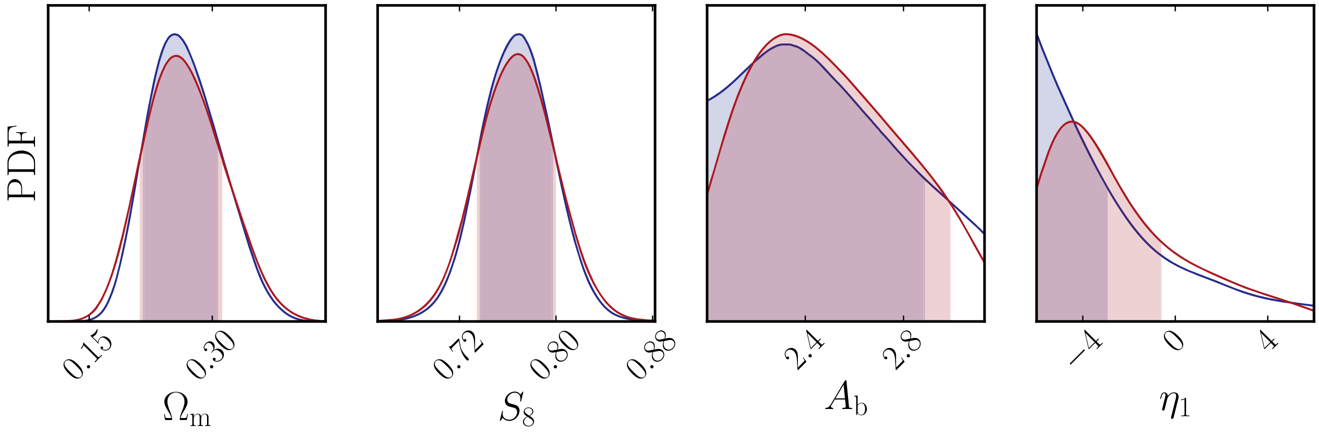

FIG. 23. This figure shows the normalized 1D marginalized posterior of our fiducial constraints on four parameters. The red lines are before the corrections for the boundary effect and multiplicative bias due to the smoothing in ChainConsumer, and the blue lines are after the bias corrections. This illustrates how the posteriors for prior-dominated nuisance parameters are noticeably modified at the boundaries, whereas those for the cosmological parameters simply change by ∼10% in width while remaining centered at the same parameter values.

Figure 23 presents the marginalized 1D posteriors from the fiducial analysis, both before and after bias corrections. It reveals that for parameters inadequately constrained by cosmic shear data, the boundary posteriors are underestimated due to the boundary effect. Furthermore, for parameters less affected by the top-hat priors, the errors are overestimated owing to the multiplicative bias introduced by KDE smoothing.

APPENDIX B: 2D POSTERIORS FOR INTERNAL TESTS

In this appendix, we show the 1D and 2D marginalized posteriors of our fiducial constant and the constraints of our internal consistent tests. First, in Fig. 24, we show the corner plot for marginalized 2D posteriors of cosmological parameters and astronomical parameters in our fiducial analysis. As shown, only the matter density, the matter amplitude and the amplitudes of intrinsic alignment parameters are well constrained by our cosmic shear 2PCFs analysis. Then the posteriors for our internal consistent tests are shown in the following subsections.

1. Priors

We show the marginalized 2D posteriors in the $(\Omega_{\rm m}, S_8)$ plane for analyses with different flat priors on A_s $\ln(A_s)$ and S_8 in Figs. 25 and 26, which are sampled with the `MultiNest` and `PolyChord` samplers, respectively. We refer the readers to Sec. V B for a detailed discussion.

2. Physical models

We show the marginalized 2D posteriors in the $(\Omega_{\rm m}, S_8)$ plane for analyses with different physical models in Fig. 27. The posteriors are sampled with `MultiNest`. We refer the readers to Sec. V C for a detailed discussion.

3. Systematic models

We show the marginalized 2D posteriors in the $(\Omega_{\rm m}, S_8)$ plane for analyses with different systematic models in Fig. 28. The posteriors are sampled with `MultiNest`. We refer the readers to Sec. V D for a detailed discussion.

4. Subfields

We show the marginalized 2D posteriors in the $(\Omega_{\rm m}, S_8)$ plane for analyses on different HSC-Y3 subfields in Fig. 29. The posteriors are sampled with `MultiNest`. We refer the readers to Sec. V F for a detailed discussion.

5. Scales

We show the marginalized 2D posteriors in the $(\Omega_{\rm m}, S_8)$ plane for analyses with different angular scale cuts in Fig. 30. The posteriors are sampled with `MultiNest`. We refer the readers to Sec. V F for a detailed discussion.

6. Tomographic bins

We show the marginalized 2D posteriors in the $(\Omega_{\rm m}, S_8)$ plane for analyses with removals of one of the four tomographic bins in Fig. 31. The posteriors are sampled with `MultiNest`. We refer the readers to Sec. V F for a detailed discussion.

7. Samplers

We show the marginalized 2D posteriors in the $(\Omega_{\rm m}, S_8)$ plane for the analyses with fiducial setup but sampled with different samplers in Fig. 32. We refer the readers to Sec. V E for a detailed discussion.

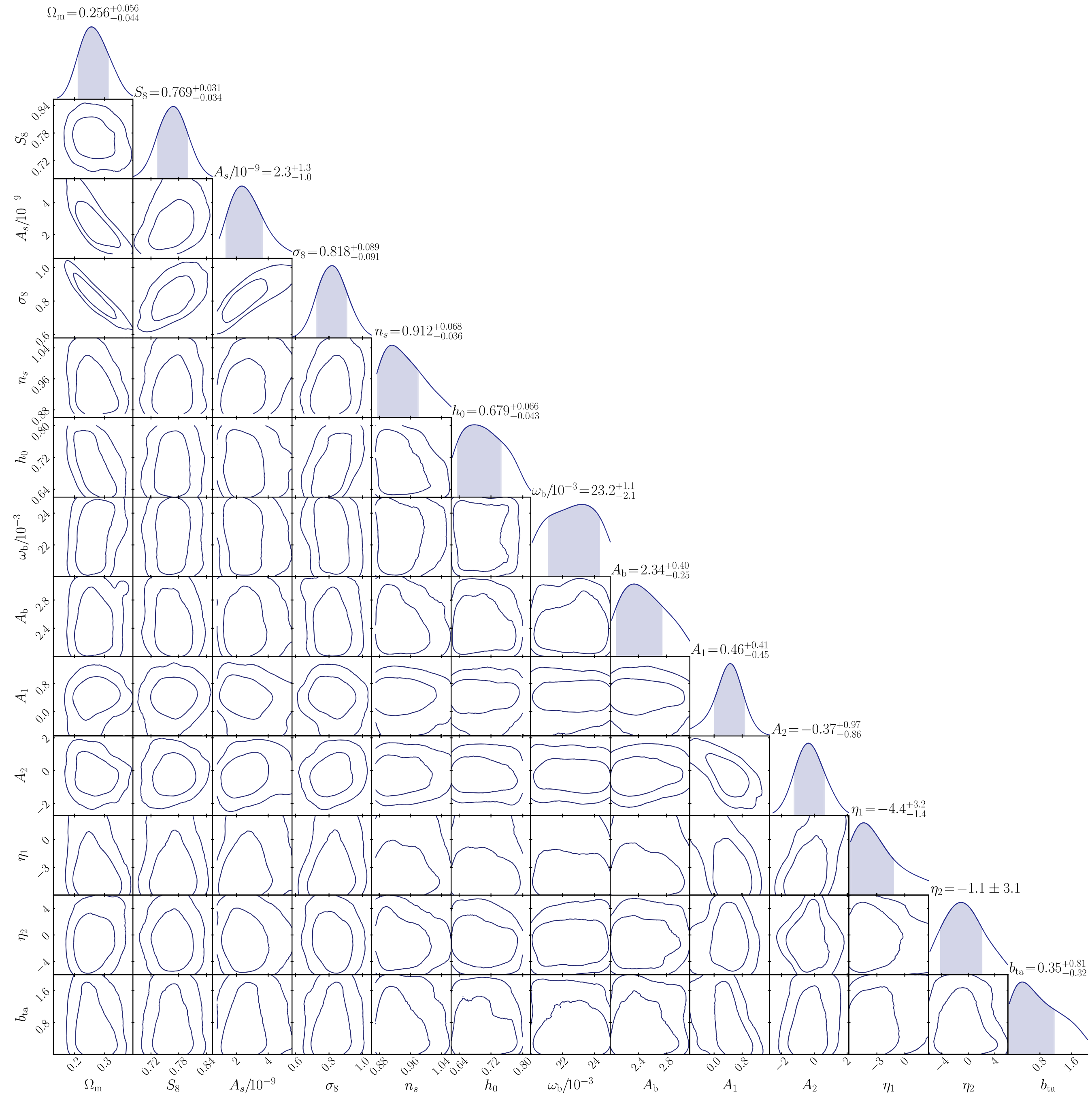

FIG. 24. Marginalized posteriors of the fiducial analysis for the various parameters in our analysis, including the cosmological ($\Omega_{\rm m}$, S_8, A_s, σ_8, n_s, h_0, $\omega_{\rm b}$), the parameter from HMCode 2016 encoding baryonic feedback ($A_{\rm b}$), and the TATT intrinsic alignment (A_1, A_2, η_1, η_2, $b_{\rm ta}$) parameters.

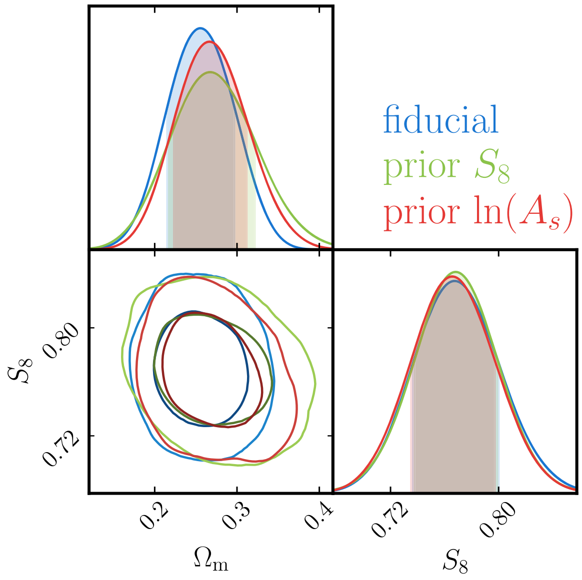

FIG. 25. The marginalized 2D posteriors analyzed with different flat priors on A_s (fiducial), S_8 and $\ln(A_s)$ sampled with `MultiNest`.

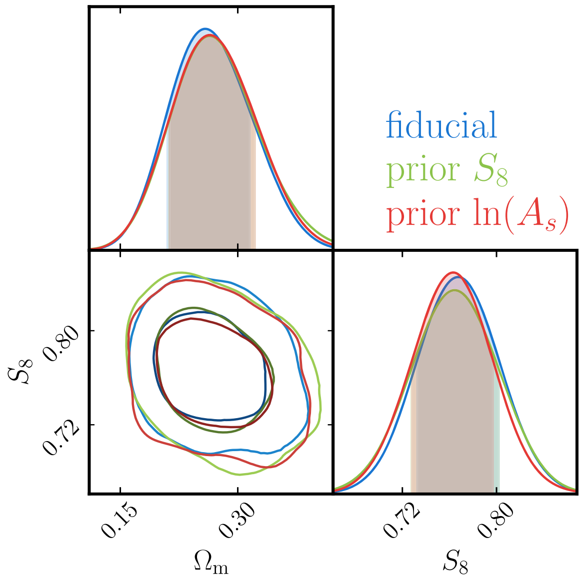

FIG. 26. The marginalized 2D posteriors analyzed with different flat priors on A_s (fiducial), S_8 and $\ln(A_s)$ sampled with `PolyChord`.

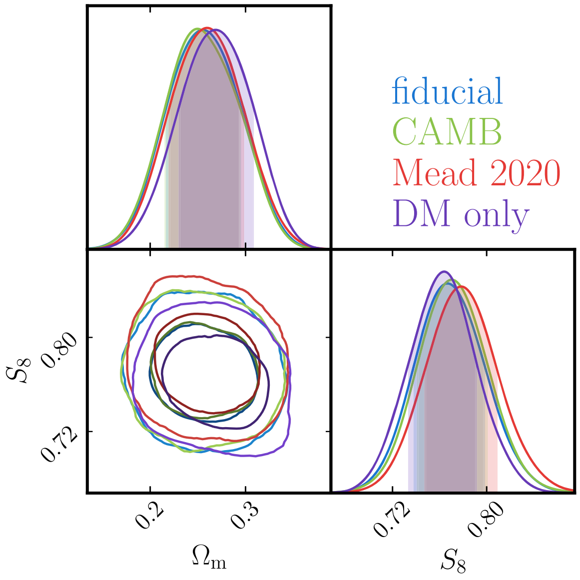

FIG. 27. The marginalized 2D posteriors analyzed with different models for cold matter power spectrum.

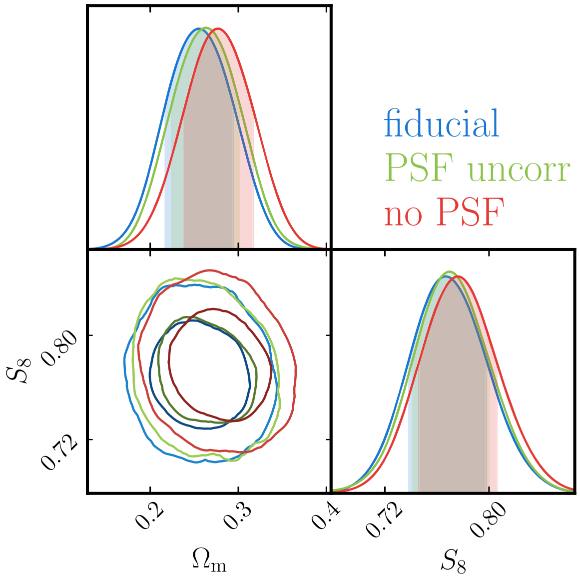

FIG. 28. The marginalized 2D posteriors analyzed with different systematic models.

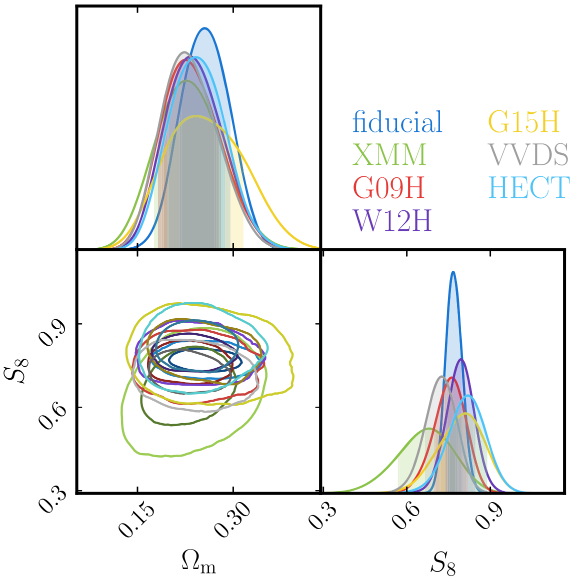

FIG. 29. The marginalized 2D posteriors in the (Ω_m, σ_8) plane for six different subfields.

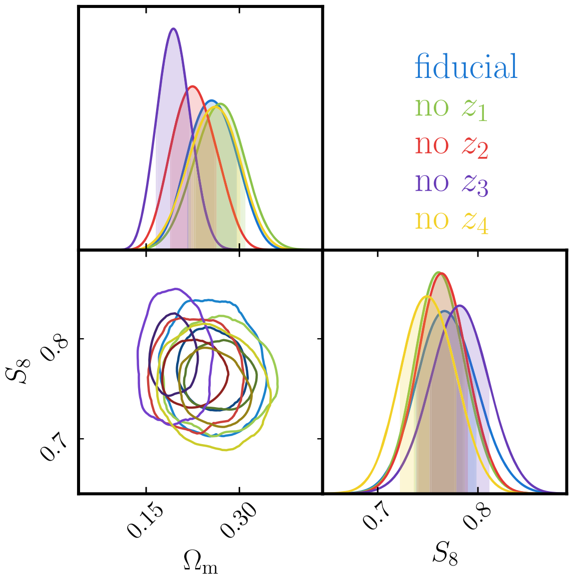

FIG. 31. The marginalized 2D posteriors in the (Ω_m, σ_8) plane when removing one of the redshift bins.

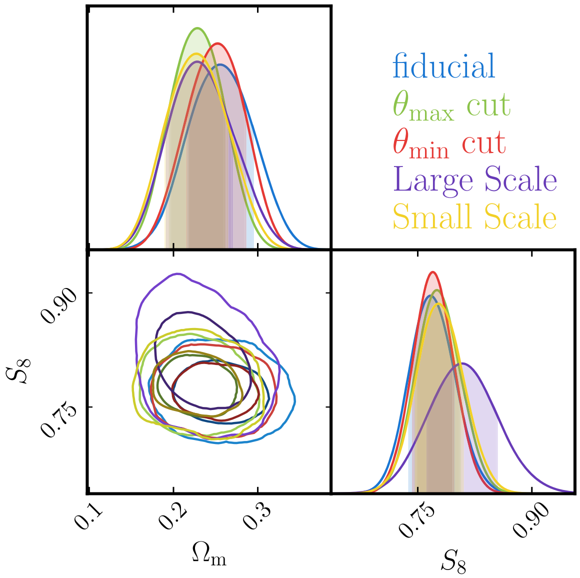

FIG. 30. The marginalized 2D posteriors in the (Ω_m, σ_8) plane with six different cuts on angular scales.

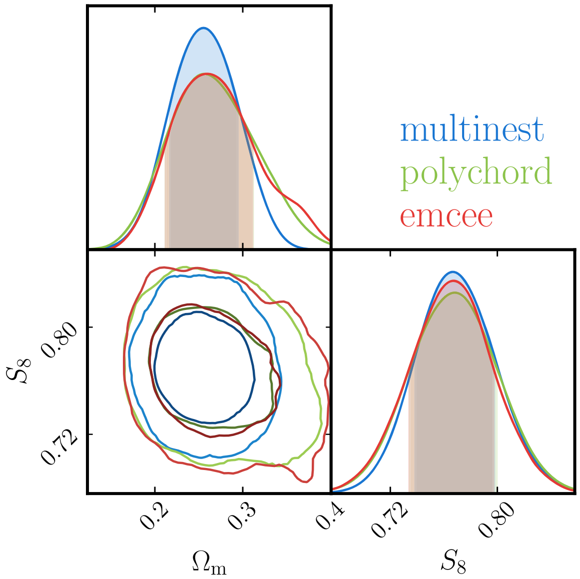

FIG. 32. The marginalized 2D posteriors in the (Ω_m, σ_8) plane for different samplers; `MultiNest`, `PolyChord`, and EMCEE.

[1] M. Betoule, R. Kessler, J. Guy, J. Mosher, D. Hardin *et al.*, Astron. Astrophys. **568**, A22 (2014).

[2] B. D. Fields, K. A. Olive, T.-H. Yeh, and C. Young, J. Cosmol. Astropart. Phys. 03 (2020) 010.

[3] G. Hinshaw, D. Larson, E. Komatsu, D. N. Spergel, C. L. Bennett *et al.*, Astrophys. J. Suppl. Ser. **208**, 19 (2013).

[4] N. Aghanim, Y. Akrami, M. Ashdown, J. Aumont *et al.* (Planck Collaboration), Astron. Astrophys. **641**, A6 (2020).

[5] T. Hamana, M. Shirasaki, S. Miyazaki, C. Hikage, M. Oguri *et al.*, Publ. Astron. Soc. Jpn. **72**, 16 (2020).

[6] M. Asgari, C.-A. Lin, B. Joachimi, B. Giblin, C. Heymans *et al.*, Astron. Astrophys. **645**, A104 (2021).

[7] L. F. Secco, S. Samuroff, E. Krause, B. Jain, J. Blazek, M. Raveri *et al.*, Phys. Rev. D **105**, 023515 (2022).

[8] S. Sugiyama, M. Takada, H. Miyatake, T. Nishimichi, M. Shirasaki, Y. Kobayashi *et al.*, Phys. Rev. D **105**, 123537 (2022).

[9] H. Miyatake, S. Sugiyama, M. Takada, T. Nishimichi, M. Shirasaki *et al.*, Phys. Rev. D **106**, 083520 (2022).

[10] C. Heymans, T. Tröster, M. Asgari, C. Blake, H. Hildebrandt, B. Joachimi *et al.*, Astron. Astrophys. **646**, A140 (2021).

[11] T. M. C. Abbott, M. Aguena, A. Alarcon, S. Allam, O. Alves, A. Amon *et al.*, Phys. Rev. D **105**, 023520 (2022).

[12] Y. Kobayashi, T. Nishimichi, M. Takada, and H. Miyatake, Phys. Rev. D **105**, 083517 (2022).

[13] E. Abdalla, G. F. Abellán, A. Aboubrahim, A. Agnello, Ö. Akarsu *et al.*, J. High Energy Astrophys. **34**, 49 (2022).

[14] M. Bartelmann and P. Schneider, Phys. Rep. **340**, 291 (2001).

[15] M. Kilbinger, Rep. Prog. Phys. **78**, 086901 (2015).

[16] J. T. A. de Jong, G. A. Verdoes Kleijn, K. H. Kuijken, and E. A. Valentijn, Exp. Astron. **35**, 25 (2013).

[17] T. Abbott, F. B. Abdalla, J. Aleksić, S. Allam *et al.* (Dark Energy Survey Collaboration), Mon. Not. R. Astron. Soc. **460**, 1270 (2016).

[18] H. Aihara, N. Arimoto, R. Armstrong, S. Arnouts, N. A. Bahcall, S. Bickerton, J. Bosch *et al.*, Publ. Astron. Soc. Jpn. **70**, S4 (2018).

[19] S. Miyazaki, Y. Komiyama, S. Kawanomoto, Y. Doi, H. Furusawa, T. Hamana *et al.*, Publ. Astron. Soc. Jpn. **70**, S1 (2018).

[20] Y. Komiyama, Y. Obuchi, H. Nakaya, Y. Kamata, S. Kawanomoto, Y. Utsumi *et al.*, Publ. Astron. Soc. Jpn. **70**, S2 (2018).

[21] S. Kawanomoto, F. Uraguchi, Y. Komiyama, S. Miyazaki, H. Furusawa *et al.*, Publ. Astron. Soc. Jpn. **70**, 66 (2018).

[22] H. Furusawa, M. Koike, T. Takata, Y. Okura, H. Miyatake, R. H. Lupton *et al.*, Publ. Astron. Soc. Jpn. **70**, S3 (2018).

[23] X. Li, H. Miyatake, W. Luo, S. More, M. Oguri, T. Hamana, R. Mandelbaum *et al.*, Publ. Astron. Soc. Jpn. **74**, 421 (2022).

[24] M. M. Rau, R. Dalal, T. Zhang, X. Li, A. J. Nishizawa, S. More, R. Mandelbaum, H. Miyatake, M. A. Strauss, and M. Takada, Mon. Not. R. Astron. Soc. **524**, 5109 (2023).

[25] M. Oguri, Mon. Not. R. Astron. Soc. **444**, 147 (2014).

[26] M. Oguri, Y.-T. Lin, S.-C. Lin, A. J. Nishizawa, A. More *et al.*, Publ. Astron. Soc. Jpn. **70**, S20 (2018).

[27] M. Oguri, S. Miyazaki, C. Hikage, R. Mandelbaum, Y. Utsumi *et al.*, Publ. Astron. Soc. Jpn. **70**, S26 (2018).

[28] T. Zhang, X. Li, R. Dalal, R. Mandelbaum, M. A. Strauss, A. Kannawadi, H. Miyatake *et al.*, Mon. Not. R. Astron. Soc. **525**, 2441 (2023).

[29] R. Mandelbaum, Annu. Rev. Astron. Astrophys. **56**, 393 (2018).

[30] A. J. Mead, S. Brieden, T. Tröster, and C. Heymans, Mon. Not. R. Astron. Soc. **502**, 1401 (2021).

[31] K. R. Moran, K. Heitmann, E. Lawrence, S. Habib, D. Bingham, D. Bingham, A. Upadhye, J. Kwan, D. Higdon, and R. Payne, Mon. Not. R. Astron. Soc. **520**, 3443 (2023).

[32] K. Osato, M. Shirasaki, and N. Yoshida, Astrophys. J. **806**, 186 (2015).

[33] A. Chen, G. Aricò, D. Huterer, R. Angulo, N. Weaverdyck, O. Friedrich *et al.*, Mon. Not. R. Astron. Soc. **518**, 5340 (2023).

[34] T. Tröster, A. J. Mead, C. Heymans, Z. Yan, D. Alonso *et al.*, Astron. Astrophys. **660**, A27 (2022).

[35] C. M. Hirata, R. Mandelbaum, M. Ishak, U. Seljak, R. Nichol, K. A. Pimbblet, N. P. Ross, and D. Wake, Mon. Not. R. Astron. Soc. **381**, 1197 (2007).

[36] S. Bridle and L. King, New J. Phys. **9**, 444 (2007).

[37] J. A. Blazek, N. MacCrann, M. A. Troxel, and X. Fang, Phys. Rev. D **100**, 103506 (2019).

[38] A. Amon, D. Gruen, M. A. Troxel, N. MacCrann, S. Dodelson, A. Choi *et al.*, arXiv:2105.13543.

[39] R. Dalal, X. Li, A. Nicola, J. Zuntz, M. A. Strauss *et al.*, arXiv:2304.00701.

[40] S. More, S. Sugiyama, H. Miyatake, M. M. Rau, M. Shirasaki *et al.*, arXiv:2304.00703.

[41] S. Sugiyama, H. Miyatake, S. More, X. Li, M. Shirasaki *et al.*, arXiv:2304.00705.

[42] H. Miyatake, S. Sugiyama, M. Takada, T. Nishimichi, X. Li, M. Shirasaki, S. More *et al.*, arXiv:2304.00704.

[43] A. J. Nishizawa, B.-C. Hsieh, M. Tanaka, and T. Takata, arXiv:2003.01511.

[44] H. Hildebrandt, M. Viola, C. Heymans, S. Joudaki, K. Kuijken, C. Blake *et al.*, Mon. Not. R. Astron. Soc. **465**, 1454 (2017).

[45] C. Chang, M. Jarvis, B. Jain, S. M. Kahn, D. Kirkby, D. Kirkby, A. Connolly, S. Krughoff, E.-H. Peng, and J. R. Peterson, Mon. Not. R. Astron. Soc. **434**, 2121 (2013).

[46] C. Hirata and U. Seljak, Mon. Not. R. Astron. Soc. **343**, 459 (2003).

[47] J. Bosch, R. Armstrong, S. Bickerton, H. Furusawa, H. Ikeda, M. Koike *et al.*, Publ. Astron. Soc. Jpn. **70**, S5 (2018).

[48] A. Leauthaud, R. Massey, J.-P. Kneib, J. Rhodes, D. E. Johnston, P. Capak *et al.*, Astrophys. J. Suppl. Ser. **172**, 219 (2007).

[49] R. Mandelbaum, F. Lanusse, A. Leauthaud, R. Armstrong, M. Simet, H. Miyatake, J. E. Meyers *et al.*, Mon. Not. R. Astron. Soc. **481**, 3170 (2018).

[50] E. Krause, X. Fang, S. Pandey, L. F. Secco, O. Alves *et al.*, arXiv:2105.13548.

[51] A. J. Nishizawa *et al.* (to be published).

[52] B. C. Hsieh and H. K. C. Yee, Astrophys. J. **792**, 102 (2014).

[53] M. Tanaka, Astrophys. J. **801**, 20 (2015).
[54] G. Bruzual and S. Charlot, Mon. Not. R. Astron. Soc. **344**, 1000 (2003).
[55] G. Chabrier, Publ. Astron. Soc. Pac. **115**, 763 (2003).
[56] A. K. Inoue, Mon. Not. R. Astron. Soc. **415**, 2920 (2011).
[57] D. Calzetti, L. Armus, R. C. Bohlin, A. L. Kinney, J. Koornneef, and T. Storchi-Bergmann, Astrophys. J. **533**, 682 (2000).
[58] R. Bordoloi, S. J. Lilly, and A. Amara, Mon. Not. R. Astron. Soc. **406**, 881 (2010).
[59] M. Shirasaki, T. Hamana, M. Takada, R. Takahashi, and H. Miyatake, Mon. Not. R. Astron. Soc. **486**, 52 (2019).
[60] R. Takahashi, T. Hamana, M. Shirasaki, T. Namikawa, T. Nishimichi, K. Osato, and K. Shiroyama, Astrophys. J. **850**, 24 (2017).
[61] T. Hamana, J. Sakurai, M. Koike, and L. Miller, Publ. Astron. Soc. Jpn. **67**, 34 (2015).
[62] M. Shirasaki, T. Hamana, and N. Yoshida, Mon. Not. R. Astron. Soc. **453**, 3043 (2015).
[63] P. Schneider, L. van Waerbeke, and Y. Mellier, Astron. Astrophys. **389**, 729 (2002).
[64] A. Amon, D. Gruen, M. A. Troxel, N. MacCrann, S. Dodelson, A. Choi *et al.*, Phys. Rev. D **105**, 023514 (2022).
[65] J. Hartlap, P. Simon, and P. Schneider, Astron. Astrophys. **464**, 399 (2007).
[66] H. Camacho, F. Andrade-Oliveira, A. Troja, R. Rosenfeld, L. Faga *et al.*, Mon. Not. R. Astron. Soc. **516**, 5799 (2022).
[67] A. Nicola, C. García-García, D. Alonso, J. Dunkley, P. G. Ferreira, A. Slosar, and D. N. Spergel, J. Cosmol. Astropart. Phys. 03 (2021) 067.
[68] S. Singh, Mon. Not. R. Astron. Soc. **508**, 1632 (2021).
[69] P. Schneider, T. Eifler, and E. Krause, Astron. Astrophys. **520**, A116 (2010).
[70] T. Hamana, C. Hikage, M. Oguri, M. Shirasaki, and S. More, Publ. Astron. Soc. Jpn. **74**, 923 (2022).
[71] M. Takada and W. Hu, Phys. Rev. D **87**, 123504 (2013).
[72] D. Kodwani, D. Alonso, and P. Ferreira, Open J. Astrophys. **2**, 3 (2019).
[73] E. Krause and C. M. Hirata, Astron. Astrophys. **523**, A28 (2010).
[74] J. Zuntz, M. Paterno, E. Jennings, D. Rudd, A. Manzotti *et al.*, Astron. Comput. **12**, 45 (2015).
[75] X. Fang, T. Eifler, and E. Krause, Mon. Not. R. Astron. Soc. **497**, 2699 (2020).
[76] M. A. Troxel and M. Ishak, Phys. Rep. **558**, 1 (2015).
[77] D. N. Limber, Astrophys. J. **117**, 134 (1953).
[78] M. LoVerde and N. Afshordi, Phys. Rev. D **78**, 123506 (2008).
[79] A. Lewis, A. Challinor, and A. Lasenby, Astrophys. J. **538**, 473 (2000).
[80] J. Lesgourgues, arXiv:1104.2932.
[81] D. Blas, J. Lesgourgues, and T. Tram, J. Cosmol. Astropart. Phys. 07 (2011) 034.
[82] R. Takahashi, M. Sato, T. Nishimichi, A. Taruya, and M. Oguri, Astrophys. J. **761**, 152 (2012).
[83] A. J. Mead, J. A. Peacock, C. Heymans, S. Joudaki, and A. F. Heavens, Mon. Not. R. Astron. Soc. **454**, 1958 (2015).
[84] A. J. Mead, C. Heymans, L. Lombriser, J. A. Peacock, O. I. Steele, and H. A. Winther, Mon. Not. R. Astron. Soc. **459**, 1468 (2016).
[85] G. Aricò, R. E. Angulo, and M. Zennaro, arXiv:2104.14568.
[86] S. Günther, J. Lesgourgues, G. Samaras, N. Schöneberg, F. Stadtmann, C. Fidler, and J. Torrado, J. Cosmol. Astropart. Phys. 11 (2022) 035.
[87] T. Nishimichi, M. Takada, R. Takahashi, K. Osato, M. Shirasaki *et al.*, Astrophys. J. **884**, 29 (2019).
[88] R. E. Angulo, M. Zennaro, S. Contreras, G. Aricò, M. Pellejero-Ibañez, and J. Stücker, Mon. Not. R. Astron. Soc. **507**, 5869 (2021).
[89] M. Knabenhans, J. Stadel, D. Potter, J. Dakin *et al.* (Euclid Collaboration), Mon. Not. R. Astron. Soc. **505**, 2840 (2021).
[90] B. Joachimi, C. A. Lin, M. Asgari, T. Tröster, C. Heymans, H. Hildebrandt, F. Köhlinger *et al.*, Astron. Astrophys. **646**, A129 (2021).
[91] A. Schneider, R. Teyssier, J. Stadel, N. E. Chisari, A. M. C. Le Brun, A. Amara, and A. Refregier, J. Cosmol. Astropart. Phys. 03 (2019) 020.
[92] H.-J. Huang, T. Eifler, R. Mandelbaum, G. M. Bernstein, A. Chen *et al.*, Mon. Not. R. Astron. Soc. **502**, 6010 (2021).
[93] J. E. McEwen, X. Fang, C. M. Hirata, and J. A. Blazek, J. Cosmol. Astropart. Phys. 09 (2016) 015.
[94] X. Fang, J. A. Blazek, J. E. McEwen, and C. M. Hirata, J. Cosmol. Astropart. Phys. 02 (2017) 030.
[95] M. L. Brown, A. N. Taylor, N. C. Hambly, and S. Dye, Mon. Not. R. Astron. Soc. **333**, 501 (2002).
[96] S. Singh, R. Mandelbaum, and S. More, Mon. Not. R. Astron. Soc. **450**, 2195 (2015).
[97] Y. Jagvaral, S. Singh, and R. Mandelbaum, Mon. Not. R. Astron. Soc. **514**, 1021 (2022).
[98] A. Campos, S. Samuroff, and R. Mandelbaum, Mon. Not. R. Astron. Soc. **525**, 1885 (2023).
[99] S. Ishikawa, T. Okumura, M. Oguri, and S.-C. Lin, Astrophys. J. **922**, 23 (2021).
[100] T. Zhang, M. M. Rau, R. Mandelbaum, X. Li, and B. Moews, Mon. Not. R. Astron. Soc. **518**, 709 (2023).
[101] G. M. Bernstein, Mon. Not. R. Astron. Soc. **406**, 2793 (2010).
[102] A. Refregier, T. Kacprzak, A. Amara, S. Bridle, and B. Rowe, Mon. Not. R. Astron. Soc. **425**, 1951 (2012).
[103] N. Kaiser, Astrophys. J. **537**, 555 (2000).
[104] E. S. Sheldon, M. R. Becker, N. MacCrann, and M. Jarvis, Astrophys. J. **902**, 138 (2020).
[105] D. Foreman-Mackey, D. W. Hogg, D. Lang, and J. Goodman, Publ. Astron. Soc. Pac. **125**, 306 (2013).
[106] F. Feroz, M. P. Hobson, and M. Bridges, Mon. Not. R. Astron. Soc. **398**, 1601 (2009).
[107] W. J. Handley, M. P. Hobson, and A. N. Lasenby, Mon. Not. R. Astron. Soc. **450**, L61 (2015).
[108] P. Lemos, N. Weaverdyck, R. P. Rollins, J. Muir, A. Ferté, A. R. Liddle, A. Campos *et al.*, Mon. Not. R. Astron. Soc. **521**, 1184 (2023).
[109] E. Higson, W. Handley, M. Hobson, and A. Lasenby, Mon. Not. R. Astron. Soc. **483**, 2044 (2019).

[110] B. Joachimi, C. A. Lin, M. Asgari, T. Tröster, C. Heymans, H. Hildebrandt, F. Köhlinger *et al.*, Astron. Astrophys. **646**, A129 (2021).

[111] J. Schaye, C. Dalla Vecchia, C. M. Booth, R. P. C. Wiersma, T. Theuns, M. R. Haas, S. Bertone, A. R. Duffy, I. G. McCarthy, and F. van de Voort, Mon. Not. R. Astron. Soc. **402**, 1536 (2010).

[112] M. P. van Daalen, J. Schaye, C. M. Booth, and C. Dalla Vecchia, Mon. Not. R. Astron. Soc. **415**, 3649 (2011).

[113] A. M. C. Le Brun, I. G. McCarthy, J. Schaye, and T. J. Ponman, Mon. Not. R. Astron. Soc. **441**, 1270 (2014).

[114] M. Vogelsberger, S. Genel, V. Springel, P. Torrey, D. Sijacki, D. Xu, G. Snyder, D. Nelson, and L. Hernquist, Mon. Not. R. Astron. Soc. **444**, 1518 (2014).

[115] N. Khandai, T. Di Matteo, R. Croft, S. Wilkins, Y. Feng, E. Tucker, C. DeGraf, and M.-S. Liu, Mon. Not. R. Astron. Soc. **450**, 1349 (2015).

[116] R. A. Crain, J. Schaye, R. G. Bower, M. Furlong, M. Schaller *et al.*, Mon. Not. R. Astron. Soc. **450**, 1937 (2015).

[117] S. Kaviraj, C. Laigle, T. Kimm, J. E. G. Devriendt, Y. Dubois *et al.*, Mon. Not. R. Astron. Soc. **467**, 4739 (2017).

[118] D. Nelson, V. Springel, A. Pillepich, V. Rodriguez-Gomez, P. Torrey, S. Genel *et al.*, Comput. Astrophys. Cosmol. **6**, 2 (2019).

[119] J. A. Nelder and R. Mead, Comput. J. **7**, 308 (1965).

[120] S. Hinton, J. Open Source Software **1**, 45 (2016).

[121] A. Lewis, arXiv:1910.13970.

[122] C. Hikage, M. Oguri, T. Hamana, S. More, R. Mandelbaum, M. Takada, F. Köhlinger *et al.*, Publ. Astron. Soc. Jpn. **71**, 43 (2019).

[123] E. P. Longley, C. Chang, C. W. Walter, J. Zuntz, M. Ishak, R. Mandelbaum *et al.*, Mon. Not. R. Astron. Soc. **520**, 5016 (2023).

[124] T. Tröster, A. J. Mead, C. Heymans, Z. Yan, D. Alonso *et al.*, Astron. Astrophys. **660**, A27 (2022).

[125] T. Bakx, T. Kurita, N. E. Chisari, Z. Vlah, and F. Schmidt, arXiv:2303.15565.

[126] C. D. Leonard, R. Mandelbaum (LSST Dark Energy Science Collaboration), Mon. Not. R. Astron. Soc. **479**, 1412 (2018).

[127] C. M. B. MacMahon and C. D. Leonard, arXiv:2306.11428.

[128] P. Zhang, Astrophys. J. **720**, 1090 (2010).

[129] J. Yao, M. Ishak, and M. A. Troxel (LSST Dark Energy Science Collaboration), Mon. Not. R. Astron. Soc. **483**, 276 (2019).

[130] F. Capozzi, G. L. Fogli, E. Lisi, A. Marrone, D. Montanino, and A. Palazzo, Phys. Rev. D **89**, 093018 (2014).

[131] I. Esteban, M. C. Gonzalez-Garcia, A. Hernandez-Cabezudo, M. Maltoni, and T. Schwetz, J. High Energy Phys. 01 (2019) 106.

[132] K. Ichiki, M. Takada, and T. Takahashi, Phys. Rev. D **79**, 023520 (2009).

[133] A. I. Malz and D. W. Hogg, Astrophys. J. **928**, 127 (2022).

[134] M. Gatti, E. Sheldon, A. Amon, M. Becker, M. Troxel *et al.*, Mon. Not. R. Astron. Soc. **504**, 4312 (2021).

[135] B. Giblin, C. Heymans, M. Asgari, H. Hildebrandt, H. Hoekstra, B. Joachimi *et al.*, Astron. Astrophys. **645**, A105 (2021).

[136] T. Charnock, R. A. Battye, and A. Moss, Phys. Rev. D **95**, 123535 (2017).

[137] Y. Park and E. Rozo, Mon. Not. R. Astron. Soc. **499**, 4638 (2020).

[138] S. Alam, M. Aubert, S. Avila, C. Balland, J. E. Bautista *et al.*, Phys. Rev. D **103**, 083533 (2021).

[139] A. J. Ross, L. Samushia, C. Howlett, W. J. Percival, A. Burden, and M. Manera, Mon. Not. R. Astron. Soc. **449**, 835 (2015).

[140] S. Alam, M. Ata, S. Bailey, F. Beutler, D. Bizyaev, J. A. Blazek *et al.*, Mon. Not. R. Astron. Soc. **470**, 2617 (2017).

[141] J. E. Bautista, R. Paviot, M. Vargas Magaña, S. de la Torre, S. Fromenteau, H. Gil-Marín *et al.*, Mon. Not. R. Astron. Soc. **500**, 736 (2021).

[142] A. de Mattia, V. Ruhlmann-Kleider, A. Raichoor, A. J. Ross, A. Tamone *et al.*, Mon. Not. R. Astron. Soc. **501**, 5616 (2021).

[143] R. Neveux, E. Burtin, A. de Mattia, A. Smith, A. J. Ross *et al.*, Mon. Not. R. Astron. Soc. **499**, 210 (2020).

[144] H. du Mas des Bourboux, J. Rich, A. Font-Ribera, V. de Sainte Agathe, J. Farr *et al.*, Astrophys. J. **901**, 153 (2020).

[145] A. Leauthaud, A. Amon, S. Singh, D. Gruen, J. U. Lange *et al.*, Mon. Not. R. Astron. Soc. **510**, 6150 (2022).

[146] C. Heymans, E. Grocutt, A. Heavens, M. Kilbinger, T. D. Kitching, F. Simpson *et al.*, Mon. Not. R. Astron. Soc. **432**, 2433 (2013).

[147] A. Leauthaud, S. Saito, S. Hilbert, A. Barreira, S. More *et al.*, Mon. Not. R. Astron. Soc. **467**, 3024 (2017).

[148] J. Zuntz, E. Sheldon, S. Samuroff, M. A. Troxel, M. Jarvis, N. MacCrann *et al.*, Mon. Not. R. Astron. Soc. **481**, 1149 (2018).

[149] A. H. Wright, H. Hildebrandt, K. Kuijken, T. Erben, R. Blake *et al.*, Astron. Astrophys. **632**, A34 (2019).

[150] R. Mandelbaum, H. Miyatake, T. Hamana, M. Oguri, M. Simet, R. Armstrong *et al.*, Publ. Astron. Soc. Jpn. **70**, S25 (2018).

[151] P. Melchior, F. Moolekamp, M. Jerdee, R. Armstrong, A. L. Sun, J. Bosch, and R. Lupton, Astron. Comput. **24**, 129 (2018).

[152] M. Jarvis, J. Meyers, P.-F. Leget, and C. Davis, Piff: PSFs in the Full FOV, Astrophysics Source Code Library, record ascl:2102.024 (2021).

[153] B. Abolfathi, D. Alonso, R. Armstrong, É. Aubourg, H. Awan *et al.* (LSST Dark Energy Science Collaboration), Astrophys. J. Suppl. Ser. **253**, 31 (2021).

[154] N. MacCrann, M. R. Becker, J. McCullough, A. Amon, D. Gruen, M. Jarvis *et al.*, Mon. Not. R. Astron. Soc. **509**, 3371 (2022).

[155] S.-S. Li, K. Kuijken, H. Hoekstra, L. Miller, C. Heymans, H. Hildebrandt *et al.*, Astron. Astrophys. **670**, A100 (2023).

[156] X. Li, N. Katayama, M. Oguri, and S. More, Mon. Not. R. Astron. Soc. **481**, 4445 (2018).
[157] X. Li, Y. Li, and R. Massey, Mon. Not. R. Astron. Soc. **511**, 4850 (2022).
[158] X. Li and R. Mandelbaum, Mon. Not. R. Astron. Soc. **521**, 4904 (2023).
[159] A. Aghamousa, J. Aguilar, S. Ahlen, S. Alam *et al.* (DESI Collaboration), arXiv:1611.00036.
[160] C. Sánchez, J. Prat, G. Zacharegkas, S. Pandey, E. Baxter, G. M. Bernstein *et al.*, Phys. Rev. D **105**, 083529 (2022).
[161] N. C. Robertson, D. Alonso, J. Harnois-Déraps, O. Darwish, A. Kannawadi, A. Amon, M. Asgari *et al.*, Astron. Astrophys. **649**, A146 (2021).
[162] Ž. Ivezić, S. M. Kahn, J. A. Tyson, B. Abel, E. Acosta *et al.*, Astrophys. J. **873**, 111 (2019).
[163] R. Laureijs, J. Amiaux, S. Arduini, J. Augueres, J. Brinchmann *et al.*, arXiv:1110.3193.
[164] D. Spergel, N. Gehrels, C. Baltay, D. Bennett, J. Breckinridge, M. Donahue *et al.*, arXiv:1503.03757.